ASPECTS OF MASS SPECTROMETRY: ISOBARIC INTERFERENCE SOLUTIONS AND QUANTITATION IN FOURIER TRANSFORM ION CYCLOTRON RESONANCE MASS SPECTROMETRY (FTICR-MS)

By

KEVIN L. GOODNER

A DISSERTATION PRESENTED TO THE GRADUATE SCHOOL
OF THE UNIVERSITY OF FLORIDA IN PARTIAL FULFILLMENT
OF THE REQUIREMENTS FOR THE DEGREE OF
DOCTOR OF PHILOSOPHY

UNIVERSITY OF FLORIDA

1996

ACKNOWLEDGMENTS

I am approaching the end of my graduate career, and as I look back there are a multitude of people whose help has made this possible.

The major source of guidance in my life, by far, has been my parents, Mary and Sammy Goodner. Their love and dedication have been instrumental in my development. Their constant expectations of high academic performance have been the measuring stick that I have used to grade my career.

Along the way many people have stood out in my life. Mr. Cunningham gave me the competitive edge that is often needed (especially in Finance^{tm}, Monopoly^{tm}, and Blackjack). Ms. Diane Suits was unquestionably the single most important teacher in my life. Ms. Suits made learning fun; that is the best lesson to discover in life. Two other important teachers were Mr. Harold Reno and Mrs. McIntyre. These high school teachers were the first I encountered who treated students as adults (with regard to teaching, expectations, and friendships).

During college Dr. Larry Houk provided much guidance regarding not only academics, but also attitude. He showed that fun, hobbies, and other interests are compatible with hard work, as well as desirable. Dr. Richard F. Browner guided me on my early bumbling attempts at research during my summer undergraduate research at Georgia Tech. He introduced me to basic research and the way a research group is supposed to work. Dr. Browner also helped with my decisions regarding graduate school and specialization area.

Mr. Joseph Shalosky definitely deserves many accolades for his master machining skills. The second project in this thesis (the internal GD) would not have been possible without his expertise.

My graduate career introduced me to several people who deserve special acknowledgement. Dr. John R. Eyler has guided my research in mass spectrometry. He has shown by example the proper way for science to be conducted and reported. Most of the beliefs I have about research, group dynamics, and the state of science are due to him. During my summer at Oak Ridge National Laboratory (ORNL), Dr. Christopher M. Barshick showed me the ins and outs of conducting and publishing research. The Eyler research group deserves thanks for all their help during my graduate studies. This includes Ragulan Ramanathan, Dilruski Peiris, Yarjing Yang, Eric Milgram, Joe Nawrocki, David Kage, Rich Burton, Lisa Lang, and Tom Hayes. A special person in Dr. Eyler's group is Dr. Clifford Watson. Cliff provided me with hands-on training in many areas of the lab (research, programming, politics, job searching, etc.). Cliff is also the person who had to endure my endless questions about how things work. He has been very patient in this regard and it is greatly appreciated.

Throughout my life I have had many friends. I cannot begin to list all of them, but a few deserve to be mentioned for their constant friendship for such a long time. Keith Lawson, Tyler Swafford, Bryan Patterson, Perry Singleton, and Rich Swafford have been good comrades for a long time. However, of all the friends I have had in my lifetime, one stands above all the rest. I would like to thank my best friend, my wife, Jamie, for the love, support, and encouragement she has given me. Without her, this would not have been possible.

TABLE OF CONTENTS

ACKNOWLEDGMENTS ii

LIST OF FIGURES vii

LIST OF TABLES x

ABSTRACT xi

CHAPTER

1 INTRODUCTION 1

2 INSTRUMENTATION 6

- Glow Discharge 6
- Sector Mass Spectrometers 14
- Fourier Transform Ion Cyclotron Resonance Mass Spectrometry 18
  - History 18
  - Ion Trapping 19
  - Ion Excitation 23
  - Ion Detection 25
  - Mass Accuracy and Resolution 27

3 ELEMENTAL QUANTITATION BASED ON ARGIDES, DIMERS, AND DOUBLY CHARGED GLOW DISCHARGE IONS 31

- Introduction 31
- Experimental 33
- Results and Discussion 34
  - Reference Quantitation 46
  - Unknown Quantitation 49
- Conclusions 53

4 INTERNAL GLOW DISCHARGE-FOURIER TRANSFORM ION CYCLOTRON RESONANCE MASS SPECTROMETRY (GD-FTICR/MS) 54

Introduction 54
Experimental 54
Results and Discussion 65
    Magnetic Field 69
    Pressure, Voltage, Current Studies 71
    Sputter rate 78
    Limits of Detection 73
    FTICR Advantages 74
Conclusions 77

5 QUANTITATION OF ION ABUNDANCES IN FOURIER TRANSFORM ION CYCLOTRON RESONANCE MASS SPECTROMETRY (FTICR-MS) 78

Introduction 78
Methodology 80
Results and Discussion 100
    Quantitation Based on Peak Height 100
    Quantitation Based on Peak Area 108
    Peak Ratio Measurements 112
    Unknown Quantitation 114
Conclusions 122

6 CONCLUSIONS 123

GLOSSARY 126

APPENDIX

A. BASIC CODE FOR DETERMINING INTERPOLATED HEIGHTS AND AREAS USED IN CHAPTER 5 128

B. BASIC CODE FOR INTERPOLATING PEAK HEIGHTS USING MATRIX METHODS USED IN CHAPTER 5 133

C. BASIC CODE FOR DETERMINING TRAPEZOIDAL AREA OF PEAKS AND EXTENDED TRAPEZOIDAL AREA OF PEAKS USED IN CHAPTER 5 135

D. BASIC CODE FOR DETERMINING INTEGRATED AREA OF PEAK USING COMISAROW EXPONENTS USED IN CHAPTER 5 136

REFERENCES 138

BIOGRAPHICAL SKETCH 146

LIST OF FIGURES

2.1 Properties of the different regions of a glow discharge 7

2.2 Graphical representation of a meteor (argon ion) striking the earth (sample). . . . 11

2.3 An illustration of the magnetic sector instrument used for the work described in Chapter 3. 17

2.4 The typical FTICR-MS analyzer cell. The detect plate nearest the viewer has been removed for clarity. An example of ion cyclotronic motion is also displayed. 21

3.1 Glow discharge mass spectra of four species formed from a copper cathode: (a) Cu^{+2}, (b) Cu^{+}, (c) CuAr^{+}, and (d) Cu$_2^{+}$. 36-39

3.2 Effect of power on relative ion signals of various species found using glow discharge mass spectrometry of a NIST SRM 604 cathode, 8 mPa argon. (a) Effect of power on relative ion signal of the M^{+}(■), M^{+2}(●), Mar^{+}(X), and M$_2^{+}$(▲) species. (b) Effect of power on relative ion signal of the TiO^{+}( ), MgO^{+}( ), AlO^{+}( ), CuO^{+}(X), and O^{+}( ) species. 41-42

3.3 Effect of pressure on average relative ion signal of the M^{+}(■), M^{+2}(●), MAr^{+}(X), M$_2^{+}$(▲) species. NIST SRM 604 cathode, 1.4 mA constant current. . 45

4.1 Schematic representation of the FT-ICR mass spectrometer including locations of analyzer cell, conductance limits, and internal glow discharge probe/source. (IG = ionization gauge; DP = diffusion pump; MP = mechanical pump) 59

4.2 Concentric tube arrangement with different pressure regimes indicated. The diagram is drawn to scale except for the conductance limits, which are exaggerated for clarity. Region A is pumped by two 500 l/min mechanical pumps. Region B is pumped by an 800 l/s cryo-pump. Region C is pumped by two 300 l/s diffusion pumps. Region D is pumped by a 700 l/s diffusion pump. (1) 1.91 cm (3/4") stainless steel sample probe; (2) glow discharge sample pin; (3) removable conductance limit and Delrin® holder; (4) second conductance limit; (5) electromagnetic shutter; (6) third conductance limit; (7) ICR cell; (8) 15.2 cm (6") outer vacuum chamber. 61

4.3 Glow discharge source/probe. (A) 1.91 cm (3/4") O.D. stainless steel probe; (B) polyethylene argon delivery tube; (C) 1/8" Swagelok® union; (D) 1/8" to 1/4" adapter; (E) high voltage connector; (F) electrical feed-through; (G) sample pin holder;(H) sample pin; (I) ceramic insulator; (J) Delrin® holder; (K) Viton® O-rings; (L) stainless steel wire mesh; (M) stainless steel conductance limit holder; (N) stainless steel removable conductance limit. 63

4.4 Mass spectra of NIST SRM 1261a steel sample using (a) an external source and (b) the internal probe/source. Figure 4a is reprinted by permission of the publisher from "A Glow Discharge Ion Source with Fourier Transform Ion Cyclotron Resonance Mass Spectrometric Detection" by Barshick and Eyler, *J. Am. Soc. Mass Spectrom.*, **3**, 122-127 Copyright 1992 by Elsevier Science Inc. 67-68

4.5 Power supply voltage necessary to maintain constant discharge current of 0.9 mA as a function of magnetic field strength at different pressures. 70

5.1 Examples of the three types of simulated spectra used in this study using a 32k data size, 3-term Blackman-Harris apodization, and no orders of zero filling. The examples show a high noise spectrum (a), moderate noise spectrum (b), and a spectrum without any noise (c). 83-85

5.2 Graphical examples of the four types of apodization functions utilized in this study. (a) 3-term Blackman-Harris, (b) Kaiser-Bessel, (c) Hamming, and (d) Hanning functions are shown corresponding to the functions given in Table 5.1. 89-92

5.3 Peak fitting using the "Comisarow method" for $^{208}Pb^{+1}$ using a simulated 32k data size, no noise, 3-term Blackman-Harris apodization function, and no orders of zero filling. 98

5.4 Bar graph showing the Average Absolute Percent Error (AAPE-eq. 23) obtained when using peak heights as a method for quantitation of ion abundances for various fitting functions, noise levels, and orders of zero filling. Along the x-axis are the 3 types of simulated spectra with the degree of zero filling for each type bracketed. Along the y-axis are the fitting techniques used. The arrows on some bars indicate that they are off-scale and have the value above the arrow. 102

5.5 Effect of data set size on AAPE using Hanning apodization, moderate noise level, one order of zero filling and the "Comisarow method" of peak height determination for damped and undamped transient response signals. 107

5.6 Bar graph showing the Average Absolute Percent Error (AAPE-eq. 23) obtained when using peak areas as a method for quantitation of ion abundances for various fitting functions, noise levels, and orders of zero filling. Along the x-axis are the 3 types of simulated spectra with the degree of zero filling for each type bracketed. Along the y-axis are the fitting techniques used. The arrows on some bars indicate that they are off-scale and have the value above the arrow. 110

5.7 Effect of data set size on AAPE using Hanning apodization, moderate noise level, one order of zero filling and the "Comisarow method" and "triangle method" of peak area determination for damped and undamped transient response signals. 113

5.8 Mass spectrum of xenon used for the unknown quantitation. The inset shows an expanded view of ^{130}Xe which clearly shows the splitting of the peak due magnet inhomegenity. The individual data points for ^{130}Xe are marked in order to illustrate the difficulty with accurate interpolation caused by splitting. . 115

5.9 Bar graph showing the Average Absolute Percent Error (AAPE-eq. 23) obtained when using peak heights as a method for quantitation of ion abundances for various fitting functions and orders of zero filling. Along the x-axis are the 2 trials of xenon spectra and the degrees of zero filling for each. Along the y-axis are the fitting techniques used. The arrows on some bars indicate that they are off-scale and have the value above the arrow. 118

5.10 Bar graph showing the Average Absolute Percent Error (AAPE-eq. 23) obtained when using peak areas as a method for quantitation of ion abundances for various fitting functions, noise levels, and orders of zero filling. Along the x-axis are the 3 types of simulated spectra and the degree of zero filling for each. Along the y-axis are the fitting techniques used. The arrows on some bars indicate that they are off-scale and have the value above the arrow. 121

LIST OF TABLES

2.1 Glow discharge ionization processes. 10

2.2 Metastable energies of noble gas atoms. 13

3.1 Concentrations of several elements in an NIST aluminum standard determined from the metal ion, the doubly-charged ion, the metal argide ion, and the metal dimer ion signals. 48

3.2 Species formed from an NIST 1190 high-temperature alloy that could interfere with molybdenum. 51

3.3 Molybdenum concentrations determined for an NIST 1190 reference material using various species. 52

4.1 Limits of Detection (LOD) of ^{60}Ni for Various Experimental Conditions 75

5.1 Apodization functions 87

Abstract of Dissertation Presented to the Graduate School of the University of
Florida in Partial Fulfillment of the Requirements for the
Degree of Doctor of Philosophy

ASPECTS OF MASS SPECTROMETRY: ISOBARIC INTERFERENCE SOLUTIONS AND QUANTITATION IN FOURIER TRANSFORM ION CYCLOTRON RESONANCE MASS SPECTROMETRY (FTICR-MS)

By

Kevin L. Goodner

December 1996

Chairperson: Dr. John R. Eyler
Major Department: Chemistry

The research in this dissertation was focused toward finding solutions to the isobaric interference problem seen in plasma source mass spectrometry with specific application to glow discharges.

Argides, dimers, and doubly charged metal ions were investigated as possible species to use for elemental quantitation in a glow discharge. These species responded similarly to the metal ion (atom) with regard to power (pressure). These species provided good quantitation (generally better than 15%) for elements with concentrations in the sample of 0.1% and above. The practical utility of this analytical scheme was evaluated by analyzing a standard as an unknown surrogate. Relative errors of approximately 50% for the M^+ analyte, due to polyatomic interferences, gave way to errors of approximately 15% when the MAr^+, M_2^+, and M^{+2} were used for quantitation.

A glow discharge (GD) ion source has been developed to work within the high magnetic field of a Fourier transform ion cyclotron resonance (FTICR) mass spectrometer. Characterization of this source revealed that the optimum operating voltage, pressure, and current are significantly lower than those for normal glow discharges. The sputter rate was 1/30th of that found with a normal glow discharge source operated external to the high magnetic field region. Operation of the GD source closer to the FTICR analyzer cell than with previous experimental designs resulted in improved ion transport efficiency. Preliminary results using this internal GD source have established detection limits in the low ppm range for selected elemental species.

An extensive survey of various methods for quantitation of peak intensities in FTICR-MS has been undertaken using a series of simulated ion transient response signals with varying signal-to-noise ratio. Both peak height (5 methods) and peak area (4 methods) were explored over a range of variables including data set size, apodization function, damping constant, and zero filling in an attempt to obtain an optimal methodology for quantitation. Optimal results over a range of signal intensities were achieved when using either Hanning, 3-term Blackman-Harris, or Kaiser-Bessel apodization functions, zero filling until the peaks of interest were represented by 10-20 points, and determining peak heights via a polynomial fit method.

CHAPTER 1
INTRODUCTION

Glow discharge mass spectrometry (GDMS) offers a distinct advantage over GD optical techniques for qualitative analysis of metals, because the resulting mass spectra are often easier to interpret. This is due to the relatively small number of isotopes of the elements as compared to the vast quantities of excited states possible in the elements. Also, isotopic patterns can be observed and identified easier in GDMS than with optical methods. The main disadvantage of glow discharge mass spectrometry is isobaric and polyatomic interferences seen in resulting mass spectra.

Isobaric interferences are isotopes of neighboring elements, or polyatomic species (MO^+, MAr^+, M_2^+, M^{+2}, Ar^+, ArO^+, Ar_2^+, etc.) that have nominally the same mass to charge ratio as the elemental isotope of interest. These species often interfere to such an extent that sensitive and accurate quantitative analyses cannot be performed. Isobaric interferences are the biggest problem seen in GDMS today. They are not unique to glow discharge mass spectrometry since they are seen in other plasma source mass spectrometry experiments such as inductively coupled plasma MS, microwave induced plasma MS, and radio frequency glow discharge MS.

For example, if a researcher wished to determine the iron concentration in an alloy, isobaric interferences could lead to problems. Iron has four naturally occurring isotopes: ^{54}Fe, ^{56}Fe, ^{57}Fe, and ^{58}Fe with relative abundances of 5.9, 91.7, 2.1, and 0.3% respectively. Obviously ^{56}Fe is the best choice for quantitation since it is by far the most abundant isotope. However, ^{56}Fe^{+} has the isobaric interferences of ^{40}Ar^{16}O^{+}, ^{28}Si$_2^{+}$ (92.2 %), and ^{112}Cd^{+2} (24.1 %). In order for ^{56}Fe^{+}, ^{28}Si$_2^{+}$, ^{112}Cd^{+2}, and ^{40}Ar^{16}O^{+} to be resolved in a mass spectrometer, a resolving power ($m/\Delta m_{1/2}$, mass of peak divided by full width at half maximum) of approximately 7,000 is required. ^{40}Ar^{16}O^{+} is a common species found in glow discharge mass spectrometry if any oxygen or water is present in the argon supply or in the sample as moisture or as an oxide. The next most abundant isotope of iron, ^{54}Fe, is obscured by ^{54}Cr (2.4%) and ^{27}Al$_2$ (100 %), with a mass resolving power of 74,000 required to resolve these interferences. After ^{54}Fe, ^{57}Fe is the next most abundant isotope and is interfered with by ^{114}Sn^{+2} (0.7%), ^{114}Cd^{+2} (28.7 %), and ^{40}Ar^{16}O^{1}H^{+}, requiring $m/\Delta m_{1/2}$ of 3,600 to resolve. This leaves the least abundant isotope of iron, ^{58}Fe as the species to use for quantitation. However, even if ^{58}Fe is uninterfered, it is 200 times less abundant than the major isotope of iron. Common interferants of ^{58}Fe are ^{58}Ni (68.3 %) and ^{116}Cd^{+2} (7.5 %) which require 28,000 mass resolving power for peak separation. While several of the isotopes and isobaric interferences in this example can be resolved using a magnetic sector instrument (^{56}Fe and ^{57}Fe requiring $m/\Delta m_{1/2}$ 7,000 and 3,600, respectively), the isobaric interferences for the two isotopes ^{54}Fe and ^{58}Fe (requiring $m/\Delta m_{1/2}$ of 74,000 and 28,000 respectively) are virtually impossible to resolve on most mass spectrometers. This simple example demonstrates the problematic nature of isobaric interferences and the pervasiveness of the problem.

Several techniques have been used to circumvent isobaric interferences. One technique attempts to perform a background subtraction. By measuring the intensity of the interferants without sample, a background is obtained that can then be subtracted from the spectrum of interest. A more common method is to try to minimize the isobaric interferences by using highly pure argon as the discharge gas with a 'getter' in-line which removes water (a problematic contaminant) from the gas delivery line. This provides a cleaner discharge and therefore fewer unwanted polyatomic species (oxides and hydrides), but this will not affect the isobaric interferences occurring from neighboring elemental isotopes. Many of the problematic polyatomic interferants can be eliminated by using high purity neon as the discharge gas in place of the more common argon. There are still polyatomic interferants containing the discharge gas, but these interferants have different masses since neon (^{20}Ne-major isotope) and argon (^{40}Ar-major isotope) have different masses.

Another approach is to utilize mass spectrometers with higher resolving power in an attempt to separate the interferants in the mass spectra. Since these isobaric interferants are not exactly identical in mass to the analyte of interest, it is possible to resolve the peaks if a mass spectrometer with sufficiently high resolving power is used. This approach has the distinct advantage that it is more universally applicable since interferant peaks from either isotopic or polyatomic species can be resolved.

What follows in this dissertation is a report of studies performed by this investigator related to solving the problem of isobaric interferences. First is a general discussion of glow discharges (used in the first and second studies), sector mass spectrometers (used in the first study), and Fourier transform ion cyclotron resonance mass spectrometers (used in the second and third studies).

After this instrumentation discussion, the first study is presented where species commonly considered interferants (metal argides, MAr^+; metal dimers, M_2^+ ; and doubly charged metals, M^{+2}) are used as the basis of quantitation of the metal concentration. Investigations into the trends of the signal intensities of these species as compared to the signal intensities of the parent metal are discussed, along with results when applying this method to a known and unknown sample.

The second study discussed is the design and implementation of high magnetic field glow discharge Fourier transform ion cyclotron resonance mass spectrometry (FTICR-MS). This design couples the ultra-high resolving power of FTICR-MS and the high ion transport efficiency of a GD source located within 25 cm of the ICR analyzer cell. With the resolving power of FTICR-MS (routinely >500,000 $m/\Delta m_{1/2}$) virtually every interferant can be resolved. Studies into the sputter rate, voltage, pressure, and current characteristics of the high magnetic field source are presented, along with results on limits of detection. This investigation implies that FTICR-MS is highly suited for glow discharge analysis when isobaric interferants are problematic.

The third project presented here entails a detailed investigation into the quantitation of ion abundances determined by FTICR-MS. This is of paramount concern if analytical analyses are to be performed using this type of mass spectrometry. Simulated transient response signals were analyzed using variables such as data set size, orders of zero filling, apodization function, and peak fitting techniques in order to establish the best methods for determining relative ion abundances. This project also involved application of the best methods for determining relative ion abundances to a real sample. The transient response signals for experimental confirmation were obtained using xenon, an isotope rich element. The nine isotopes of xenon are ^{124}Xe (0.10 %), ^{126}Xe (0.09 %), ^{128}Xe (1.91 %), ^{129}Xe (26.4 %), ^{130}Xe (4.1 %). ^{131}Xe (21.2 %), ^{132}Xe (26.9 %), ^{134}Xe (10.4 %), and ^{136}Xe (8.9 %). Only seven of the nine isotopes were investigated since ^{124}Xe and ^{126}Xe were not decernible from the noise.

Following a complete discussion of these 3 projects is an overall conclusion, discussing the projects and giving further suggestions for overcoming the isobaric interference problem.

CHAPTER 2
INSTRUMENTATION

Glow Discharge

Glow discharges are most commonly used for elemental analyses of solid, conducting samples. This is due to several factors inherent to glow discharges. Their low operating power and simplicity are major advantages over other techniques. Glow discharges are a subset of gas discharges, and are a type of plasma. If a sufficiently high voltage is applied to two electrodes in an atmosphere of gas, the gas will break down and form electron-ion pairs, permitting current to flow. Glow discharges typically operate using a reduced pressure (0.1-10 Torr) of a gas (commonly noble gases, especially argon), voltages from 500 V to 2000 V, and currents of 5 mA to 100 mA.

The electric field in a glow discharge is typically achieved by using a power supply to apply a negative potential to the sample for the cathode and using the grounded discharge housing as the anode. This electric field at the appropriate voltages and pressures will initiate a glow discharge. There are typically eight regions in a glow discharge. These eight regions are shown in Figure 2.1 along with the corresponding electrostatic potentials and charged particle distributions [1].

The three most important regions of the discharge in glow discharge analyses are the cathode dark space, the negative glow, and the Faraday dark space. The cathode dark space

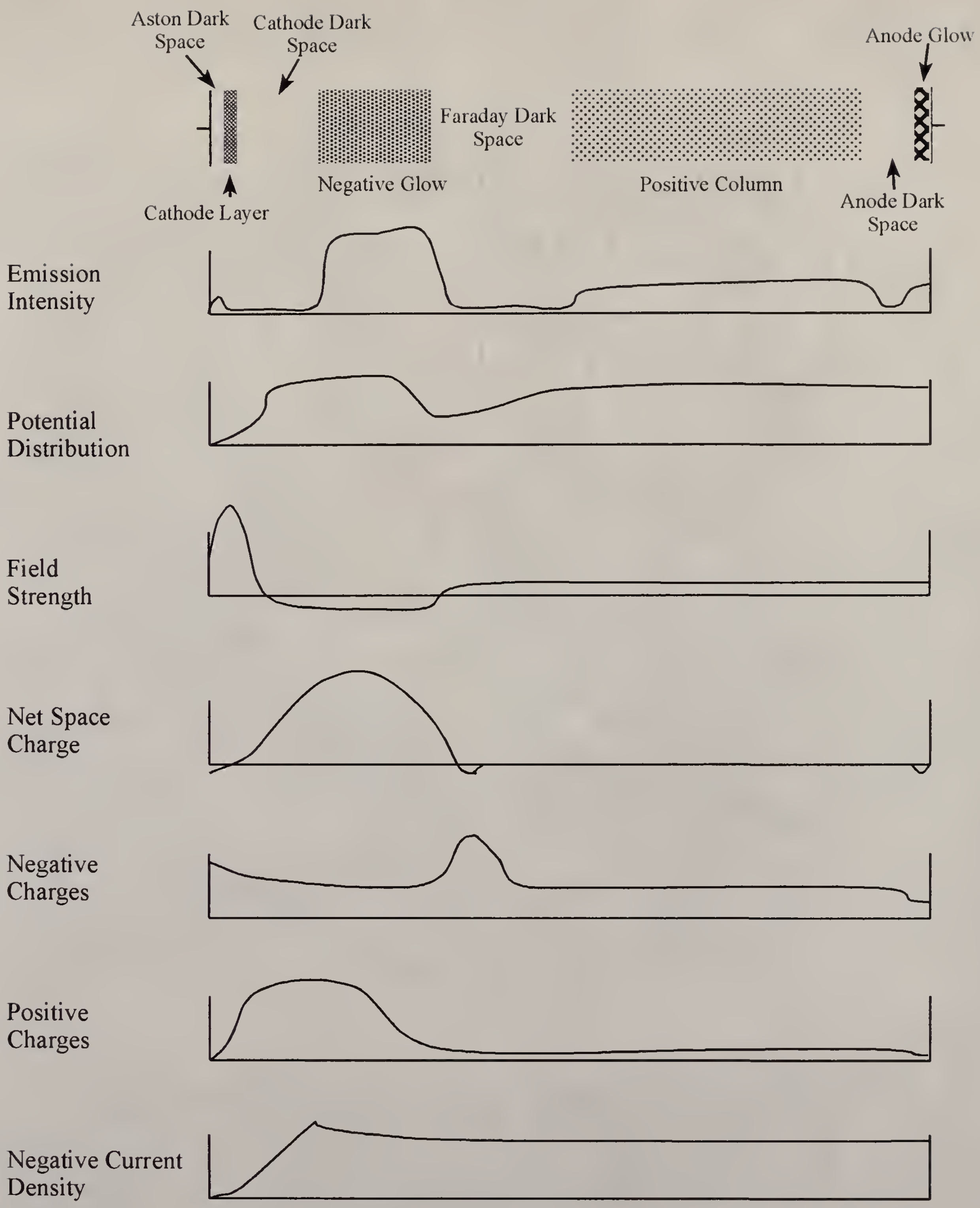

Figure 2.1: Properties of the different regions of a glow discharge [1].

results from the creation of a positive space charge near the cathode where the majority of the potential is dropped across a narrow distance. The next region, the negative glow region, is where the discharge "glows" due to gas-phase excitations, subsequent emissions, and ionizations. This region is where the the bulk of analytically important processes occur, due to the collision rich environment. This region has a higher concentration of positive charge (see Fig 2.1) and is where sampling occurs in GDMS. The Faraday dark space has a high concentration of negative charges balancing the positive charges in the negative glow. Glow discharge chambers are commonly constructed to contain only the cathode dark space and negative glow regions since the bulk of analytical information is contained in these regions.

The spatial diversity in glow discharges can easily be seen in Figure 2.1 [1]. The glow discharge plasma varies greatly in composition and, therefore, analytical usefulness in each region. Sample position, and therefore sampling region, is critical for quality analyses. Thus, it is often necessary to optimize the probe position before performing any analyses. Furthermore, as the sample is sputtered during analysis, optimum sample probe position may change over time (hours) and with it the analytical signal which may be observed.

Cathodic sputtering is the mechanism by which atoms of the sample are converted from the solid phase to the gas phase so that they may be analyzed. Cathodic sputtering occurs when positive ions in the negative glow region near the cathode dark space and the negative glow boundary are accelerated across the cathode dark space and impact the surface of the sample. When these positively charged ions collide with the sample surface, their kinetic energy is transferred into the lattice energy of the sample and this can dislodge sample atoms into the gas phase. This process can be imagined to be much like a meteor striking the earth, creating a crater, and ejecting dirt (sample) into the air. This is illustrated in Figure 2.2. One can see the effects of the meteor (positive ion) as it impacts the earth (sample). This impact not only ejects atoms from the sample, but also secondary electrons, positive and negative ions, and photons. Positive ions return to the sample surface due to the electric field, and the negative ions and electrons are accelerated away from the sample by the same field. These other species are minor in comparison to neutral atoms which diffuse to the negative glow region where a fraction of the atoms are ionized.

Since glow discharges operate with around 1 Torr of discharge gas, collisional processes account for excitation and ionization of species in the plasma. These species are excited and ionized through inelastic collisions which possess either kinetic or potential energy [2]. Collisions where kinetic energy is transferred are called ‘collisions of the first kind’ and where potential energy is transferred ‘collisions of the second kind’ [3]. These two methods of excitation are detailed in Table 2.1. The relative importance of the two methods depends upon operating conditions (voltage, current, pressure, and geometry of the discharge chamber) of the glow discharge. Of the five ionization methods listed in Table 2.1, Penning ionization is the method responsible for the majority of ions produced in the typical glow discharge [4-8].

Penning ionization is the transfer of energy from a metastable discharge gas atom to an atom or molecule. If the excitation energy of the metastable atom is greater than the ionization potential of the atom or molecule, ionization can occur. Metastable states are created through the excitation of the discharge gas and for argon the two metastable states have energies of 11.55 eV and 11.72 eV. Under normal discharge conditions the argon metastables have

Table 2.1. Glow Discharge Ionization Processes [3].

Collisions of the first kind	
Electron ionization	$A + e^- \rightarrow A^+ + 2e^-$
Collisions of the second kind	
Penning ionization	$Ar^m + X \rightarrow Ar + X^+ + e^-$
Associative ionization	$Ar^m + X \rightarrow ArX^+ + e^-$
Symmetric Charge exchange	$A^+ + A \rightarrow A + A^+$
Asymmetric charge exchange	$A^+ + B \rightarrow A + B^+$

A, B, X, neutral gas phase species; Ar^m, metastable argon atom; e^-, electron

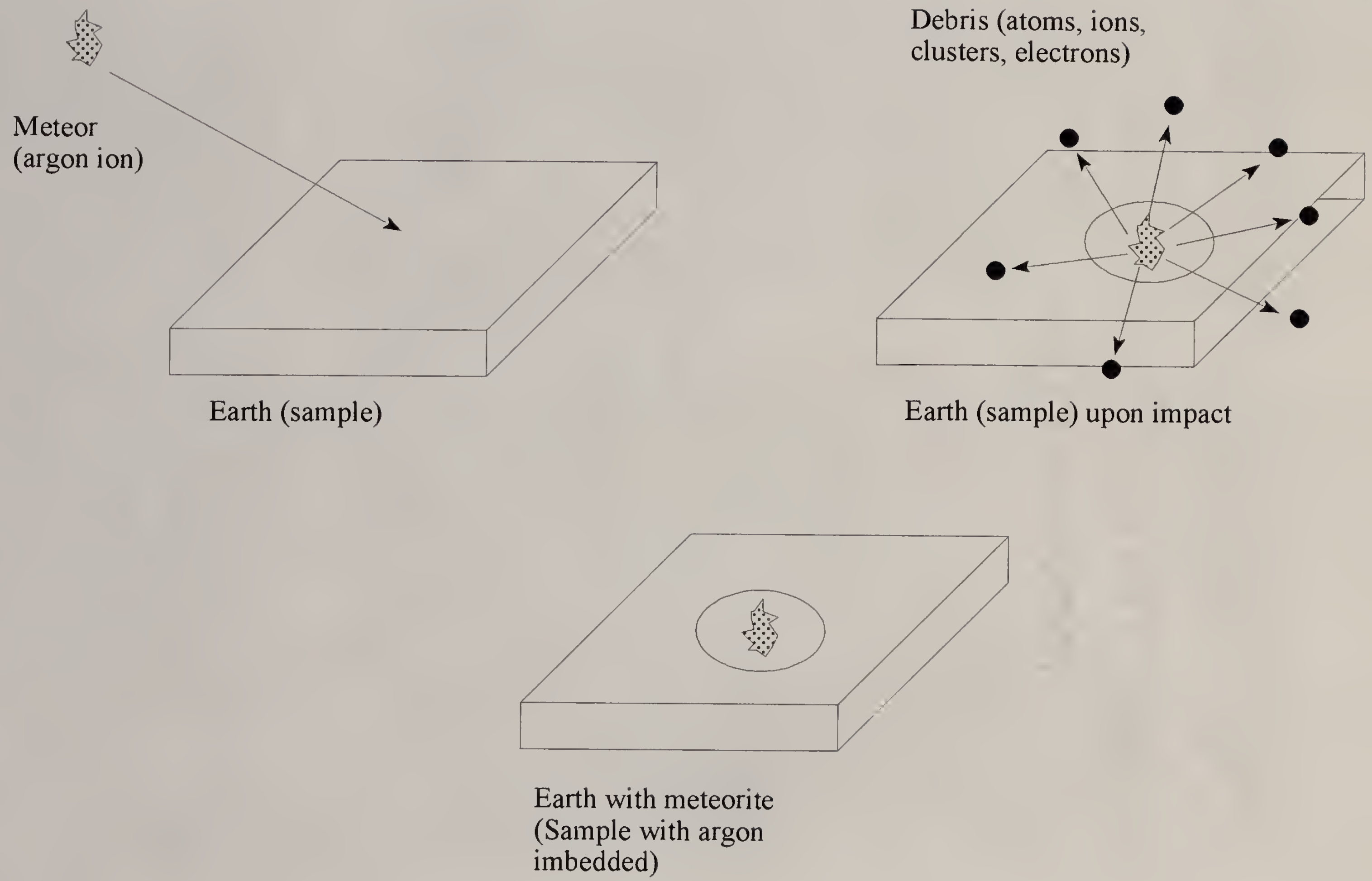

Figure 2.2: Graphical representation of a meteor (argon ion) striking the earth (sample).

lifetimes of milliseconds [9]. With this energy they can ionize all but 11 of the first 92 elements in the periodic table. Table 2.2 shows the metastable energies of the noble gases. After ionization of analyte atoms in the negative glow region via Penning ionization, they exit a small sampling orifice and are extracted by electrodes into the mass spectrometer. This provides a mass spectrum consisting of various ions with differing relative intensities. Quantitation using such a mass spectrum is not as straightforward as it is for many other analytical methods. For instance, a typical calibration curve is much more difficult to construct since it is often difficult to find a series of certified alloys with analyte concentrations which vary over a sufficient range. When different matrices, differential atomization and ionization efficiencies, ion transmission, and ion sensitivity are also considered, it is readily apparent that quantitation is not as simple as for many techniques where liquid samples are used [10].

Often it is necessary to use only a small handful of standards for quantitation. Most quantitative analyses in glow discharge mass spectrometry use relative sensitivity factors (RSFs). The RSF of an analyte is

$$RSF_{\frac{A}{B}}=\frac{\left(\frac{I_A}{C_A}\right)}{\left(\frac{I_B}{C_B}\right)}$$

where the sensitivity (intensity, I, per unit concentration, C) of the analyte, A, is ratioed with the sensitivity of the reference element, B [11]. It is important to note that if the sample is relatively pure with only trace amounts of other elements then one assumes that the sample

Table 2.2. Metastable energies of noble gas atoms. [1]

Gas	Metastable Energy, eV
He	19.8, 20.7
Ne	16.6, 16.7
Ar	11.5, 11.7
Kr	9.9, 10.5
Xe	8.3, 9.4

behaves like the pure element. However, if the sample contains large percentages of several elements then the reference sample should be matched as closely as possible to the sample. This means that the researcher must first perform a semi-quantitative analysis to determine the approximate concentrations of the constituents of the sample before choosing a reference.

An alternate approach to quantitation is to use ion-beam ratios (IBRs) [12]. This method determines the concentration of the analyte by summing all the ionized sputtered species and then determining the fraction the analyte signal compared to the whole signal, which could be related to the concentration of the analyte. This method does not take differing sensitivities of the elements into consideration and therefore is used for semi-quantitative analyses. If RSFs are used in conjunction with IBRs then quantitative analytical analyses are possible.

Sector Mass Spectrometers

Sector instruments use magnetic and/or electrostatic fields to separate ions. A magnetic field can separate ions by dispersing monoenergetic ions across a focal plane [13]. The radius of the curved ion path, r_m (cm), through the magnetic field is

$$r_m = \left(\frac{143}{B}\right)\left(\frac{mV}{z}\right)^{\frac{1}{2}}$$

where *B* is the magnetic field strength in gauss, *m* is the atomic mass of the ion, *V* is the acceleration voltage applied to the ion, 143 is a collection of physical constants, and *z* is the number of charges on the ion [14]. A mass spectrum is obtained by either collecting all of the dispersed ions on a photographic plate or array detector, or, more commonly, by scanning the magnetic field or acceleration voltage and using a single detector. Resolution is determined by the focusing of the ions on the detector, which is in turn determined by the width of the ion slits in the mass spectrometer. This means that resolution and sensitivity are inversely proportional. Recalling the example from the introduction of iron in a metal alloy, it was stated that 2 isotopes of iron (^{56}Fe and ^{57}Fe) could be resolved using a mass sector instrument. This inverse proportionality of resolution and sensitivity is critical in this case. In order for the needed resolution to be obtained, it is often the case that only the major isotope can be examined. The loss of sensitivity coupled with the lower concentration of the isotope (factor of 45 in this example) can preclude its use as an analyte. A rule of thumb in mass sector instruments is in order to double the resolution, the sensitivity is decreased tenfold.

Magnetic sector instruments are often coupled with an electric sector in order to improve resolution. These double focusing mass spectrometers can have either the magnetic sector followed by the electric sector (B-E), or the electric sector followed by the magnetic sector (E-B). The practical resolution available with such a double-focusing sector mass spectrometer is approximately 4000 with acceptable sensitivity [14]. Figure 2.3 is an illustration of the magnetic sector instrument used for the work described in Chapter 3. This is a commercial glow discharge mass spectrometer. It has several key features that make it especially useful for GD-MS. It is a double-focusing sector instrument (B-E), and therefore

Figure 2.3: An illustration of the magnetic sector instrument used for the work described in Chapter 3.

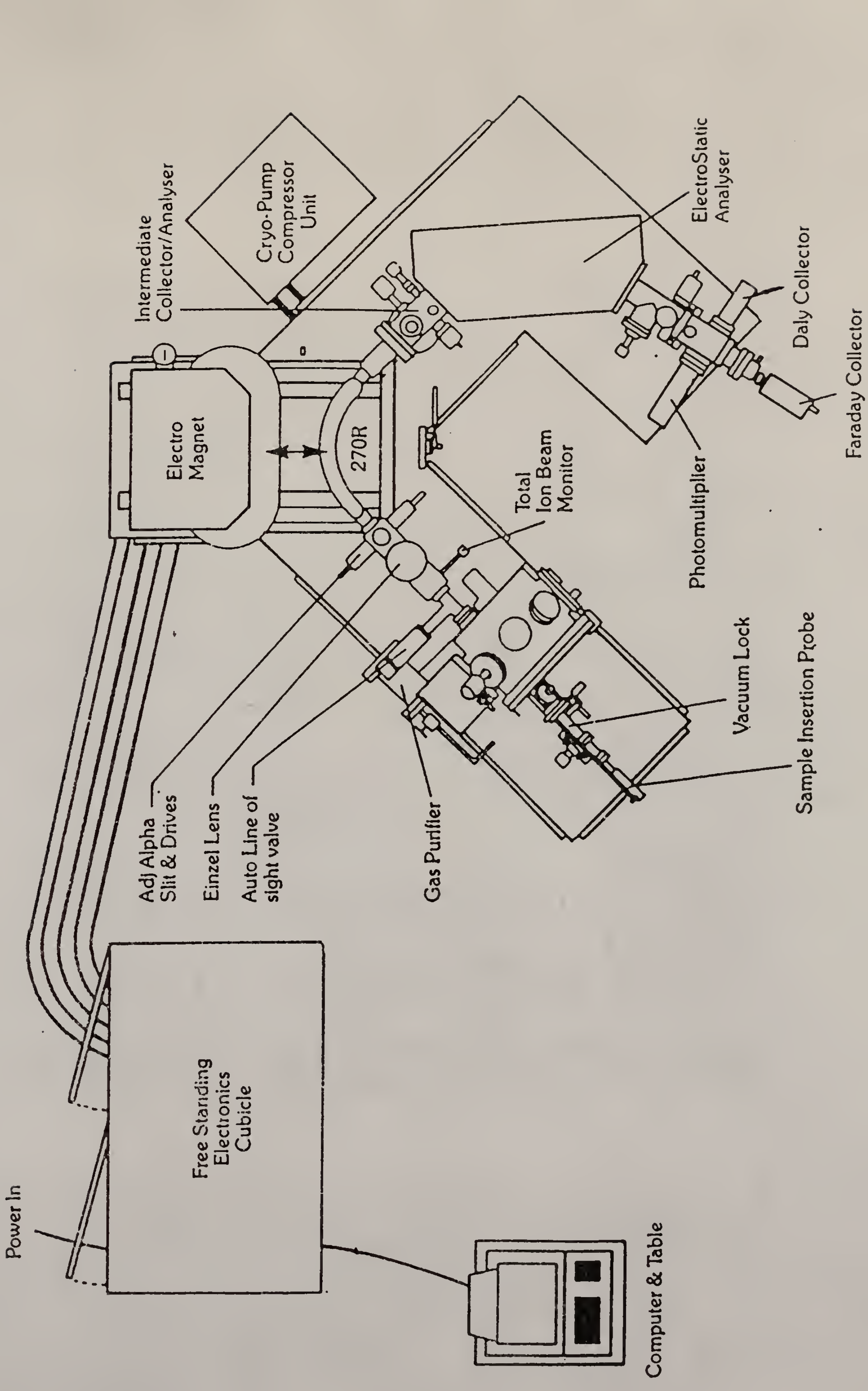
Power In
Free Standing Electronics Cubicle
Computer & Table
Adj Alpha Slit & Drives
Einzel Lens
Auto Line of sight valve
Gas Purifier
Intermediate Collector/Analyser
Cryo-Pump Compressor Unit
Electro Magnet
270R
Total Ion Beam Monitor
Vacuum Lock
Sample Insertion Probe
Photomultiplier
ElectroStatic Analyser
Daly Collector
Faraday Collector

has high enough resolution to separate many interferant peaks from the analyte. The dual detector system (Faraday cup and Daly detector) enables the instrument to quantitate analyte species over many orders of magnitude (generally 6 orders of magnitude). The instrument used a cryogenically cooled discharge chamber and an inline 'getter' for the argon in order to minimize polyatomic species. The biggest disadvantage of this instrument is the size and cost. The instrument occupies a space of approximately 5 m x 5 m, and costs several hundred thousand US dollars.

Fourier Transform Ion Cyclotron Resonance Mass Spectrometry

History

The basic principles of ion cyclotron resonance mass spectrometry (ICR-MS) were published by Lawrence and Livingston in 1932 when they showed that ions in a magnetic field could be accelerated to higher energies by applying an electric field of the same frequency as the cyclotron frequency of the ions [15]. Sommer et al. developed the first practical ion cyclotron resonance mass spectrometer, called the Omegatron, in 1949 [16]. Early ion cyclotron resonance instruments had slow scan speed, low resolution, and limited mass range [17-22]. However, these draw backs were improved dramatically in 1974 when Marshall and Comisarow applied the technique of Fourier transformation to ICR-MS, which improved the sensitivity, used a 'chirp' excitation that excites the ions virtually simultaneously, and allowed a complete mass spectrum to be obtained simultaneously within a fraction of a second [23-25].

The next two major steps in the evolution of FTICR-MS were in 1980 when superconducting magnets began being used and in 1981 when the instruments first became commercially available [26]. Higher magnetic field magnets improved characteristics of FTICR-MS by providing ultra-high mass resolution, wider mass range, higher mass accuracy measurements, and improved ion storage [26]. Since the early 1980s many improvements have been made to FTICR-MS instrumentation. Improved vacuum systems, higher field magnets (currently a 7 Tesla magnet is 'standard' and as high as 20 Tesla), improved analyzer cell designs, and the use of faster computers and better software for the instrument have transformed the FTICR-MS into a mainstream mass spectrometric tool. The history and progress of FTICR-MS has been described in several review articles [27-30].

Ion Trapping

Several papers and books have discussed the basic theory of FTICR-MS [31-34]. The first step in FTICR-MS is ion formation. Ion formation and ion transfer are discussed in the subsequent sections of this work. These ions are trapped in the analyzer cell which isolated in the middle of a superconducting magnet in a high quality vacuum. The pressures generally used in FTICR-MS are on the order of 10^{-8} Torr (considered poor vacuum), to 10^{-9} Torr (considered average vacuum), to 10^{-10} Torr or lower (considered excellent vacuum). Obtaining such vacuum obviously adds to the complexity and cost of FTICR-MS. In a magnetic field only ions with velocity components that are not parallel to the magnetic field are deflected into circular motion. In order for ions to be in a stable circular orbit, the magnetic or Lorentz force experienced inward must be equal to the centrifugal force exerted outward. The Lorentz (magnetic) force inward is

$$\mathit{Lorentz\ force} = qvB$$

and the centrifugal force outward is

$$\mathit{Centrifugal\ force} = \frac{mv^2}{r}$$

where q is the charge on the ion, v is the velocity of the ion, B is the magnetic field, m is the mass of the ion, and r is the circular radius of the ion. In a stable orbit, these two forces are equal and can be shown as

$$qvB = \frac{mv^2}{r}$$

$$\frac{qB}{m} = \frac{v}{r} = \omega_c = 2\pi f_c$$

$$f_c = \frac{qB}{2\pi m}$$

where ω_c is the cyclotron frequency in radians per second and f_c is the cyclotron frequency in Hertz. Notice that this equation shows that the mass to charge ratio of the ion, and its cyclotron frequency are inversely related.

A typical analyzer cell has six plates. Two are perpendicular to the magnetic field, in order to trap the ions along the z-axis (parallel to the magnetic field), since the cyclotron motion of the ions does not affect the motion of the ions in the z direction. These ‘trap’ plates generally are held at 1-2 V in order to keep the ions from escaping the cell. In addition to the

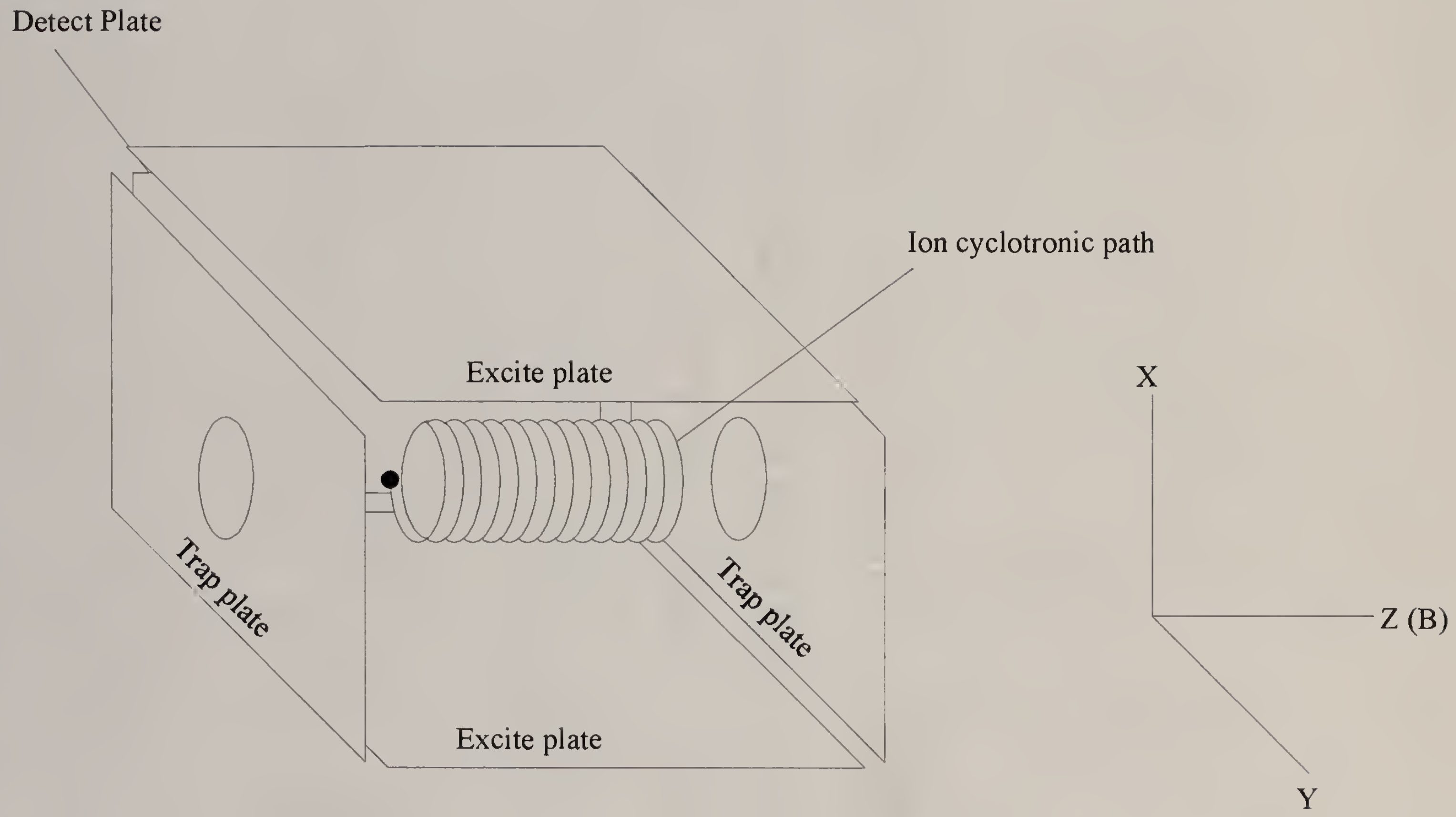

Figure 2.4: The typical FTICR-MS analyzer cell. The detect plate nearest the viewer has been removed for clarity. An example of ion cyclotronic motion is also displayed.

trap plates there are two excite plates and two detect plates that are parallel to the magnetic field. These six plates can be seen in Figure 2.4.

The trapping plates which are used to contain the ions in the z direction create two other types of ion motion in addition to the cyclotron motion. The first is due to ion oscillation between the trapping plates. This motion is termed the 'trapping' motion and is characterized by

$$\omega_T = \left[\frac{4q(V_T - V_o)}{ma^2}\right]^{1/2}$$

where ω_T is the trapping frequency, q is the charge on the ion, V_T is the trapping potential, V_o is the potential on the side plates, m is the mass of the ion, and a is the length of the cell (assuming a cubic cell) [35]. This motion depends upon cell geometry (usually cubic, rectangular, or cylindrical) [36].

The second induced ion motion is called the 'magnetron' motion. This motion is a combination of trapping and cylcotron motions. This motion leads the center of the cyclotron orbit along a wider path which follows the equipotential surfaces within the analyzer cell. This magnetron motion can be characterized by

$$\omega_M = \frac{2(V_T - V_o)(\alpha\lambda)^{1/2}}{a^2B}$$

where ω_M is the magnetron frequency, α is 2.185 V for a cubic cell, λ is 6.75 x 10^{-3} V for a cubic cell, and V_T, V_o, a, and B have been defined previously [35].

These two motions have frequencies much lower than the cyclotron frequency and are therefore generally ignored in a simple explanation of the ICR processes. Using an example from the Sharp et al. paper [35], an argon ion in a 7 Tesla field, 1 volt trapping potential, 2.54 cm cell, -0.5 V on V_o, and a cubic cell would have a cyclotron frequency, f_c, of 2.69 MHz, a trapping frequency, f_T, of 19.4 kHz (0.722 % of f_c), and a magnetron frequency, f_m, of 60 Hz (0.00223 % of f_c) [35].

Ions may be trapped in the analyzer cell for long periods of time. Routinely ions are held in the analyzer cell for approximately one second; however trapping times of seconds, minutes, and even hours have been reported. If the trap plates have a significantly high potential applied to them then observed cyclotron frequencies may shift due to the trapping frequency coupling with the cyclotron frequency. Other factors that can contribute to a shift of the observed ion frequency are the electric field produced by the space charge characteristics of the ions, magnetic field inhomogeneity, and collisional damping.

Ion Excitation

Once the ions are trapped within the analyzer cell, they must be excited and detected. The ions are accelerated to larger cyclotron orbits by applying an rf pulse to the two opposing ‘excite’ plates. This also drives the ions into distinct ion packets and coherent cyclotron motion. If sufficient energy is applied to an ion of a particular m/z, its cyclotron orbit will exceed the spacing between the walls of the analyzer cell and it will thus be ejected from the cell.

There are three common methods used for ion excitation. The first is a single frequency excitation, as was used for the initial FTICR-MS studies reported by Comisarow and Marshall [23]. This method provides a flat excitation power only over a narrow frequency range. Consequently, this method of excitation is normally only used in narrow band FTICR-MS experiments where the ions of interest have cyclotron frequencies within a few kilohertz of each other.

The most common method of ion excitation today is the so-called 'chirp' excitation. This chirp is a lower power, but longer duration, fast frequency sweep, as was suggested by Comisarow and Marshall [24]. Chirp excitation is generated via a frequency synthesizer over a typical range of ~20 kHz to ~5 MHZ for approximately 1 ms. The frequencies are scanned from higher frequencies to lower, because at sufficiently low frequencies the ions behave as if there were a dc offset on the excite plates instead of a frequency which would have deleterious effects to ions of small cyclotron orbits with low mass. The main disadvantage of chirp excitation is nonuniform excitation of the ions. This problem is most dramatic at the edges of the frequency range used in the chirp excitation. Also, since the chirp is a sweep of frequencies, the different mass ions are excited at slightly different times, which can cause peak height distortion due to space charge effects. In addition to these problems, it has been shown that the z-axis component of the chirp excitation can accelerate ion trapping motions as well and can cause ions to be ejected from the analyzer cell along the z-axis [37].

A relatively new approach used to excite ions in FTICR-MS is Stored Waveform Inverse Fourier Transform (SWIFT), which was introduced by Marshall et al. in 1985 [38]. The excitation waveform is generated by taking the desired power spectrum for ion excitation and performing an inverse FT to give a time-domain signal. This waveform is then applied to the excite plates via a digital frequency synthesizer. The SWIFT technique allows almost any excitation frequency pattern to be applied to the excitation plates. The common uses of SWIFT are for providing flat power to the ions for more accurate peak heights, flat power with windows for ejecting desired ions from the cell, or to selectively excite one or more ions.

After excitation the ions have a cyclotron radius, r_c, of

$$r_c = \frac{Et}{2B}$$

where E is the excitation electric field, t is the width of the excitation pulse, and B is the magnetic field strength. If excitation is to provide reasonable results all the ions must be accelerated to the same cyclotron radius so that the peak intensities represent the ion abundances in the cell.

A common use of FTICR-MS is to excite ions of a particular mass to a larger orbit, which increases the velocity of the ions, and then to allow the higher kinetic energy ions to collide with a gas which has been introduced in the cell, thus leading to ion fragmentation. These fragmented ions may then be excited and detected. Using this technique it is possible to obtain a mass spectrum of fragment ions from any peak in a mass spectrum. This is termed MS/MS. The ability to perform multiple stages of mass spectrometry (MS^n) is one of the advantages of FTICR-MS.

Ion Detection

Once the ions have been excited, an image current is induced on the detection plates as the ions circulate in the cyclotron orbit. An image current is induced when the ion packet (usually positively charged) approaches a detect plate and electrons move from the opposite detect plate to the detect plate close to the ion packet. As the ion packet orbits there is a periodic flow of electrons from one detect plate to the other and back again. This image current is defined by

$$I = \frac{Nqv}{d}$$

where N is the number of ions, q is the charge of the ion, v is the velocity of the ions, and d is the distance between the detect plates [39, 40]. This oscillating current is passed through an impedance and converted to an oscillating voltage. The voltage signal is a composite of the the cyclotron frequencies of the ions present in the analyzer cell. This signal is amplified and digitized to give a voltage vs. time function called a transient response signal.

Two methods are commonly employed in FTICR-MS to acquire the transient response signal: 'broadband' and 'heterodyne' modes. In broadband mode the signal is digitized directly by an analog to digital converter. The rate of signal digitization must be at least twice the highest frequency for which information is desired. The signal is digitized until either the digitizer's random access memory (RAM) is full or until the signal has disappeared due to collisional damping. With the frequencies and amount of RAM commonly found in current digitizers, the RAM is most often filled before the signal degenerates.

The other method of signal acquisition is the ‘heterodyne’ mode. This method is used in order to reduce the digitization rate so that the time of acquisition can be increased, therefore increasing frequency resolution. Higher frequency resolution implies higher mass resolution, higher signal to noise ratios, and better mass accuracy but with a narrow frequency (mass) range. Heterodyne mode works by mixing the acquired signal with a reference signal and then by use of mixing devices the needed frequency of digitization is lowered. Heterodyne mode, however, is a technique that is not needed if the signal is short lived or if the digitizer has sufficient RAM to acquire larger transient response signals. A major shortcoming to heterodyne mode is that the frequency range (and thus mass range) that can be obtained is very narrow whereas, the broadband technique can obtain a mass spectrum of ions with m/z from the low teens to several thousand.

Multiple signals may be acquired and summed in order to increase the signal-to-noise ratio. Transient response signals contain 2^n data points. The most common data set sizes used today are 16K, 32K, 64K, 128K, and 256K (where K=1024). This is required for the fast Fourier transformation (FFT) algorithm described by Cooley and Tukey [41]. Some researchers are discussing using ultra-large data set sizes so that only broadband mode needs to be used, but with all the advantages of heterodyne mode (ultra-high mass resolution, higher signal-to-noise, and better mass accuracy). The FFT converts the time domain voltage signal into a frequency based spectrum. Using mass calibration equations the frequency spectrum can be converted into a mass spectrum.

Mass Accuracy and Resolution

Fourier transform ion cyclotron resonance mass spectrometry is capable of determining the mass of an ion very accurately. This is due to the fact that frequencies can be determined very accurately and they are inversely related to mass in this technique. Exact mass measurement is critical for accurate and unambiguous determination of the composition of an ion. This is required for unknown analysis in many areas of science, including synthetic chemistry. Mass accuracy is described as the parts-per-million (ppm) error in determining the mass of an ion. It can be calculated by

$$Mass\ Error(ppm) = \frac{|correct\ mass - measured\ mass|}{correct\ mass}\ x\ 10^6$$

Mass errors in the low ppm range are common in FTICR-MS.

In order for the frequency spectrum to be converted into a mass spectrum, a calibration equation must be used. Many equations have been suggested, but only a few are commonly used. The simplest equation (and least used) is a rearrangement of an earlier equation. Rearranging

$$f_c = \frac{qB}{2\pi m}$$

to

$$\frac{m}{q} = \frac{B}{2\pi f_c}$$

$$\frac{m}{q} = \frac{a}{f_c},\ a = \frac{B}{2\pi}$$

the simplest calibration equation is obtained. However, this method does not take second order effects in account due to trapping fields, and equations such as

$$\frac{m}{q} = \frac{a}{f_c} + b$$

$$\frac{m}{q} = \frac{a}{f_c} + \frac{b}{f_c^2}$$

$$\frac{m}{q} = \frac{a}{f_c} + \frac{b}{f_c^2} + \frac{c}{f_c^3}$$

have been used by different commercial instrument manufacturers [42]. The second term in the above equations can be related to the trapping voltage applied to the trap plates. The constants *a*, *b*, and/or *c* are obtained by obtaining a mass spectrum (and thus ion frequencies) of a compound, such as perfluorotributylamine (PFTBA), with precisely known masses. It is possible to solve a series of equations and unknowns to determine the constants a, b, and/or c. Since the frequencies of ions can shift due to the trapping field produced by the trap plates, it is necessary to calibrate the mass spectrometer at a trap voltage equal to that used in the experiments with compounds of unknown mass. Some researchers have been attempting to circumvent this problem. Watson et al. have shown some good results by collecting a series of mass spectra at varying trapping potentials, and extrapolating to zero trapping potential to obtain calibration independent of trapping potential [43].

Another strong point of FTICR-MS is its capability for obtaining ultra-high mass resolution spectra. It is generally agreed that FTICR-MS has the highest resolving power of any type of mass spectrometer. Resolving power in FTICR-MS instruments is defined by

$$\frac{m}{\Delta m} = \frac{qBt}{m}$$

where m is the mass of the ion, Δm is the full width at half maximum (FWHM) of the peak, q is the charge of the ion, B is the magnetic field, and t is the length of the transient response signal [44]. It is apparent that the resolving power in FTICR-MS is directly proportional to the magnetic field strength, and also to the amount of time that the coherent motion of the ion packet can be observed. This means that high resolution spectra are commonly performed in heterodyne mode in order to increase the time of signal acquisition. It is fairly common to see FTICR-MS mass spectra with resolution greater than 1,000,000 and as great as 400,000,000.

The high mass accuracy, ultra-high mass resolution, ability to store ions, ability to perform multiple stages of mass spectrometry (MS^n), ability to perform collisionally induced dissociation, and ability to study ion/molecule reactions are some of the major advantages of FTICR mass spectrometry. However, nothing is without its disadvantages. Among FTICR-MS's disadvantages are: cost (instruments cost ~ $100,000 to > $1,000,000 plus the operating costs due to cryogens), size, need for skilled operators, complexity (the high vacuum, electronics, acquisition software, ion formation, and ion transport), space charge limited dynamic range (the cell can only hold approximately 10^6 to 10^7 ions), and the fact that signal acquisition can take from a few hundred milliseconds to several seconds, thus hampering the duty cycle of the instrument.

CHAPTER 3
ELEMENTAL QUANTITATION BASED ON ARGIDES, DIMERS, AND DOUBLY CHARGED GLOW DISCHARGE IONS

Introduction

As stated previously, a limitation to absolute quantitation in glow discharge mass spectrometry (GDMS) is the presence of polyatomic interferences [45,46]. Unlike sputtered analyte atoms, these species are not an inherent part of the sample cathode but are continuously created and destroyed in the collision-rich negative glow. Three principal species derived from the discharge gas are involved in collisions: free electrons, atoms in excited electronic states, and the ions themselves [47]. Two primary ionization mechanisms, electron impact and Penning (metastable), and several secondary ionization mechanisms, whose role is believed to be less significant [48], provide the conventional analyte of interest (metal ions).

Argides (MAr^+), dimers (M_2^+), oxides (MO^+), and doubly charged species (M^{+2}) are formed in the plasma in addition to the singly charged ions normally used in an analysis. While the relative abundance of these species varies with the matrix, they comprise a large enough fraction of the total ion population that glow discharge practitioners are often forced to suppress [49], eliminate [50,51], or discriminate [52] against them during an analysis. While all of these schemes are employed to varying degrees, mass discrimination has met with the most success, due in part to the availability of high resolution commercial instrumentation [53].

The magnetic sector glow discharge mass spectrometer, most popular among these instruments, is capable of providing mass resolution on the order of 6000 - 20000 ($m / \Delta m_{1/2}$), high enough to separate many interferences from species of interest. Several prototype Fourier transform mass spectrometers have been shown to be useful for mass discrimination, exceeding the capabilities of the magnetic sectors by an order of magnitude or more [54-56]. Using these instruments, one is able to resolve the masses of nearly all interfering species from the analyte ions of interest. Often, however, the success of this approach is lessened by a loss of transmission (sensitivity), an increase in instrumental complexity, and the cost.

As an alternative to the classical approach of discriminating against polyatomic interferences, this chapter reports efforts to use metal argide ions, metal dimeric ions, and doubly-charged metal ions as alternatives to using singly-charged ions for quantitation. Although the use of species other than the singly-charged ions for elemental quantitation is novel in GDMS, it is not new in other types of mass spectrometry; the use of doubly-charged ions is common in spark source mass spectrometry (SSMS) [57], and an investigation in secondary ion mass spectrometry (SIMS) [58] demonstrated in-situ analysis of rare earth elements with good precision and limits of detection of < 15 ppb for most elements. The success realized by using these species is due in part to their relatively high abundance in SSMS and SIMS [59]; in a glow discharge, the doubly-charged species are known to be a much lower fraction of the singly-charged species than in these other techniques, and their usefulness is as yet unproven.

After examining the parameters that influence the relative populations of the metal argides, metal dimers, and doubly-charged metal ions, their analytical usefulness was evaluated by measuring the precision and accuracy of an analysis when they were employed. A high temperature alloy standard was analyzed as a surrogate for an unknown to evaluate the methodology.

Experimental

A VG9000 reverse Nier-Johnson geometry glow discharge mass spectrometer (FI Elemental Ltd., Winsford, Cheshire, U.K.) was used in these studies. At peak performance, resolution exceeds 7000 (FWHM) at an accelerating voltage of 8 kV. The linear dynamic range is in excess of 10^9 (via a combination of Faraday and Daly detectors). In this study, the resolution was deliberately kept at a nominal 5000 (FWHM) to improve ion transmission.

The discharge support gas was high purity argon, passed through a heated active-metal getter system into the discharge cell. The cell was cooled to approximately -130 °C to aid in the reduction of oxygen-containing species formed by reaction with water. The discharge was operated at 2 mA and 2000 V, except during pressure and power studies. The ion source chamber pressure was 8 mPa unless varied in a particular study; the cell pressure, although not measured directly, was approximately 10^4 times higher than the source pressure.

Cathodes were machined from pins 2.0 mm in diameter by 18.0 mm in length, with 8 mm exposed to the discharge. For signal optimization and method testing, National Institute of Standards and Technology (NIST) standard reference materials (SRMs) 601, 602, 603, and 604 were used. To gauge the usefulness of this method, two Ti:Cr:Mo high-temperature alloy standards (NIST 644 and 1190) were analyzed as a standard and an unknown, respectively.

Prior to analysis, all of the samples were sputtered for 30 minutes to remove surface contaminants and improve discharge stability.

Results and discussion

Figure 3.1 shows four spectra that illustrate the copper doubly-charged (a), copper metal (b), copper argide (c), and copper dimer (d) ions obtained from an aluminum pin (~4% copper) in a discharge operating under conditions favorable to analysis. If the metal is taken as 100%, the argides comprise 29%, the dimers 1.4%, and the doubly-charged ions 0.01% of the metal ion population. These results, typical in these experiments, are strongly influenced by the operating parameters of the discharge.

In GDMS the influence of discharge power and pressure on the M^+ species is well documented [60, 61]. However, little has been done to evaluate the effect these parameters have on the other species found in the discharge (argides, dimers, oxides, hydroxides, doubly-charged species, etc.) [46,60]. Prior to any analysis, it is prudent to optimize signal intensity by varying pressure, power, and ion focusing conditions. Since the species of interest depend not only on the number of sputtered atoms, but also on the density of other gas phase analytes, the collision frequency in the plasma, and on other factors, such optimization is crucial. It is highly desirable to operate in a region of the power and pressure regimes where small variations won't produce dramatic changes in ion signal intensities. If such changes are observed (see, for example, Figure 3.2a), one must at least be assured that the species of interest vary in the same manner as the reference species.

Figure 3.1: Glow discharge mass spectra of four species formed from a copper cathode: (a) Cu^{+2}, (b) Cu^{+}, (c) $CuAr^{+}$, and (d) Cu_2^{+}.

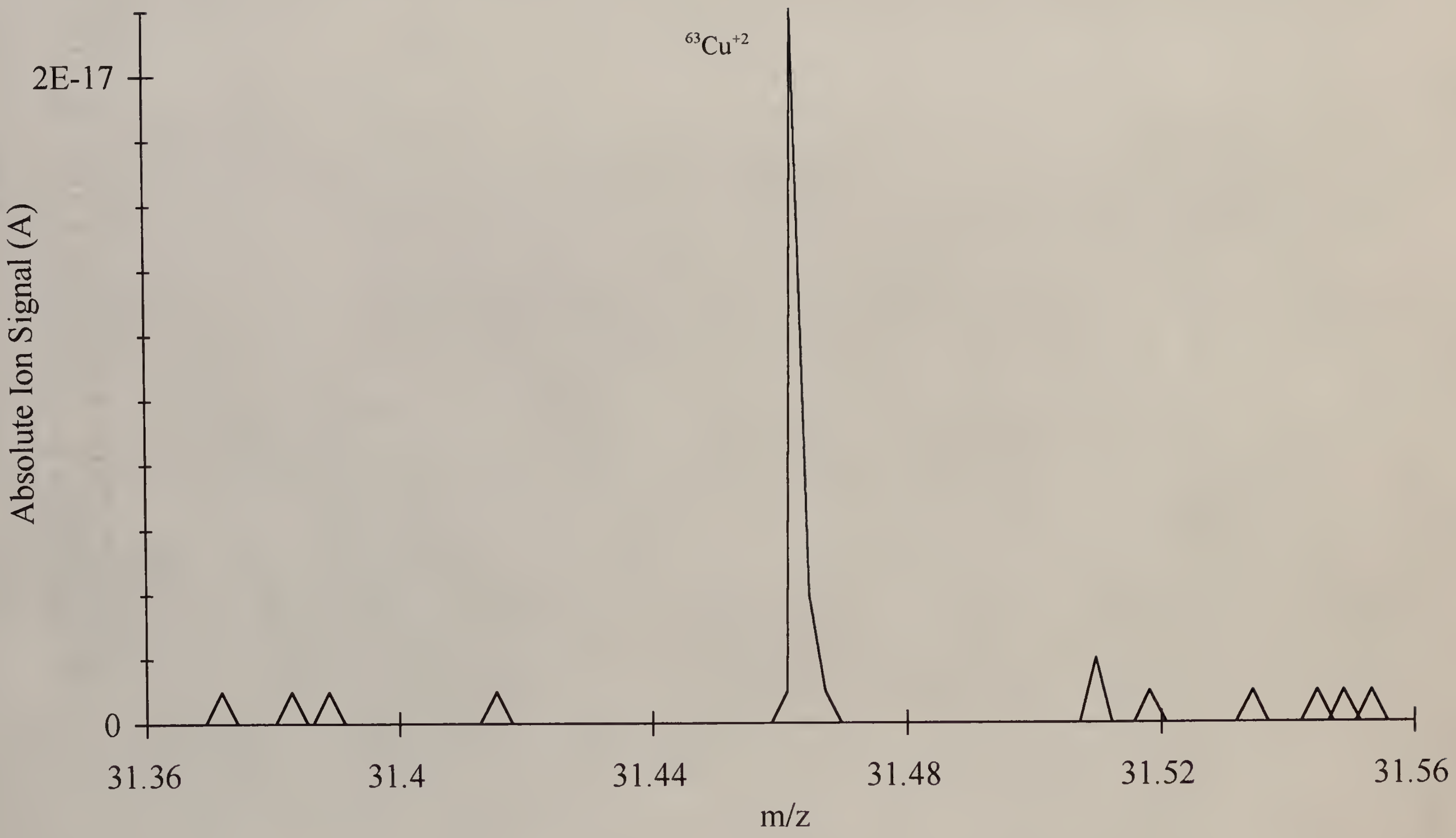
$^{63}Cu^{+2}$
2E-17
0
Absolute Ion Signal (A)
31.36
31.4
31.44
31.48
31.52
31.56
m/z

Figure 3.1: (a)

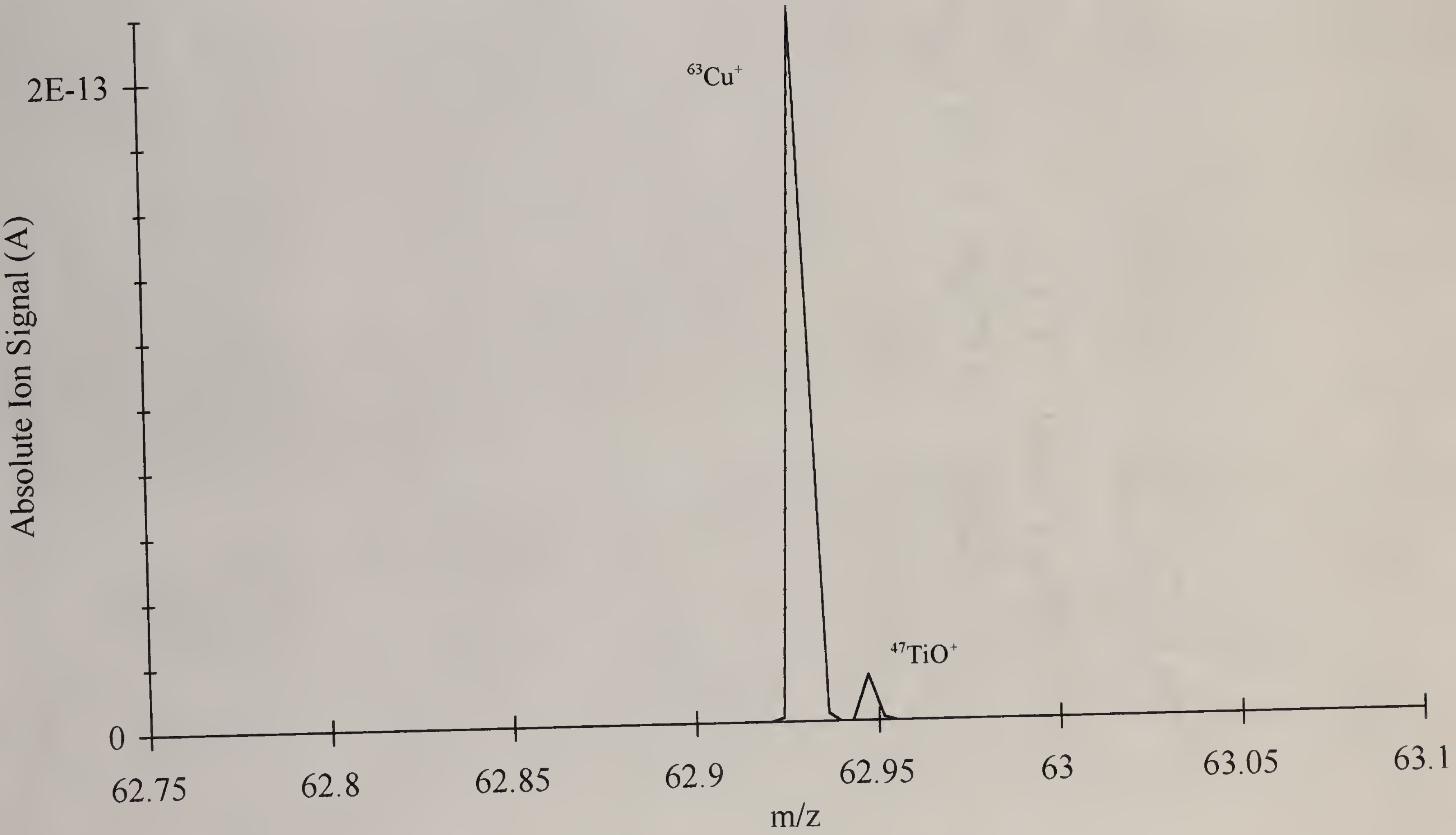

Figure 3.1:--continued. (b)

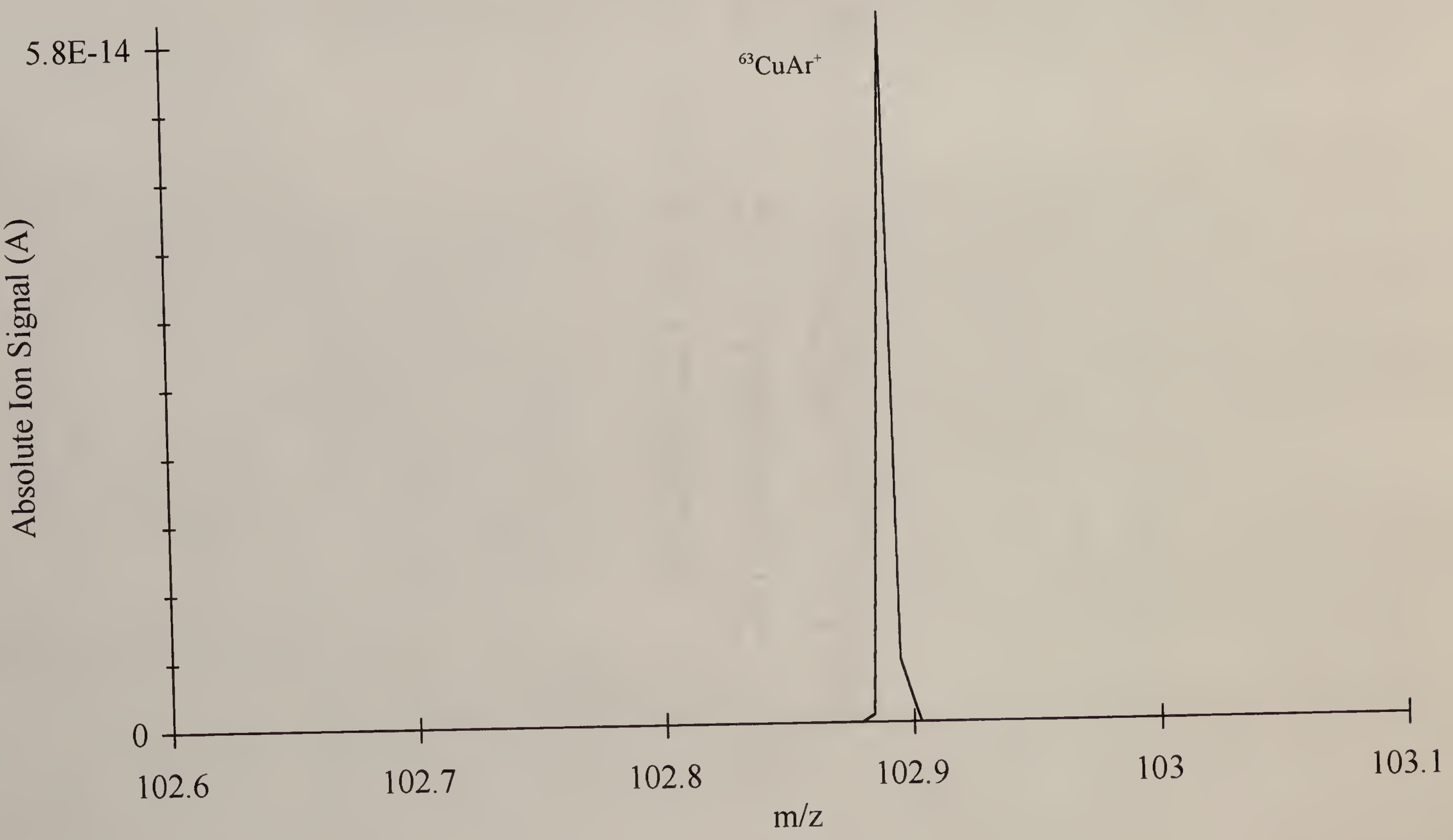

Figure 3.1:--continued. (c)

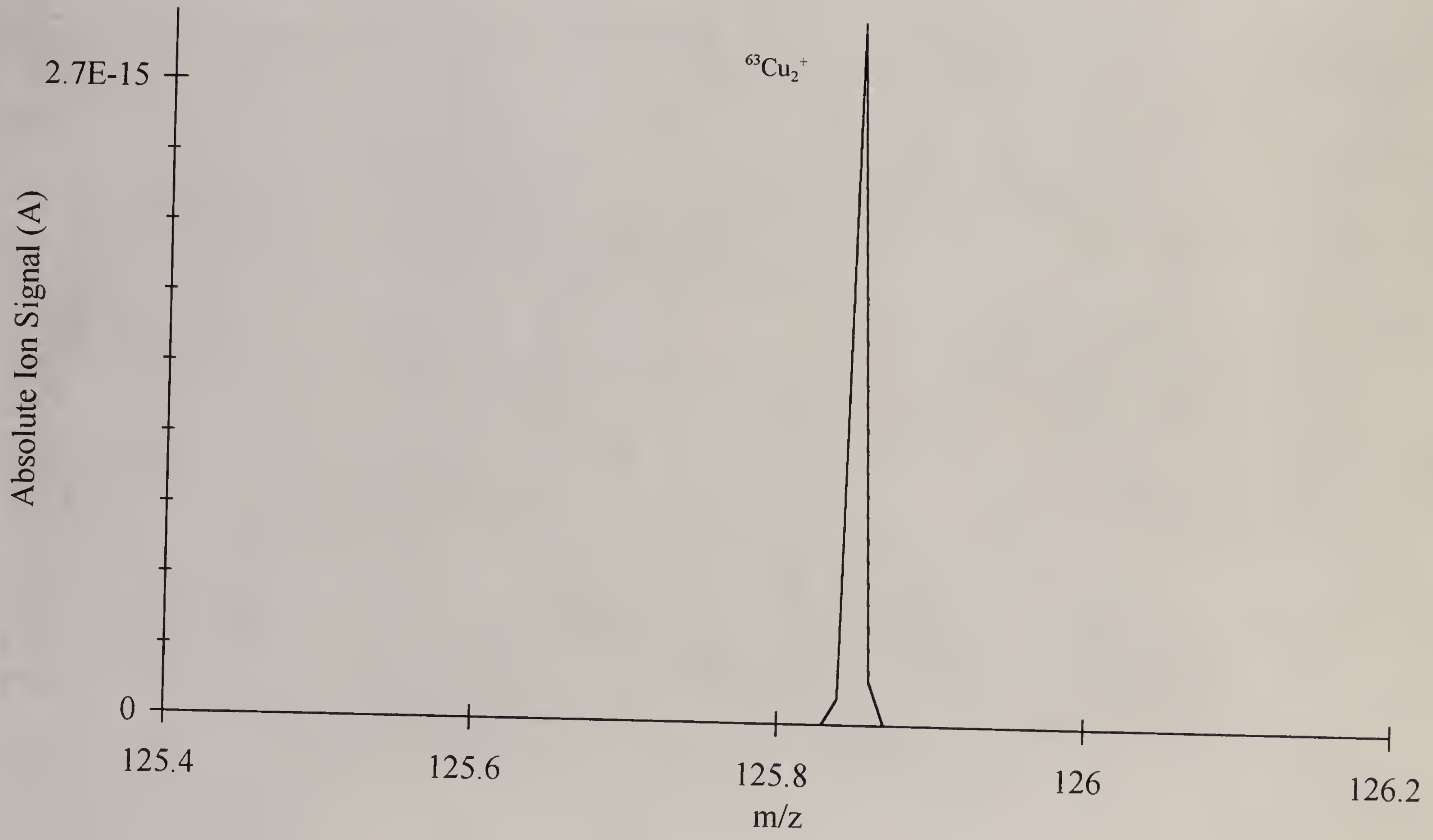

Figure 3.1:--continued. (d)

Figure 3.2: Effect of power on relative ion signals of various species found using glow discharge mass spectrometry of a NIST SRM 604 cathode, 8 mPa argon. (a) Effect of power on relative ion signal of the M^+(■), M^{+2}(●), MAr^+(×), and M_2^+(▲) species. (b) Effect of power on relative ion signal of the TiO^+( ), MgO^+( ), AlO^+( ), CuO^+(×), and O^+( ) species.

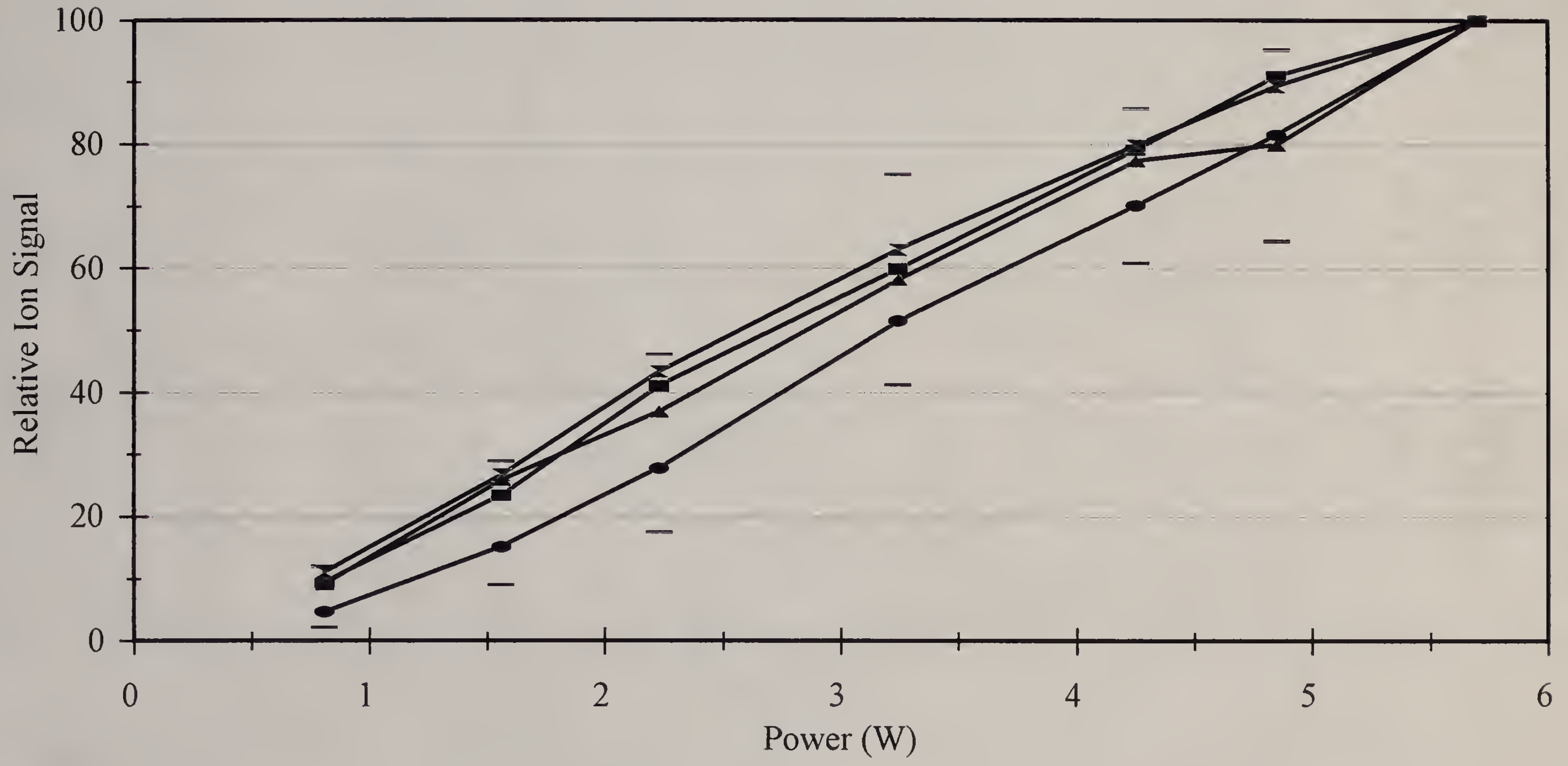

Figure 3.2a: (a)

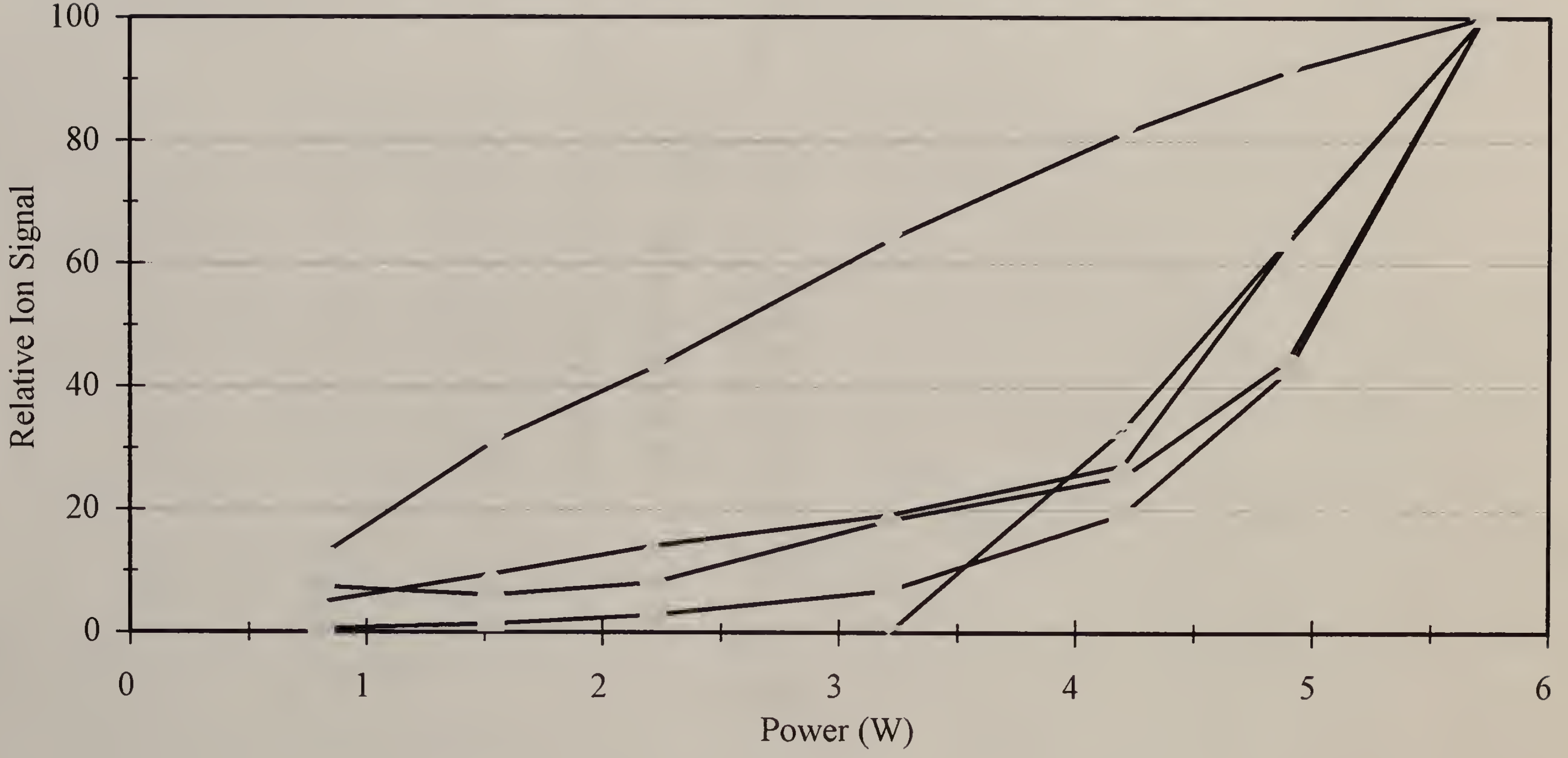

Figure 3.2--continued. (b)

Figure 3.2a shows the response of the average relative ion signal as a function of power for metal, argide, dimeric, and doubly-charged ions formed with an aluminum cathode (NIST SRM 604) containing magnesium, copper, and titanium as major components. Note that all of these species behave in a similar manner, increasing with increasing power at constant pressure. Since these species ultimately depend on the metal atom density, it seems safe to conclude that these results can be attributed to the increase in sputter atomization that accompanies the increased current (incident number of impinging ions) and voltage (incident ion energy). For subsequent studies, a power of 4 W was chosen for the GD to operate; this was a compromise between high power, which produces higher signals, and the accompanying increase in discharge temperature that can result in more thermal liberation of atoms and in extreme cases melting of the cathode.

Figure 3.2b illustrates the effect of discharge power on the magnesium, aluminum, copper, and titanium oxide ion signals. Magnesium oxide, aluminum oxide, and copper oxide all mirror the oxygen ion signal, but titanium oxide behaves differently, increasing linearly with increasing power. It is well known that titanium is among the more aggressive oxygen getters. If one assumes that an equilibrium exists between oxygen, the sputtered metal atoms, and the metal oxide ions at a given pressure and power, then, at low powers, titanium is more readily able to combine with the relatively scarce oxygen atoms (hence the higher signal). As oxygen population and power increase (around 3W), the oxygen concentration increases faster than that of titanium until there is an excess of oxygen for which the other metals can compete; the result is an increase in the relative populations of the other metal oxides. This poses a problem, of course, in using these species for analysis. If an equilibrium does exist, and if the composition of a sample were known, and if the oxide content were in equilibrium with the metal, one could operate under conditions where quantitation would be possible. However, since the oxygen levels in a glow discharge are a combination of sputtered oxides, entrained water (in the case of compacted samples), and contaminants, equilibrium would seem difficult to obtain. Thus, although abundant enough to permit their use for quantitation, metal oxide ions were not further investigated.

Figure 3.3 shows the effect of pressure on the average relative ion signal of the metal, the argide, the dimeric, and the doubly-charged ions at a constant current of 1.4 mA. The cathode was the same NIST SRM that was used in the previous study. Two different trends are observed, that of the singly-charged metal ions and that of the test species ions. It has been shown by Hess, et al. that metal ions mirror the argon metastable population [62], increasing with increasing ground-state argon population, reaching a maximum, and then finally decreasing as the pressure continues to increase and the destructive collision rate of the metastables exceeds their creation rate. This is the trend shown by M^+ (solid squares), but does not apply to the other species. A number of other differences are apparent. There is no distinct local maximum. Many of these species require stabilizing collisions for their formation [63]; at any given pressure, the probability of a stabilizing collision and dissociating collision should be constant. The observed decrease with increasing pressure can probably be attributed to the interdependence between pressure, current, and voltage in the discharge. Under constant current conditions, as pressure increases the voltage and hence the incident ion energy will decrease, decreasing the sputtering rate and the neutral atom density [62]. Since the measured test species all depend on atom density, they may respond accordingly.

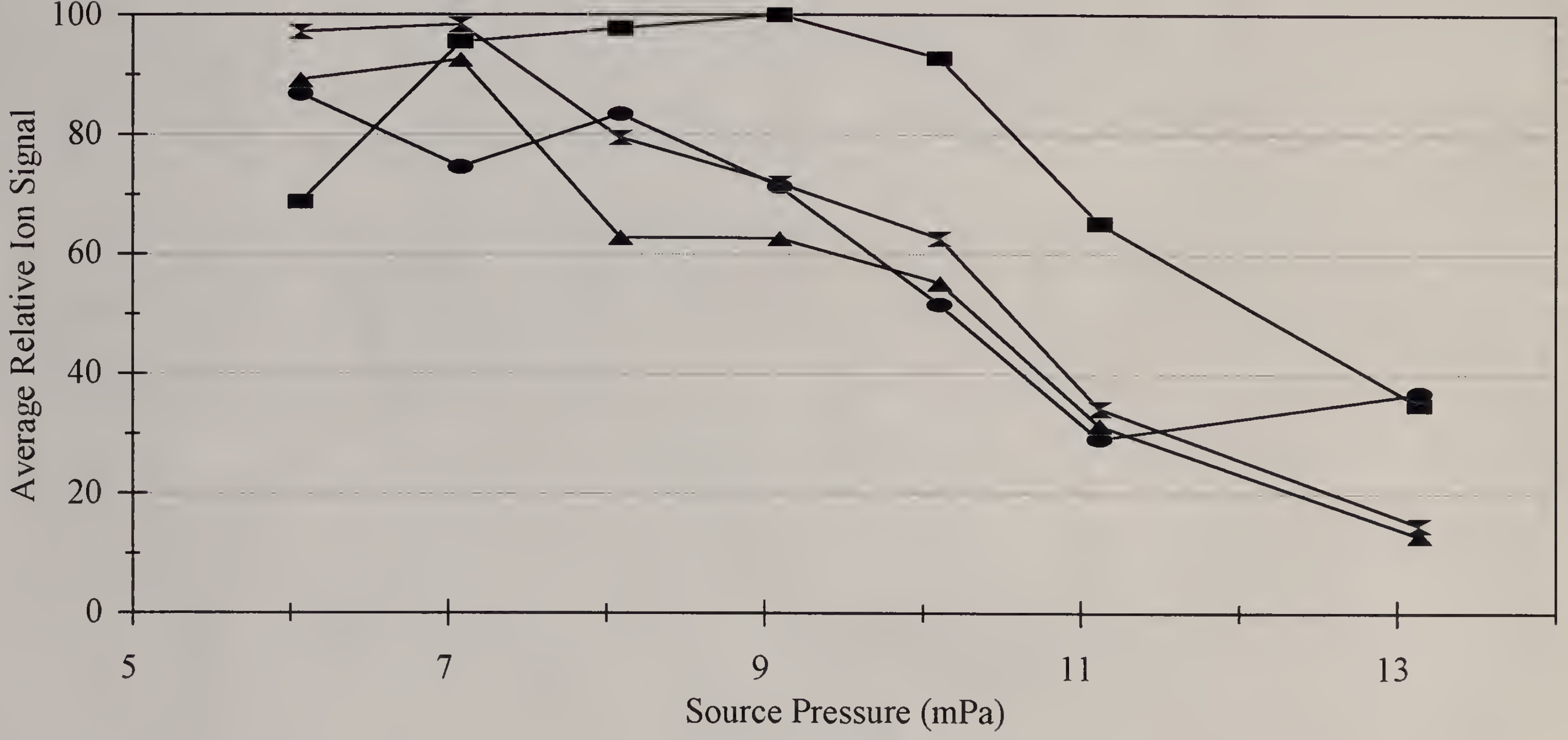

Figure 3.3: Effect of pressure on average relative ion signal of the M^+(■), M^{+2}(●), MAr^+(×), and M_2^+(▲) species. NIST SRM 604 cathode, 1.4 mA constant current.

For the remaining studies, a constant pressure of approximately 8 mPa was used; this was a compromise between a higher pressure (e.g., 9 mPa) where a higher signal was observed for the M^+ ions but a lower signal for the other species, and a lower pressure (e.g., 6 mPa) where a higher signal was observed for the argides, dimers, and doubly-charged species but a lower signal for the M^+ ions.

Reference Quantitation

To see if alternative species (i.e., metal argides, metal dimers, and doubly-charged metal ions) could be used for quantitative elemental analysis, three standard reference materials were used to provide quantitation for a fourth. NIST SRM's 601, 603, and 604 were used as reference materials to analyze SRM 602.

For the M^+ ions, relative sensitivity factors (RSF's) were calculated in the conventional manner using the following equation:

$$RSF_M = (I_r / C_r) / (I_M / C_M) \qquad (1)$$

where I_M is the ion intensity of the metal, C_M is the concentration of the metal, I_r is the ion intensity of the reference element and C_r is the concentration of the reference element. For the argides, dimers, and doubly-charged species, I_M was replace with I_{MAr}, I_{M_2}, and I_{M+2}, the intensity of the metal argide, metal dimer, and doubly-charged metal ions, respectively. In these studies, aluminum was the reference element, r. By rearranging equation (1) and using RSF's from the standards, equation (2) is obtained:

$$C'_M = (RSF_M)[(I'_M)(C_r) / (I_r)] \qquad (2)$$

where C'_M is the concentration of the metal in the unknown. Table 3.1 shows the results from this analysis. The M^+ species gave excellent accuracy (< 5% relative error, which is the measured value minus the true value divided by the true value times 100), due in part to the lack of interferences and in part to the relatively high concentrations of these elements in the sample. The average errors found using the MAr^+ and M^{+2} were on the order of 15%, except for Cu^{+2}. It is well known that in many samples the M^+ peak is interfered to the extent that the 15% error associated with using these alternative species would be superior. The problem with Cu^{+2} is attributed to its relatively high second ionization potential (20.29 eV, compared to the 15 - 16 eV for the other elements), and the poorer signal accompanying it. The errors associated with the dimers averaged ca. 40% relative error, even though the signals were 1 - 2 orders of magnitude higher than the doubly-charged species. This is probably due to interference peaks for each element that make accurate measurement of the dimers difficult for each element. For example, the manganese dimer at m/z 110 had interferences that masked the peak so badly that there was a peak even with the significantly lower manganese concentrations in SRM's 603 and 604. Interference peaks did not have an effect on the doubly-charged species since a half mass could be chosen for use, or the argides, since their signals were so much larger than either the dimers or doubly charged species.

Since all of these species are in much lower abundance than the M^+ species, their limits of detection (LOD), defined as 3 times the standard deviation of the background divided by the slope of the calibration line, are higher. For this study, the average LOD for M^+ was 60 ppb. The relatively large abundance of argides (up to 30% of the M^+species) provide the next lowest LOD, 300 ppb. The dimers and doubly-charged species gave an average LOD of 160

Table 3.1. Concentrations of several elements in an NIST aluminum standard determined from the metal ion, the doubly-charged ion, the metal argide ion, and the metal dimer ion signals.

		NIST SRM 602	M^+	M^{+2}	MAr^+	M_2^+
Magnesium	Conc. (%)	1.49	1.45	1.44	1.59	1.03
	1σ (%)	—	0.16	0.15	0.64	0.41
	% RSD		11.0	10.4	40.3	39.8
	Abs. % Error	—	2.7	3.5	6.7	31
Silicon	Conc. (%)	0.13	0.13	0.16	0.14	0.09
	1σ (%)	—	0.01	0.06	0.08	0.02
	% RSD		7.7	37.5	57.1	22.2
	Abs. % Error	—	0.0	2.3	7.7	31
Iron	Conc. (%)	0.28	0.28	—	0.22	0.13
	1σ (%)	—	0.04	—	0.05	0.03
	% RSD		14.3		22.7	23.1
	Abs. % Error	—	0.0	—	21	55
Manganese	Conc. (%)	0.63	0.60	0.67	—	0.22
	1σ (%)	—	0.07	0.07	—	0.03
	% RSD		11.7	10.4		13.6
	Abs. % Error	—	4.8	6.3	—	65
Copper	Conc. (%)	4.44	4.34	2.46	3.49	3.15
	1σ (%)	—	0.60	0.61	0.67	1.29
	% RSD		13.8	24.8	19.2	41.0
	Abs. % Error	—	2.3	45	21	29

ppm and 360 ppm, respectively. As one approaches the limit of detection, the uncertainty of the measurement, as always, increases. A point is thus reached where the error associated with using alternative species is as large or larger than that associated with the interfered M^+ peak. However, with proper care, these species can be used either for primary quantitation or for confirmation, in a manner similar to the way a second isotope of an element can be used.

Unknown Quantitation

To evaluate the usefulness of this technique, an NIST standard containing molybdenum, titanium, chromium, iron, and nickel was analyzed under conditions simulating those for analysis of an unknown. NIST SRM 644 was used to obtain RSF's for use in the analysis of an NIST 1190 standard that served as the unknown. In the spectra obtained for this 1190 standard, it was observed widely varying isotope ratios for molybdenum, suggesting that every isotope was interfered with by one or more polyatomic species. Table 3.2 illustrates a number of possible interferences that could result from the discharge gas, contaminant gases, and the major components of the sample. The resolution needed to separate these interferences from the isotope of interest ranged from 1300 to in excess of 76000 ($m / \Delta m_{1/2}$). Results showed that the concentration of molybdenum, based on the average of all the singly-charged metal isotopes, was 5.79%; this is a positive 52% relative error, confirming the presence of interfering species. Table 3.3 shows the molybdenum concentrations obtained from the ^{95}Mo and ^{96}Mo isotopes. Quantitation was based on the singly-charged metal isotopes, as well as the doubly-charged, the dimer, and the argide species associated with these isotopes (natural isotopic abundance is assumed). Using these doubly-charged and molecular species, a 15% relative error was found, compared to the 24% relative error found when the $^{95}Mo^+$ and $^{96}Mo^+$ isotopes were used. This confirms the usefulness of this approach. The smaller error (24% versus 52%) suggests that ^{95}Mo and ^{96}Mo are interfered to a lesser extent than the other molybdenum isotopes.

Several more subtle results are also noteworthy. Unlike the results obtained for aluminum, all of the measured concentrations were lower than the certified values. One explanation for this might be found in the differences in matrices between the 644 and 1190. The 644 is a titanium-based alloy, containing in excess of 90% titanium, and the 1190 contains almost equal parts titanium and molybdenum (~ 3.5%). It is not uncommon in solids mass spectrometry to have to use dissimilar matrices, but it has been known for some time that for best results matrix matching is important.

Another difference between these results and those obtained with the aluminum is that in this study the dimeric species gave the best results; this is presumably due to differences in the number of interfering species, but shows the importance of the supposition that one should not rely on any single species when absolute quantitation is the objective.

Table 3.2. Species formed from an NIST 1190 high-temperature alloy that could interfere with molybdenum.

Isotope	Interferences
$^{92}\mathrm{Mo}^{+}$	$^{56}\mathrm{Fe}^{36}\mathrm{Ar}^{+}$; $^{52}\mathrm{Cr}^{40}\mathrm{Ar}^{+}$; $^{46}\mathrm{Ti}_2^{+}$, $^{92}\mathrm{Zr}^{+}$, $^{184}\mathrm{W}^{+2}$; $^{27}\mathrm{Al}^{65}\mathrm{Cu}^{+}$; $^{60}\mathrm{Ni}^{16}\mathrm{O}_2^{+}$
$^{94}\mathrm{Mo}^{+}$	$^{54}\mathrm{Cr}^{40}\mathrm{Ar}^{+}$; $^{54}\mathrm{Fe}^{40}\mathrm{Ar}^{+}$; $^{47}\mathrm{Ti}_2^{+}$; $^{58}\mathrm{Ni}^{36}\mathrm{Ar}^{+}$; $^{46}\mathrm{Ti}^{48}\mathrm{Ti}^{+}$; $^{94}\mathrm{Zr}^{+}$
$^{95}\mathrm{Mo}^{+}$	$^{55}\mathrm{Mn}^{40}\mathrm{Ar}^{+}$, $^{59}\mathrm{Co}^{36}\mathrm{Ar}^{+}$; $^{47}\mathrm{Ti}^{48}\mathrm{Ti}^{+}$; $^{63}\mathrm{Cu}^{16}\mathrm{O}_2^{+}$; $^{46}\mathrm{Ti}^{49}\mathrm{Ti}^{+}$
$^{96}\mathrm{Mo}^{+}$	$^{56}\mathrm{Fe}^{40}\mathrm{Ar}^{+}$; $^{48}\mathrm{Ti}_2^{+}$; $^{60}\mathrm{Ni}^{36}\mathrm{Ar}^{+}$; $^{96}\mathrm{Zr}^{+}$; $^{46}\mathrm{Ti}^{50}\mathrm{Ti}^{+}$; $^{46}\mathrm{Ti}^{50}\mathrm{Cr}^{+}$; $^{47}\mathrm{Ti}^{49}\mathrm{Ti}^{+}$; $^{40}\mathrm{Ar}_2^{16}\mathrm{O}^{+}$
$^{97}\mathrm{Mo}^{+}$	$^{57}\mathrm{Fe}^{40}\mathrm{Ar}^{+}$; $^{61}\mathrm{Ni}^{36}\mathrm{Ar}^{+}$; $^{48}\mathrm{Ti}^{49}\mathrm{Ti}^{+}$; $^{65}\mathrm{Cu}^{16}\mathrm{O}_2^{+}$, $^{47}\mathrm{Ti}^{50}\mathrm{Ti}^{+}$; $^{47}\mathrm{Ti}^{50}\mathrm{Cr}^{+}$
$^{98}\mathrm{Mo}^{+}$	$^{49}\mathrm{Ti}_2^{+}$; $^{58}\mathrm{Ni}^{40}\mathrm{Ar}^{+}$; $^{62}\mathrm{Ni}^{36}\mathrm{Ar}^{+}$; $^{46}\mathrm{Ti}^{52}\mathrm{Cr}^{+}$; $^{48}\mathrm{Ti}^{50}\mathrm{Ti}^{+}$; $^{48}\mathrm{Ti}^{50}\mathrm{Cr}^{+}$
$^{100}\mathrm{Mo}^{+}$	$^{50}\mathrm{Ti}_2^{+}$; $^{60}\mathrm{Ni}^{40}\mathrm{Ar}^{+}$; $^{64}\mathrm{Ni}^{36}\mathrm{Ar}^{+}$; $^{50}\mathrm{Cr}_2^{+}$; $^{46}\mathrm{Ti}^{54}\mathrm{Cr}^{+}$; $^{46}\mathrm{Ti}^{54}\mathrm{Fe}^{+}$; $^{47}\mathrm{Ti}^{53}\mathrm{Cr}^{+}$

Table 3.3. Molybdenum concentrations determined for an NIST 1190 reference material using various species.

	^{95}Mo	^{96}Mo
NIST Certified Isotopic Concentration (%)	3.80	3.80
M^+		
Concentration (%)	4.74	4.71
Relative Error (%)	25.00	23.80
M^{+2}		
Concentration (%)	3.12	—
Relative Error (%)	17.90	—
$M^{40}Ar^+$		
Concentration (%)	3.12	3.08
Relative Error (%)	17.90	18.90
M_2^+		
Concentration (%)	3.72	3.14
Relative Error (%)	2.11	17.40

Conclusions

Metal argides, metal dimers, and doubly-charged metal ions are useful for quantitation when the analyte is obscured by interference peaks. This technique gives reasonable accuracy (ca. 15% relative error) if the elemental composition is approximately 0.1% or greater of the sample. Below this the measurement errors for the trace species are larger than for the elemental species . It is important to look at all candidate species when using alternative quantitation techniques since one or more may give false results if they also have interferences. While this technique should be used with caution, it was demonstrated that it gives the analyst a viable alternative in those cases where it is impossible to address interferences in other ways.

CHAPTER 4
INTERNAL GLOW DISCHARGE-FOURIER TRANSFORM ION CYCLOTRON RESONANCE MASS SPECTROMETRY (GD-FTICR/MS)

Introduction

Ion formation in Fourier transform ion cyclotron resonance mass spectrometry (FTICR/MS) has been extended in recent years to include virtually every type of ion source which has been used with other types of mass analyzers. These sources have included electron impact (EI), chemical ionization (CI), matrix assisted laser desorption ionization (MALDI) [64], and electrospray ionization (ESI) [65], as well as many less common ionization sources. For example, sources such as ^{252}Cf ionization [66], laser microprobe ionization [67], fast atom bombardment (FAB) [68] and continuous flow FAB [69], and secondary ion mass spectrometry (SIMS) [70] have been demonstrated. Many of these ionization sources operate at relatively high pressures, which are incompatible with those required by the high resolution FTICR detection scheme. Thus, the problem of transporting ions formed at relatively high pressure to the FTICR analyzer cell located at the center of a high field magnet (often superconducting) must be solved. This issue has been resolved in one of two ways: (1) formation of the ions outside the magnetic field and subsequent transport to the cell (over distances of 1-2 meters depending on the magnet's field strength and geometry); or (2) formation of the ions inside the high magnetic field (either directly inside or several centimeters away from the cell).

Several methods have been used to transport ions from outside the magnetic field through the fringing fields of the magnet to the analyzer cell. McIver [71, 72] employed an RF-only mode quadrupole ion guide to transport ions from an external source through the fringing magnet field to the FTICR analyzer cell. Another approach for external injection was the use of an electrostatic "wire" ion guide, where the potential difference between a rigid wire and a surrounding cylinder creates a potential well that directs ions to the trapped ion analyzer cell [73]. An alternative approach accelerates the ions through the fringing fields using a set of electrostatic lenses, followed by deceleration prior to entering the cell [74]. Of particular relevance to the work reported here are the transfer optics previously designed in this laboratory for external injection of ions created in a glow discharge probe/source [75, 76]. These transfer optics involved three acceleration/focusing lenses directly following the exit orifice of the glow discharge chamber, which allowed ions to pass through a conductance-limiting orifice in a small metal plate whose potential could be varied. Ions were then transferred ca. 1 m through a flight tube whose potential could also be adjusted, then passed through an ion decelerator assembly directly before the analyzer cell so that they could be slowed and trapped in the ICR cell.

External formation of ions with subsequent transport to the FTICR analyzer cell greatly facilitates access to the ion source for repairs, exchange with other ion sources, adjustments, and modifications. In addition, the external injection method makes it easier to employ several stages of differential pumping in order to obtain the desired FTICR cell operating pressures of less than $1\mathrm{x}10^{-8}$ torr ($1.33\mathrm{x}10^{-6}$ Pa). However, the additional intricacy of the transfer optics adds dramatically to the expense, complexity, and time required for signal optimization. A potential drawback with external injection is ion loss during transport, which can adversely affect limits of detection and lead to decreased sensitivity.

Many limitations to external injection can be overcome by forming ions in or adjacent to the analyzer region, within the high magnetic field necessary for FTICR mass detection. This is simplified if the normal ion source operates with pressures in the $1\mathrm{x}10^{-8}$ torr ($1.33\mathrm{x}10^{-6}$ Pa) range (such as a laser desorption source), but is much more complicated if the ion source operates at higher pressures (e.g. 1 torr (133 Pa) for GD sources or atmospheric pressure for ESI sources). One method has been devised which uses a source pumping arrangement consisting of a series of concentric tubes enclosing the ion source [77]. Exit orifices located at the tube ends serve as conductance limits for the pumping, allowing a pressure drop from atmospheric to the 10^{-8} torr (10^{-6} Pa) range in a distance of only 25 cm. Placement of the source within the high magnetic field eliminates the need for complicated transport and focusing optics, since ions exiting the source at large angles are focused by the magnetic field into relatively small cyclotron orbits and tend to form a beam of low divergence. Because ion formation takes place much closer to the cell than with external sources, ion transport efficiencies are higher and problems associated with ion transfer from external sources are reduced. However, the internal source approach also has disadvantages. Location of the source within the high magnetic field region makes repairs, exchange with other ion sources, adjustments, and modifications more difficult and time consuming.

We have built for use with the GD technique a concentric tube vacuum chamber similar to that described by Laude and co-workers [77-79] for electrospray ionization. The diameters of the concentric tubes were optimized for maximum conductance of the differentially pumped regions within the constraints of a 15.2 cm (6") o.d. vacuum chamber and a 1.91 cm (¾") o.d. probe.

Glow discharge ion sources coupled with FTICR/MS have received only limited interest to date [75, 76, 80-83]. The advantage of GD-FTICR/MS is the high mass resolution which virtually eliminates problems due to interferences often observed in other forms of GDMS [80, 82]. The possibility of performing RF glow discharge experiments within the magnetic field of a FTICR/MS was alluded to, but not demonstrated, in a paper by Shohet *et al.* [84]. Marcus *et al.* have reported an external RF glow discharge coupled with FTICR/MS, where externally produced ions were simply allowed to drift into the analyzer cell [80]. Barshick and Eyler developed a DC glow discharge source which used a set of electrostatic lenses to transport ions to the cell [75, 76] and this approach exhibited detection limits of 15 ppm for ^{60}Ni [76]. Other work by Watson *et al.* has shown lower limits of detection [81], but involved the use of more complicated external ion injection instrumentation.

The effect of relatively low magnetic fields on glow discharges has been studied previously [85-88]. These fields, of no more than 800 Gauss, were shown to increase ion currents in a GD/quadrupole mass spectrometer [85]. The suggested enhancement mechanism was that the magnetic field increases the electron path length, thus increasing the formation of both argon metastables and analyte ions. Other effects attributed to the presence of a magnetic field were higher sputter rates, higher currents at given voltages, and lower operating pressures [85, 86].

Using the concentric tube vacuum chamber approach, a glow discharge probe/source was successfully operate inside a high magnetic field region (*ca.* 1.5 Tesla) of the FTICR superconducting magnet and obtained similar detection limits to those previously reported from this laboratory [76] with external source operation. This paper reports the initial investigations of sputtering rates, optimization of operating parameters, and determination of limits of detection (LOD) for the high magnetic field glow discharge probe/source.

Experimental

A laboratory-built FTICR mass spectrometer (Figure 4.1) was modified with a concentric tube differential pumping arrangement (Figure 4.2) which provided three stages of differential pumping to lower pressure from 1 torr (133 Pa) in the glow discharge probe/source to 5x10^{-8} torr (6.5x10^{-6} Pa) in the FTICR analyzer cell. As shown in Figure 4.2, there are four distinct pressure regions, labeled A-D. Region A is the region of the glow discharge and is maintained at approximately 1 torr (133 Pa) of argon. Separating regions A and B is a 0.5 mm diameter conductance limit. An 800 L/s (N_2) cryopump maintains pressure in the latter region at value of 1-5x10^{-5} torr (1.3-6.5x10^{3} Pa). A magnetic shutter was employed on the conductance plate separating regions B and C. This shutter was opened to allow neutrals and ions to pass through a 4 mm orifice during ion accumulation, and then closed to facilitate better differential pumping. In region C two 300 L/s oil diffusion pumps maintained pressures of 5x10^{-6} (shutter open) and 4x10^{-7} (shutter closed) torr (6.5x10^{-4} Pa,

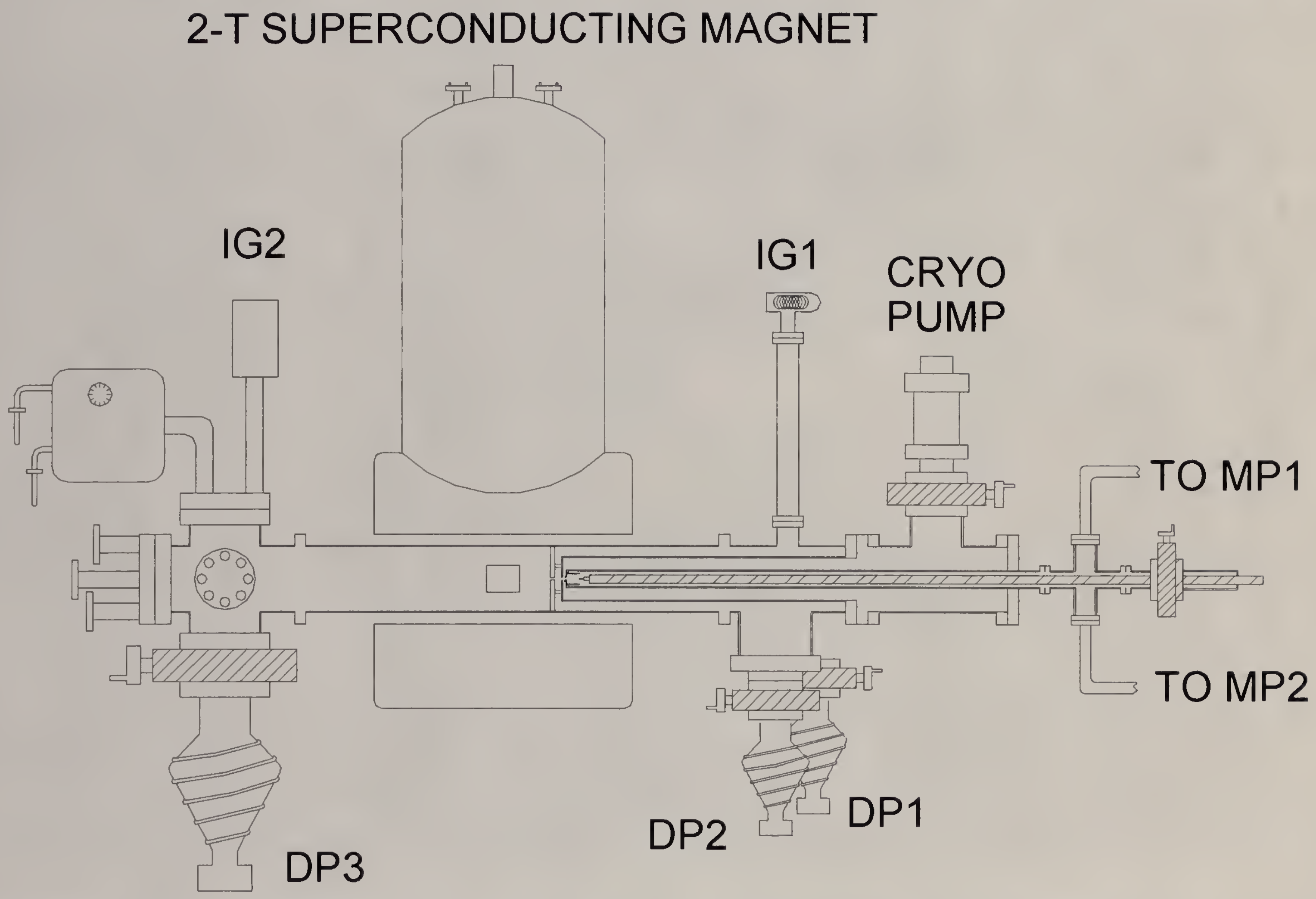

Figure 4.1: Schematic representation of the FT-ICR mass spectrometer including locations of analyzer cell, conductance limits, and internal glow discharge probe/source. (IG= ionization gauge; DP= diffusion pump; MP= mechanical pump).

Figure 4.2: Concentric tube arrangement with different pressure regimes indicated. The diagram is drawn to scale except for the conductance limits which are exaggerated for clarity. Region A is pumped by two 500 l/min mechanical pumps. Region B is pumped by an 800 l/s cryo-pump. Region C is pumped by two 300 l/s diffusion pumps. Region D is pumped by a 700 l/s diffusion pump. (1) 1.91 cm (3/4") stainless steel sample probe; (2) glow discharge sample pin; (3) removable conductance limit and Delrin® holder; (4) second conductance limit; (5) electromagnetic shutter; (6) third conductance limit; (7) ICR cell; (8) 15.2 cm (6") outer vacuum chamber.

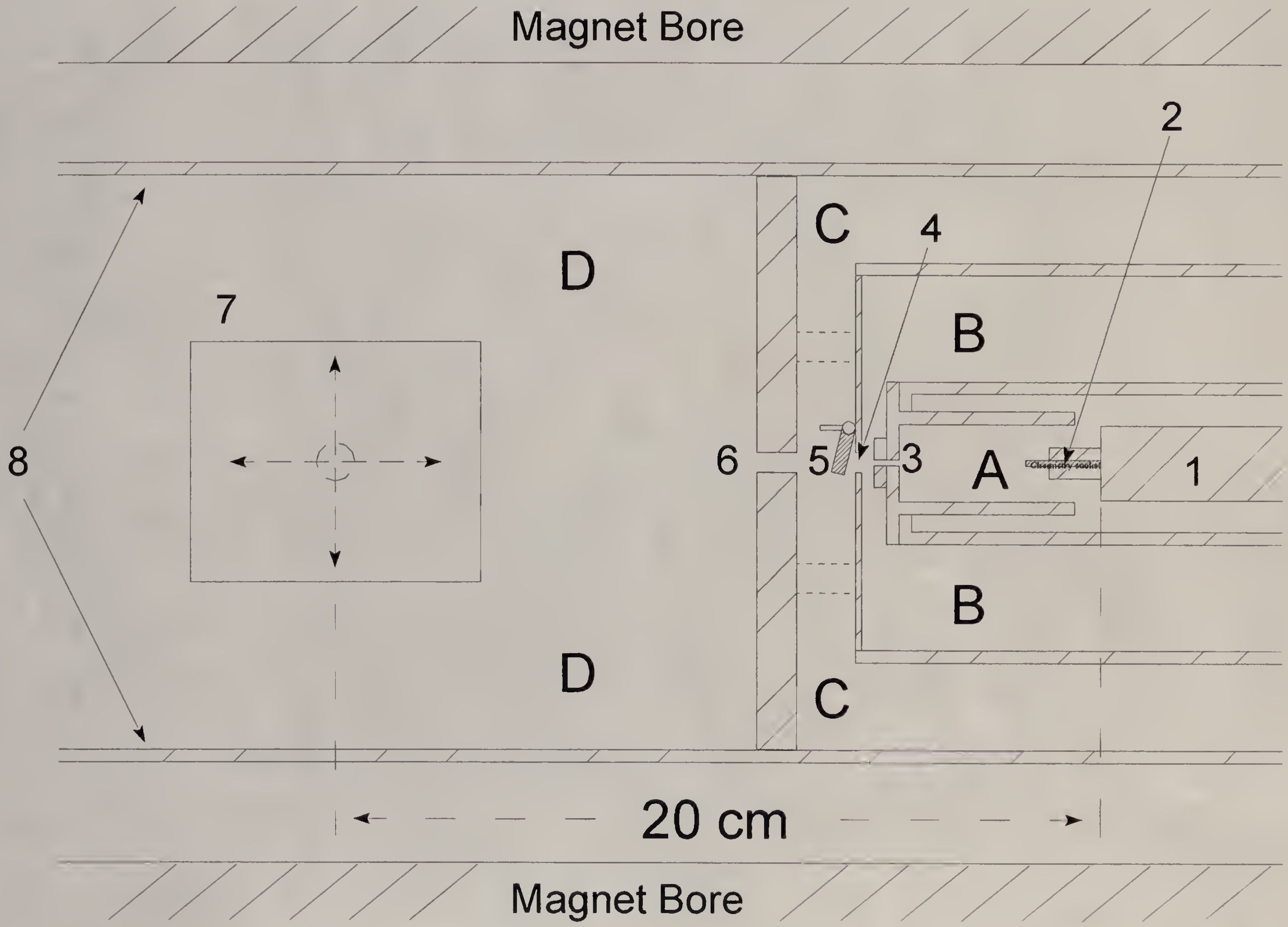
Magnet Bore
2
C
4
D
7
B
8
6
5
3
A
1
B
D
C
20 cm
Magnet Bore

Figure 4.3: Glow discharge source/probe. (A) 1.91 cm (3/4") O.D. stainless steel probe;(B) polyethylene argon delivery tube; (C) 1/8" Swagelok® union; (D) 1/8" to 1/4" adapter; (E) high voltage connector; (F) electrical feed-through; (G) sample pin holder;(H) sample pin; (I) ceramic insulator; (J) Delrin® holder; (K) Viton® O-rings;(L) stainless steel wire mesh; (M) stainless steel conductance limit holder; (N) stainless steel removable conductance limit.

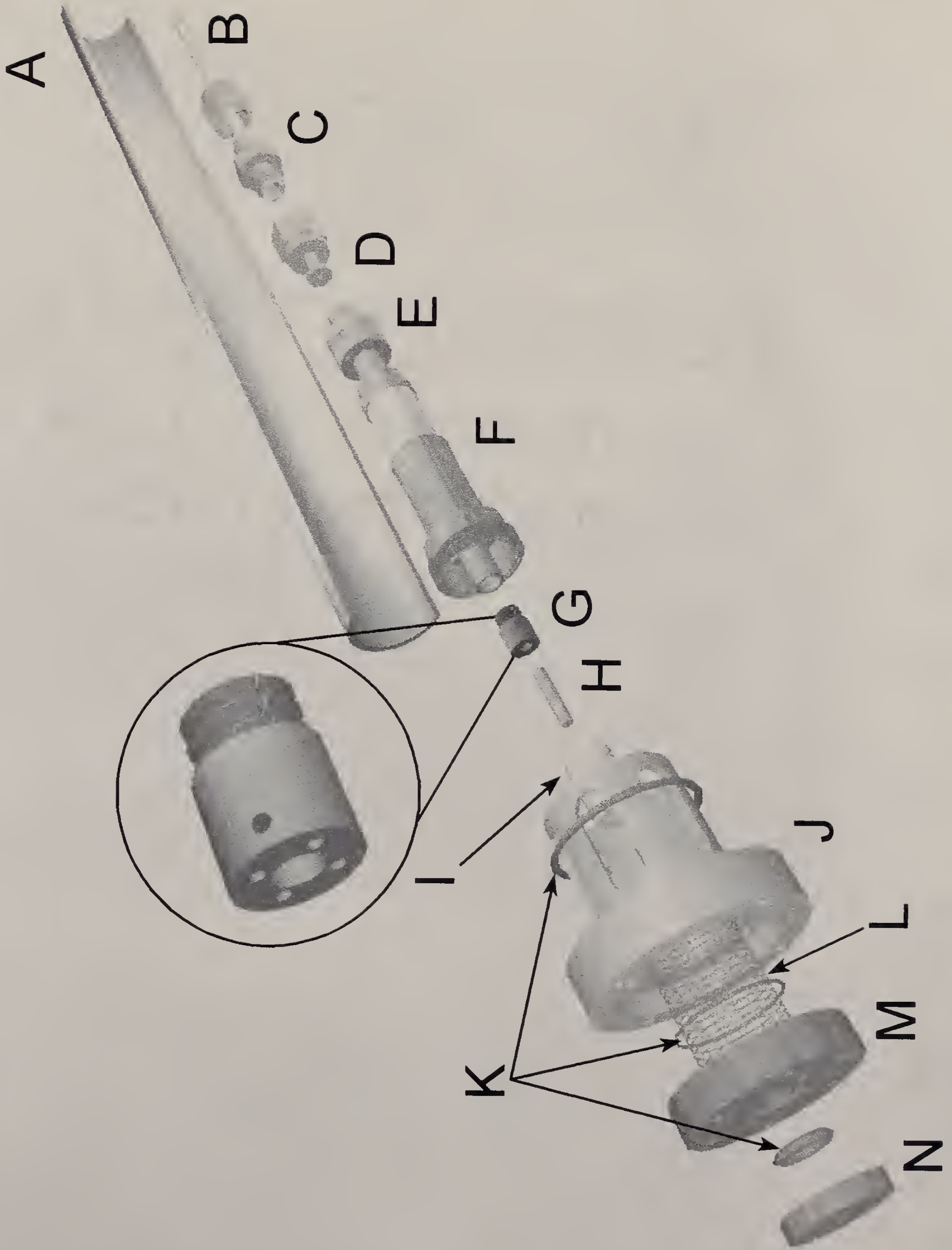
A
B
C
D
E
F
G
H
I
J
K
L
M
N

$5x10^{-5}$ Pa respectively). A second 4 mm conductance limit separated regions C and D, and a 700 L/s oil diffusion pump was used to pump the latter (analyzer cell) region. Pressures of $6x10^{-7}$ (shutter open) and $5x10^{-8}$ (shutter closed) torr ($8x10^{-5}$ Pa, $6.5x10^{-6}$ Pa respectively) were achieved.

The 1.91 cm (¾") o.d. GD probe design is shown in Figure 4.3. A high voltage feed-through (Part # FTT1213251, Kurt J. Lesker Co., Clairton, PA) with a hollow conductor was modified by welding to it a threaded stainless steel sleeve. This allowed the source assembly to be screwed into the (threaded) probe, to simplify disassembly for maintenance and alterations. The sample holder in Figure 4.3, labeled G, was also threaded so that sample holders could be accessed easily and changed to accommodate pin cathodes, hollow cathodes, or planar cathodes. A 1/4" to 1/8" copper adapter (labeled D in Figure 4.3) was brazed onto the end of the high voltage feed-through opposite the sample holder; this permitted connection of a 1/8" o.d. gas supply line. A protective ceramic cover (I in Figure 4.3) was placed over the sample to confine the glow discharge to the tip of the sample, which protruded through the cover.

For the FTICR-GDMS experiments a superconducting 2 Tesla prototype magnet (originally purchased from Nicolet FTMS) was used. Data were collected using an IonSpec data station (IonSpec, Irvine, CA). Fifty time-domain broadband transients each of 128k data points were acquired and averaged. The data were multiplied by a Hamming apodization function [89] and zero filled once prior to Fourier transformation. Industrial grade argon (99.998% pure; Bitec, Inc. Tampa, FL) was used as the discharge gas as well as the bath gas for experiments involving quadrupolar axialization [90], which utilized a laboratory-built switching box. The metal samples were small cylinders (ca. 2 mm diameter by 20 mm long) with about a 5-8 mm length of the sample exposed when it was mounted in the sample holder and covered by the ceramic cap (both shown in Figure 4.3). A National Institute of Standards and Technology (NIST) Standard Reference Material (SRM) 1261a steel sample was used for determining LODs.

Results and Discussion

Figure 4.4 shows two spectra of an NIST SRM 1261a stainless steel sample obtained with (a) the external GD probe/source [75] and (b) the internal GD probe/source which is the subject of this paper. The spectrum obtained with external injection (Fig 4.4a) shows a base peak of $^{56}Fe^+$ ($^{40}Ar^+$ was ejected before data collection) and several minor species. The spectrum obtained with internal ion formation (Fig 4.4b) shows similar peaks and has approximately the same signal to noise ratio. Several minor peaks in both spectra are due to H_2O^+, N_2^+, O_2^+, and $^{60}Ni^+$. A peak from $^{56}Fe^{16}O^+$, m/z 72, is not present in the external source spectrum, but is seen for the internal probe/source while the argon dimer, $^{40}Ar_2^+$, is seen only in the external source spectrum. It is unclear if these differences can be attributed to more than the typical variations observed in conventional GDMS resulting from gas load, purity, etc. Similarly, no definitive explanation can be given for the enhanced $^{55}Mn^+$ and $^{60}Ni^+$ signals produced by the internal probe/source, although they may result from more thermal emission if the glow discharge in that source has a somewhat higher temperature than the external source.

Figure 4.4: Mass spectra of NIST SRM 1261a steel sample using (a) an external source [12] and (b) the internal probe/source. Figure 4a is reprinted by permission of the publisher from “A Glow Discharge Ion Source with Fourier Transform Ion Cyclotron Resonance Mass Spectrometric Detection” by Barshick and Eyler, *J. Am. Soc. Mass Spectrom.*, **3**, 122-127 Copyright 1992 by Elsevier Science Inc.

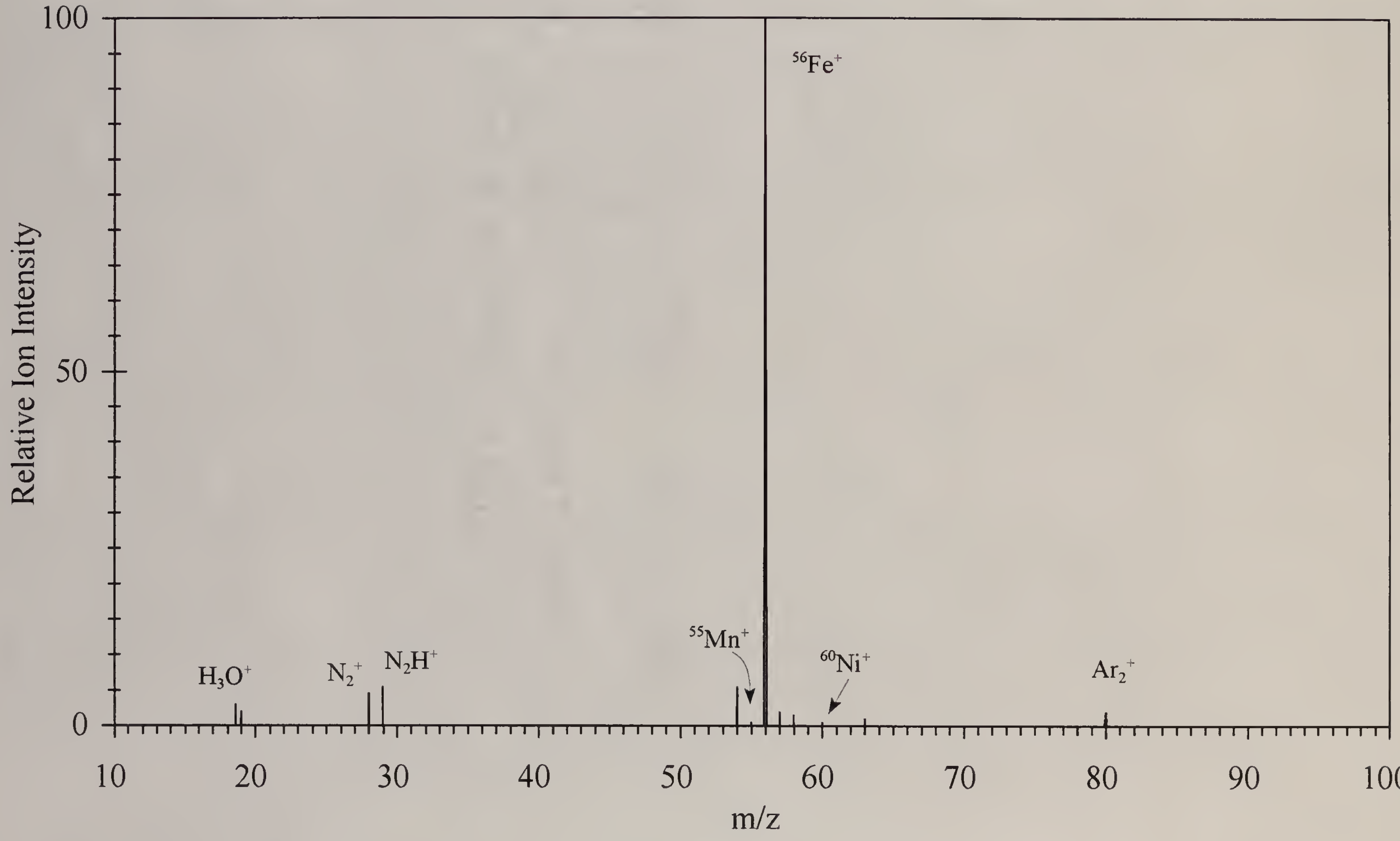
Relative Ion Intensity
100
50
0
10
20
30
40
50
60
70
80
90
100
m/z
$^{56}Fe^+$
H_3O^+
N_2^+
N_2H^+
$^{55}Mn^+$
$^{60}Ni^+$
Ar_2^+

(a)

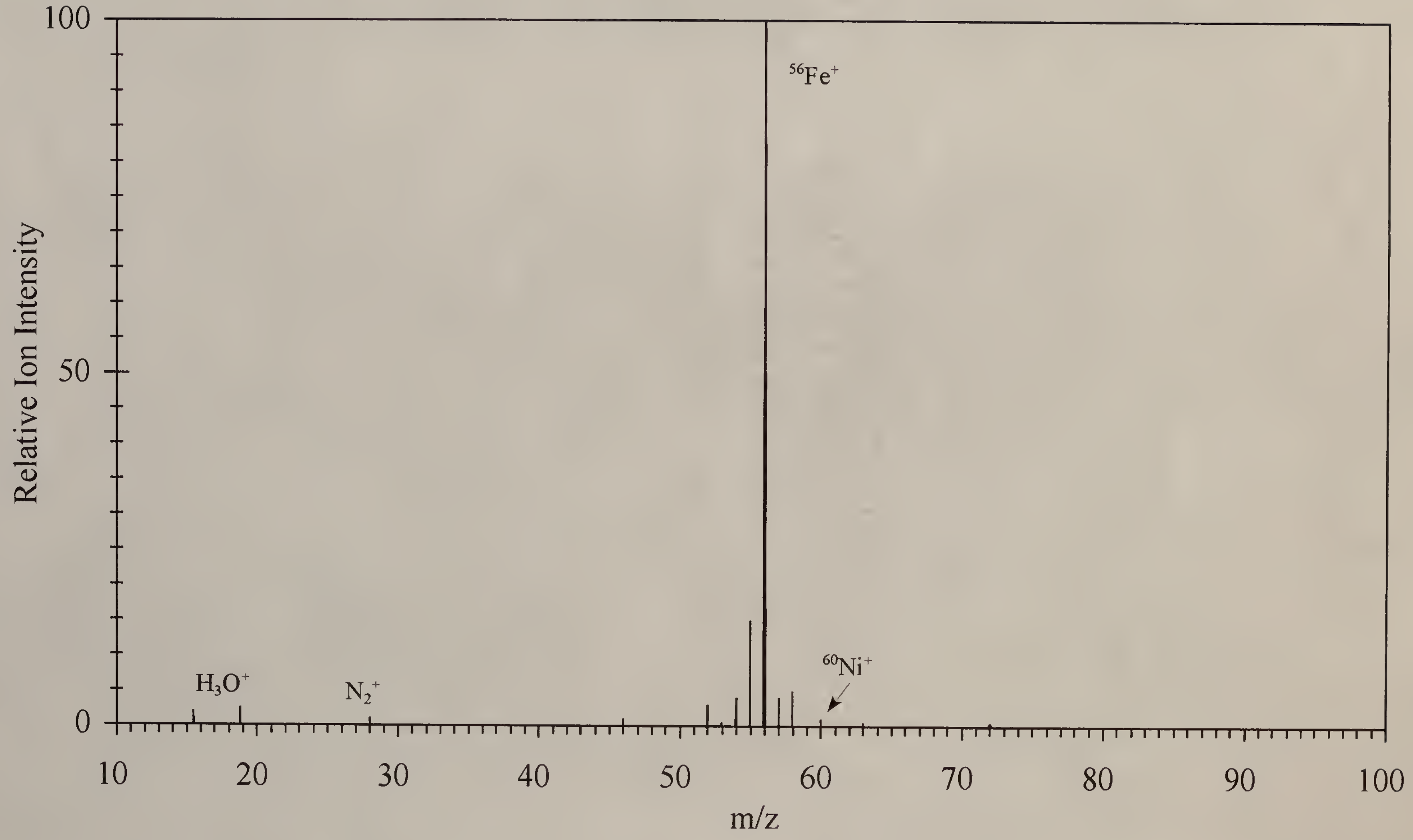

Figure 4.4:--continued. (b)

Magnetic Field

An important consideration for characterizing the glow discharge operating within a high magnetic field is the effect of the field on the discharge process. To gain insight into this, the relationship between magnetic field and glow discharge power supply voltage needed to maintain a constant discharge current was examined. This was accomplished by measuring power supply voltage as the probe/source was progressively inserted into the concentric tube assembly at various pressures. Figure 4.5 shows the results of these measurements. The data on magnetic field strength as a function of distance from the cell (left ordinate and abscissa of Figure 4.5) were reported previously by Barshick and Eyler [76].

As the probe/source was advanced progressively further into the vacuum chamber, moving toward higher magnetic field, the power supply voltage needed to maintain a constant discharge current of 0.9 mA was observed to decrease (become less negative). From approximately 100 cm to 60 cm from the center of the magnet the required voltage decreased, consistent with results reported by Bentz and Harrison [86] which showed that as an external magnetic field was increased from 200 to 500 Gauss the current for a constant voltage discharge increased. In the experiments with a constant current discharge, the voltage would decrease with increasing magnetic field, as can be seen in Figure 4.5.

Metal probe guides, located at 58 and 38 cm, caused a perturbation of discharge operating conditions as the probe passed these points. The increase in voltage beginning at about 30 cm, however, did not coincide with the presence of a guide, but did occur simultaneously with a rapid increase in the magnetic field strength. This is attributed to a

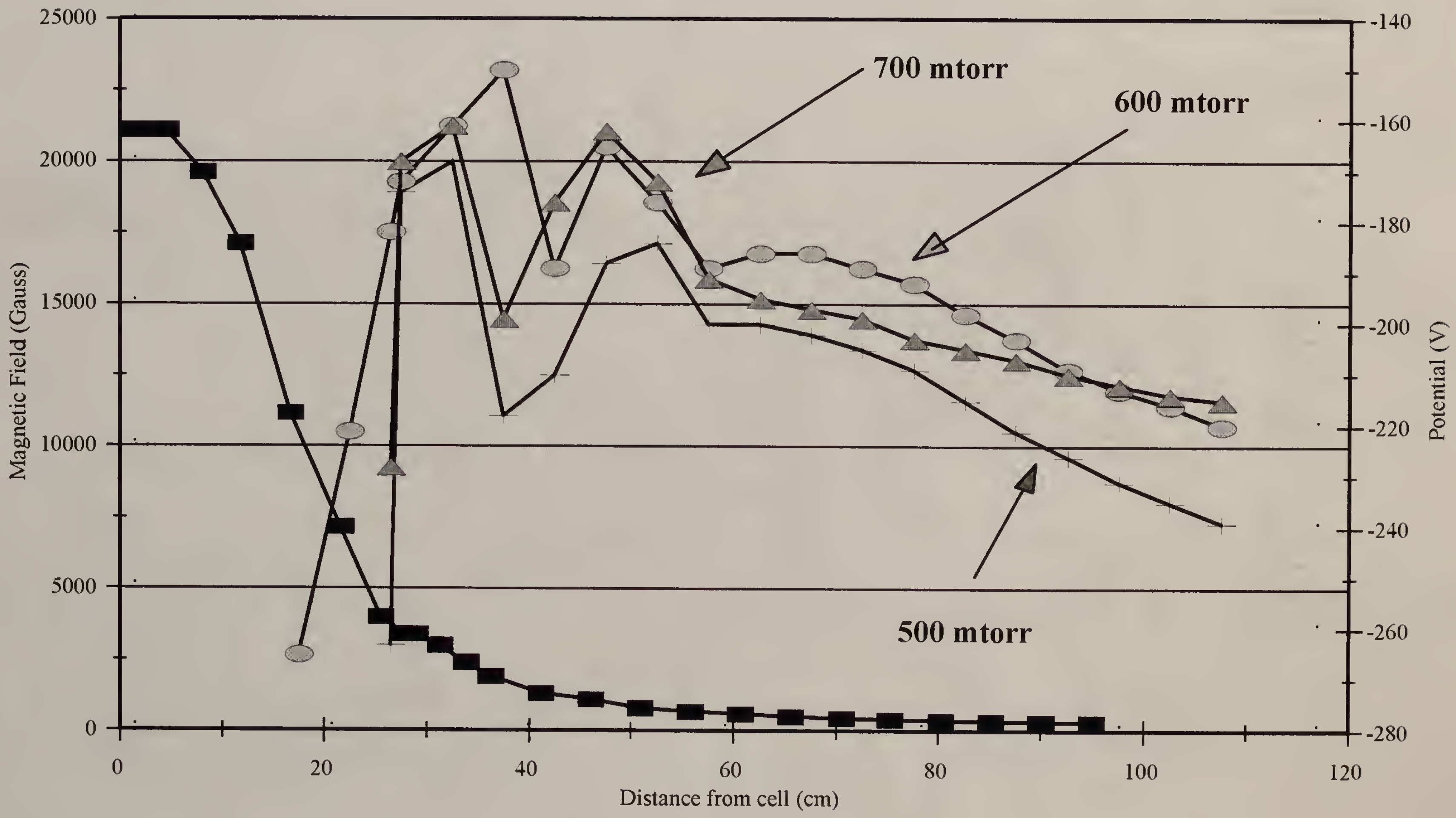

Figure 4.5: Power supply voltage necessary to maintain constant discharge current of 0.9 mA as a function of magnetic field strength at different pressures.

change in discharge voltage required for constant current to the induced cyclotron motion of the positively charged argon ions in the magnetic field, which would necessitate a higher voltage (more negative). Two possible explanations are proposed for this observation. First, argon ions undergoing cyclotron motion in the magnetic field at some distance from the sample pin will spiral down toward the sample under influence of the applied voltage. With constant voltage, the force of impact from these spiraling ions will be less than that of argon ions attracted directly to the sample in the absence of a magnetic field. Therefore, a higher voltage is needed to produce the same impact force of argon ions on the sample. Another possibility is that the cyclotron motion of the argon ions increases the path length that they must traverse before impact with the sample. This increased path length leads to a greater number of collisions, which would lower the kinetic energy of the argon ions and therefore lessen their force of impact onto the sample. Higher potentials would also be needed to overcome this effect.

Pressure, Voltage, Current Studies

Because the sample holder and discharge chamber used for these studies were different from those used by Barshick and Eyler [75, 76], it was decided to investigate the operating characteristics of the new design. It was found that the operating pressure, voltage, and current of the internal glow discharge probe/source were of the same order of magnitude as has been observed in external GD sources [91, 92]; however, the internal discharge does operate at lower pressures, voltages, and currents than the external. The discharge was found to have an onset voltage of about -330 V, with -400 V being the upper limit for stable operation at 750 mtorr (100 Pa).

It was observed that as the source pressure increased (at constant -375 V discharge potential) the ion signal also increased to a maximum at 850 mtorr (113 Pa) and then decreased. This pattern is consistent with other studies [93, 94]; the explanation given by Hess *et al.* for this phenomenon is that the metal ion signal follows the population of the argon metastable (Ar*). It has been shown that as the pressure increases at constant discharge potential there is an increase in the argon metastable (Ar*) population; above a local maximum collisional processes dominate, resulting in a decrease in Ar* and M^+ [93].

The studies reported here show that the probe/source operates similarly to a conventional GD source external to a magnetic field, but with optimal operating conditions around 0.9 mA, -375 V, and 850 mtorr (113 Pa).

Sputter Rate

Using a solid iron pin, a sputter rate of 0.25 mg/hr (n=3, σ =0.087) was determined in the high magnetic field source by sputtering the sample for two hours and measuring the mass difference before and after sputtering. Under similar conditions (voltage, current, pressure), but outside the magnetic field, a 0.23 mg/hr sputter rate (n=6, σ=0.098) was observed. By performing a two sample t-test [95] on the sputter rate data, it was determined that the two means have a greater than 95% chance of having the same true mean. This supports the belief that the lower voltage, pressure, and current needed for optimal operation of the high magnetic field GD probe/source are not dictated by the magnetic field, but instead result from probe design. This sputter rate is approximately one thirtieth that found in conventional GD sources [96] and with earlier [75, 76] external injection methods utilized by the Eyler research group. Thus, the amount of sample needed for analysis is reduced by over an order of magnitude in the probe/source designed for high magnetic field operation. A lower sputter rate would be expected to produce fewer ions, resulting in lower signals. However, signal levels comparable to external ionization were achieved. Improved ion transport in the internal design compensates for the reduced sputter rate and more of the ions formed in the discharge are eventually detected in the FTICR analyzer cell. Since the signal levels for both internal and external source operation were comparable, the internal method offers no great advantage unless the sample size is limited, where the lower sputter rate of this design would be desirable. If an ample amount sample is available, the external method is more convenient.

Limits of Detection

To evaluate limits of detection (LOD) for the high magnetic field design, a comparison was made to those obtained by Barshick and Eyler [76] on a GD-FTICR system of the same magnetic field, but with external injection of the analyte ions. Both investigations used the $^{60}Ni^+$ peak from NIST SRM 1261a. The same method for determining the limit of detection was used in each study: the LOD was determined by taking the inverse of the sensitivity (intensity per ppm) and multiplying it by 3 times the standard deviation of the mean of the background. The lowest LOD reported for external injection was 15 ppm [76]. In order to reproduce the previous work as closely as possible, a pulsed valve was utilized. The gas from the pulsed valve and the ion decelerator used in the external source studies serve the same purpose--lowering the kinetic energy of the ions to facilitate trapping. With the decelerator configuration that Barshick and Eyler used a 15 ppm detection limit of ^{60}Ni was achieved. In comparison, an 11 ppm detection limit for the same species was seen in this work (Table 4.1). Since the limits of detection were essentially the same for the external and internal injection methods and only one thirtieth the sample was used with the internal probe/source (due to lower sputter rates, *vide supra*), a 30-fold improvement in ion transport was observed. Assuming 7.5 mg/hr sputter rate for the external method, a one-minute acquisition time for 50 scans, and a LOD of 15 ppm, an absolute detection limit of 1.9 ng is determined. Assuming a 0.25 mg/hr sputter rate for the internal method, a one-minute acquisition time for 50 scans, and a LOD of 6 ppm (the best achieved for the internal probe/source design), an absolute detection limit of 25 pg is determined. This is a substantial increase over the external injection method, and is comparable to other forms of GDMS.

FTICR Advantages

There are several additional techniques in FTICR/MS that can be applied to obtain lower detection limits. These include ion ejection [97], use of pulsed valves for thermalization [98], and quadrupolar axialization [90]. Each was investigated in conjunction with use of the internal GD probe/source.

The FTICR cell can contain an upper limit of *ca.* one million ions before excessive space-charge effects distort the observed spectrum. By applying RF energy at a specific

Table 4.1. Limits of Detection (LOD) of ^{60}Ni for Various Experimental Conditions

Conditions	**LOD (ppm)**
No ejection	38
$^{56}Fe^{+}$ ejected	28
No ejection. Pulse valve on. QA off	11
No ejection. Pulse valve on. QA on	8
Eject m/z 55-57. Pulse valve on. QA on	6
External injection [76]	15

QA= Quadrupolar Axialization

cyclotron frequency, ions can be given enough energy to eject them from the cell [97]. With the ejection of ions in the mass range 55-57 amu, the relative number of nickel to iron ions increased, which resulted in a lower detection limit for nickel. For example, the LOD for ^{60}Ni improved from 38 ppm to 28 ppm when ^{56}Fe was ejected from the cell (Table 4.1).

Quadrupolar axialization (QA) is a method in which an RF waveform is applied differentially to two sets of opposing cell plates [90]. The energy imparted during the axialization process, with the help of a bath gas, collapses the ions back to the center of the cell. This allows for larger cyclotron radii to be obtained during excitation and for remeasurement of ion packets. A laboratory-built switching box currently under evaluation was used for quadrupolar axialization. In this experiment only a 27% improvement in LOD (from 11 to 8 ppm) was observed when QA was used to axialize ^{60}Ni$^+$ ion. Such a relatively minor improvement is attributed to the fact that quadrupolar axialization sees its biggest improvement with a pulsed ion source, since more signal can be obtained per pulse. Since the source was not pulsed and it is felt that incorporating a pulsed GD source should lower LOD's significantly.

Lastly, the three techniques (ejecting ^{56}Fe$^+$, using pulsed gas, and employing the Eyler research group prototype quadrupolar axialization switching box) were combined and obtained a LOD of 6 ppm. This is a 60% improvement over the result of external injection experiments. This leads to detection limits of approximately 25 picograms for the internal glow discharge probe/source taking sputtering rate and scan time into account, compared with ~1900 picograms for the external source.

Conclusions

Glow discharge sources *do* work when located inside the FTICR magnetic field and the probe/source design presented here has the added benefit of a lower sputtering rate, which enhances LODs. The relative proximity of the source to the FTICR cell results in higher ion transport efficiency when compared to previous external injection methods [75, 76]. The thirty fold improvement in ion transport seen in this work gives limits of detection comparable to external injection (low ppm), but with significantly lower sample consumption, leading to a limit of detection of 25 picograms for ^{60}Ni. Finally, it has been shown that the behavior of a glow discharge with this probe/source design in a magnetic field of approximately 1.5 Tesla is comparable to that when no magnetic field is present.

CHAPTER 5
QUANTITATION OF ION ABUNDANCES IN FOURIER TRANSFORM ION CYCLOTRON RESONANCE MASS SPECTROMETRY (FTICR-MS)

Introduction

The technique of Fourier transform ion cyclotron resonance mass spectrometry (FTICR-MS) has been used quite successfully for qualitative analytical analysis in studies such as structure elucidation [99, 100], fragmentation pathways [101, 102], reaction mechanisms [103, 104], exact mass measurements [105, 106], and glow discharge [this work, chapter 4]. However, *quantitative* analysis using FTICR has received considerably less attention. In order to improve quantitative aspects of FTICR-MS mass analysis several different methodologies have been investigated in the work reported here for manipulating the time domain FTICR transient response signals and the resulting the frequency domain spectra to obtain accurate peak intensities and ion abundances.

Accurate and precise determination of both relative and absolute ion abundances in FTICR-MS is critical for obtaining the highest quality data in many areas. An obvious need for quantitative information is the determination of unknown concentrations using appropriate calibration curves. In addition, other experiments also require precise and accurate peak intensity measurements. For example, researchers who use FTICR-MS to determine ion/neutral binding energies [107] find that the accuracy of these measurements depends directly on the quality of the ion abundance measurements. Reaction rate constants and equilibrium constants are also affected by the uncertainty in measured peak intensities. It is thus imperative that the methodology used for FTICR-MS ion abundance determinations be optimized for both maximum accuracy and precision with a minimal increase in data analysis time.

Various researchers have examined many variables involved in analyzing signals obtained in FTICR-MS [108-119], with a primary goal of obtaining the highest possible mass accuracy. Their investigations included evaluating apodization functions [108-114], zero filling [115], and various interpolation functions [116-119] which give more accurate assessment of the exact frequency (and thus mass) of peak maxima. These improvements are very important for qualitative analyses, but for quantitative analyses, one often knows the mass of the species of interest, and desires instead information on the relative or absolute ion abundance.

Liang and Marshall have reported a method for determining precise relative ion abundances using a least-squares fit of a peak to a Lorentzian lineshape [116]. The results shown are impressive, but with two major disadvantages. The peaks that are fitted in the paper are unapodized and the method is stated to be most appropriate when there is no peak overlap. However, apodization is very commonly used in FTICR mass spectrometry to enhance spectra by minimizing the sidelobes of peaks, and in order to observe small peaks that are lost in the "ringing" from adjacent larger peaks. Since many applications might be expected to require quantitation of closely spaced peaks which could overlap in the absence of apodization, the limitation of the Liang and Marshall technique to isolated peaks is a severe one.

This report builds upon previous studies which primarily focused on accurate determination of the exact frequency of a peak, and applies similar methodologies to determining accurate peak intensities. Several methods of determining both peak height and peak area have been examined. The results of applying these methods are evaluated using various simulated data sets of different size, signal-to-noise ratio, and damping constant.

Methodology

Exact knowledge of "true" peak intensities is necessary in order to make comparisons between methods which attempt to determine them accurately. For this reason it was decided to base these studies on the analysis of *simulated* FTICR ion transient responses. Such transient response signals were generated by adding a series of cosine functions whose frequencies correspond to the ion masses of interest with appropriate amplitude factors to achieve the desired abundances. Eight ion masses were chosen for the simulated signals. The cyclotron frequencies of both singly-charged lead ions (Pb^{+}) at m/z 204, 206, 207, and 208, and the corresponding doubly-charged lead ions (Pb^{+2}) at m/z 102, 103, 103.5, and 104 were used. Cosine signals at the eight different frequencies were added with the relative amplitudes of 1.4, 24.1, 22.1, and 52.4 for m/z 204, 206, 207, and 208 (as well as for m/z 102, 103, 103.5, and 104), respectively, to mimic the naturally occurring abundances of these isotopes [120]. Transient response signals were generated for four data set sizes: 16k, 32k, 64k, and 128k data points.

Transient response signals with three different noise levels were generated by adding a scaled series of random numbers to each transient. These noise levels were generated by adding random numbers in the ranges -15 to 15, -1.5 to 1.5, and 0. Figure 5.1 illustrates the effect of these three noise levels on the mass spectra of the Fourier transformed data. The left spectrum (Figure 5.1a), corresponding to addition of random numbers between -15 and +15 to each point of the transient response signal, is labeled "single-scan" because it might represent a signal-to-noise ratio typical of that seen in spectra where only one transient is collected before Fourier transformation. The middle spectrum (Figure 5.1b), with addition of a random number from -1.5 to +1.5 to each point of the transient before transformation, is labeled as "100 scans" because its noise level is 1/10th of that in the left spectrum (if the left spectrum is representative of one scan then 100 transient response signals averaged together would decrease the noise level by a factor of 10 [121]). The right spectrum (Figure 5.1c) is labeled "∞ scans" because no noise has been added to the transient response signal, corresponding to what would be seen if an infinite number of scans were averaged together before transformation. These three noise levels were chosen to represent worst case, normal, and best case scenarios. Because of the high noise level in the "single scan" spectrum, the smallest peak (1.4% for m/z 102 and 204) was not used for quantitation as it was generally not discernible from the noise.

The effect of signal damping (due primarily to ion/neutral collisions in real FTICR experiments) was also investigated by generating two sets of transients, one set undamped and one set damped. The transient response signals were multiplied by an exponential function of the form

Figure 5.1: Examples of the three types of simulated spectra used in this study using a 32k data size, 3-term Blackman-Harris apodization, and no orders of zero filling. The examples show a high noise spectrum (a), moderate noise spectrum (b), and a spectrum without any noise (c).

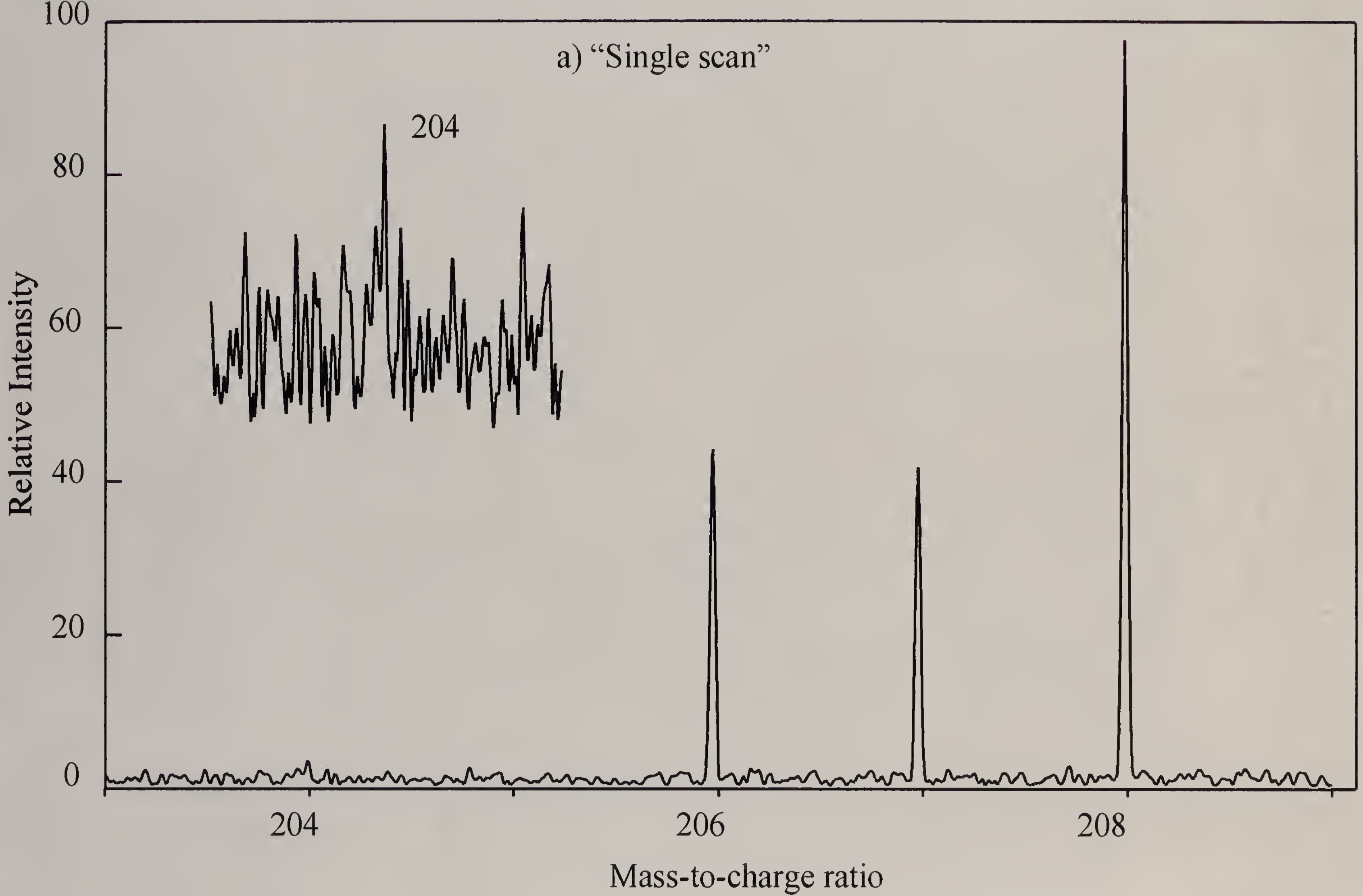

Figure 5.1--continued

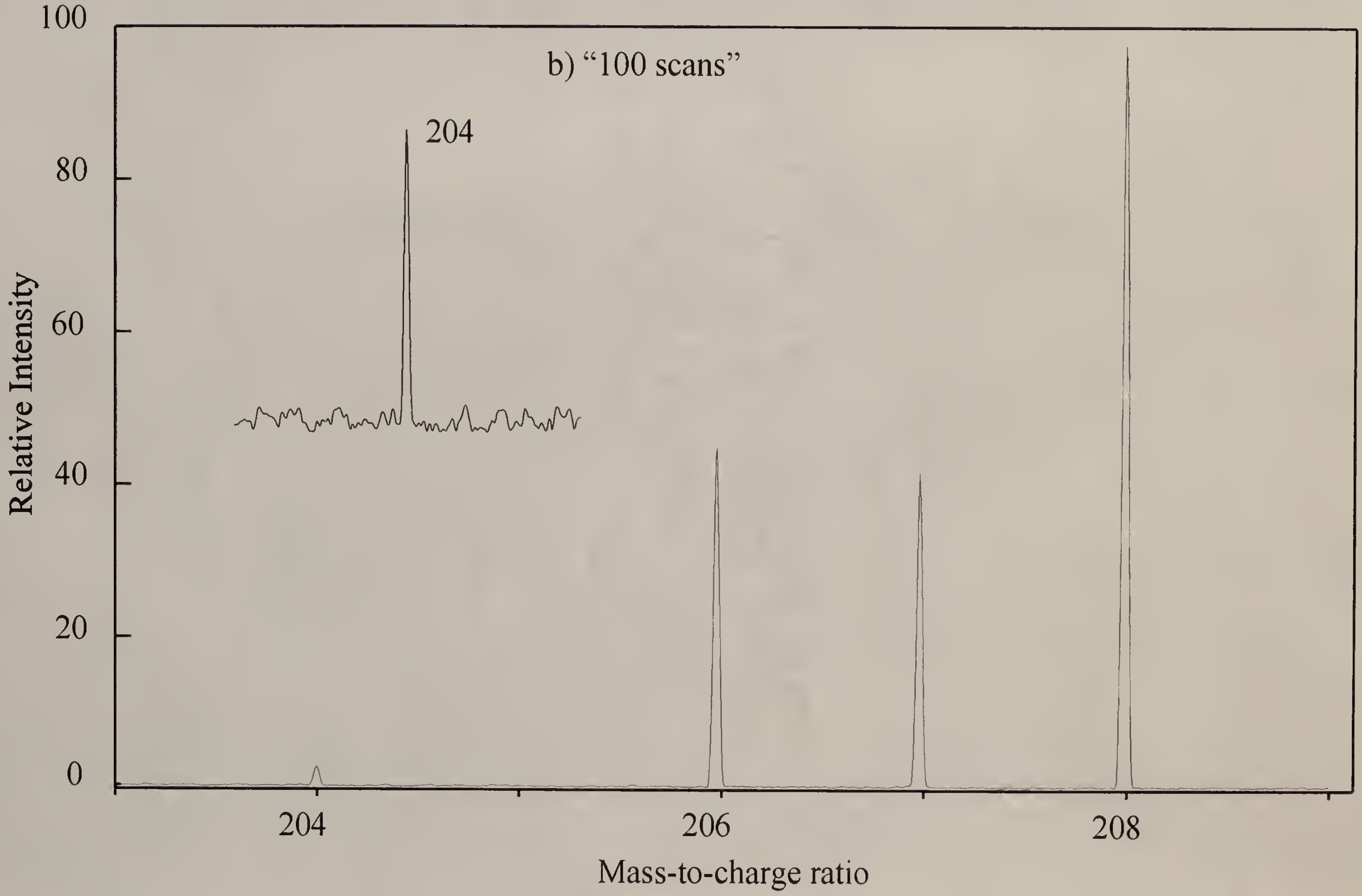

Figure 5.1--continued

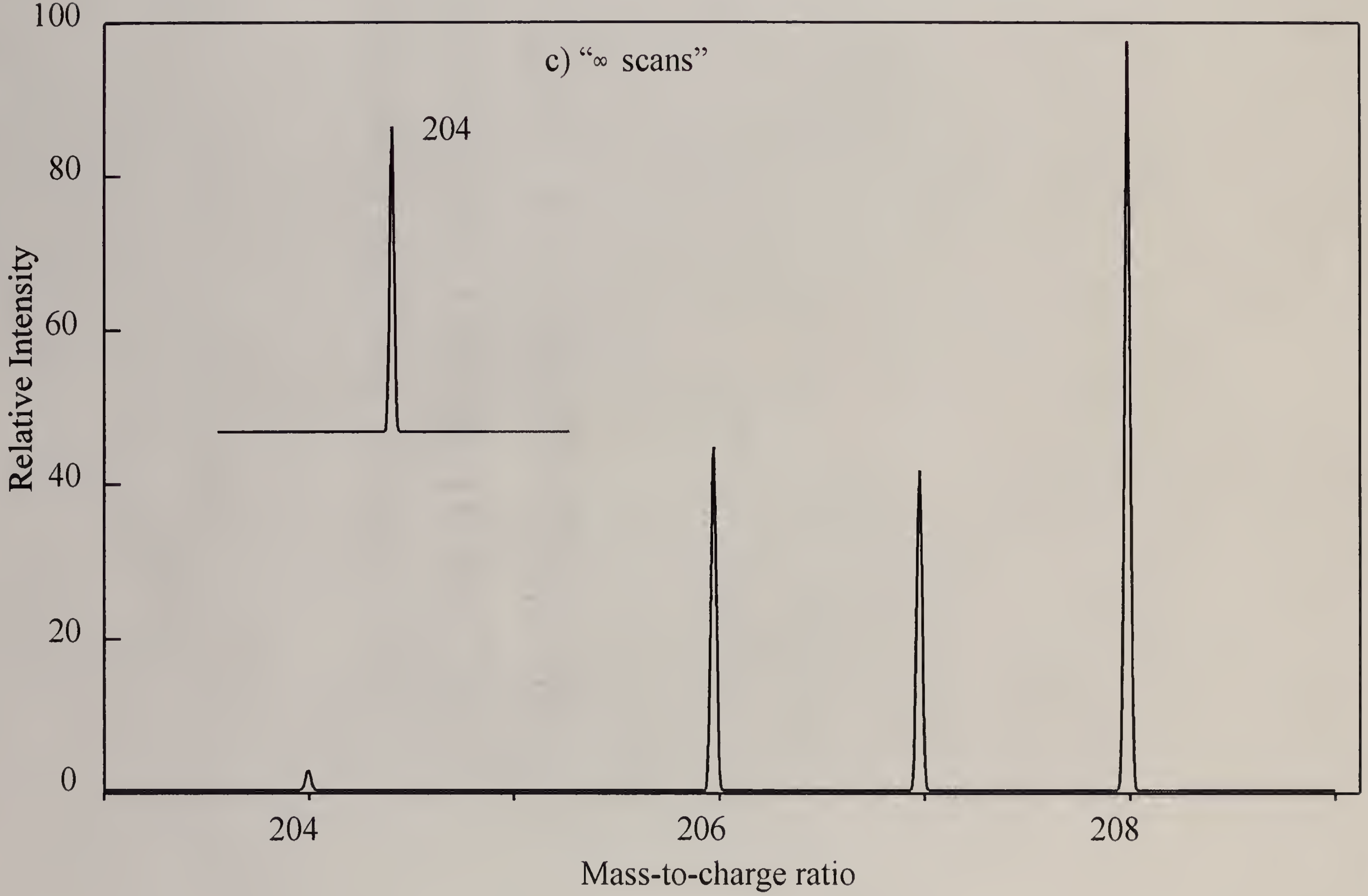

Figure 5.1--continued

$$e^{\left(-\frac{i}{2^{15}}\right)}, \quad 1 \le i \le T \tag{1}$$

where *I* is the data index number and T is the total number of data points. A value of 2^{15} was used for the relaxation constant, τ, which resulted in reduction of the final transient response data point by a factor of $1/e^{0.5}$, $1/e$, $1/e^2$, and $1/e^4$ for the 16k, 32k, 64k, and 128k data sets, respectively. The combination of 4 data set sizes with 3 noise levels and 2 types of signal damping gave 24 simulated transient response signals.

Once the representative transient response signals were generated, the effect of applying various apodization functions was investigated. Apodization involves multiplying the time domain transient by a function in order to minimized side lobes or “ringing” which appear in the frequency domain after Fourier transformation [122]. Such side lobes arise due to the Gibbs phenomenon [123] when discontinuities associated with the beginning and ending of data acquisition are present in the time domain signal. Apodization functions minimize this problem by forcing the beginning and ending portions of the transient response signal to approach zero monotonically [118].

Several of the most commonly applied FTICR apodization functions were used in this study, including Hamming, Hanning, 3-term Blackman-Harris, and the Kaiser-Bessel functions. These functions have varying characteristics, which have been studied previously [108-113]. The optimal function for a particular application depends on the dynamic range of the peaks of interest [108, 109]. The Hamming or Hanning is recommended for 1:10, the 3-term Blackman-Harris for 1:100, and the Kaiser-Bessel for 1:1000. The individual

Table 5.1: Apodization functions

Apodization Name	Analytical form, $0<t<T$
3-term Blackman-Harris	$0.42323 - 0.49755\cos(2\pi t/T) + 0.07922\cos(4\pi t/T)$
Kaiser-Bessel	$I_o[3.5\pi\{1.0 - ((2t-T)/T)^2\}^{0.5}] / I_o[3.5\pi]$
Hamming	$0.54 - 0.46\cos(2\pi t/T)$
Hanning	$\sin^2(\pi t/T)$

I_o is the zero order modified Bessel function

Figure 5.2: Graphical examples of the four types of apodization functions utilized in this study. (a) 3-term Blackman-Harris, (b) Kaiser-Bessel, (c) Hamming, and (d) Hanning functions are shown corresponding to the functions shown in Table 5.1.

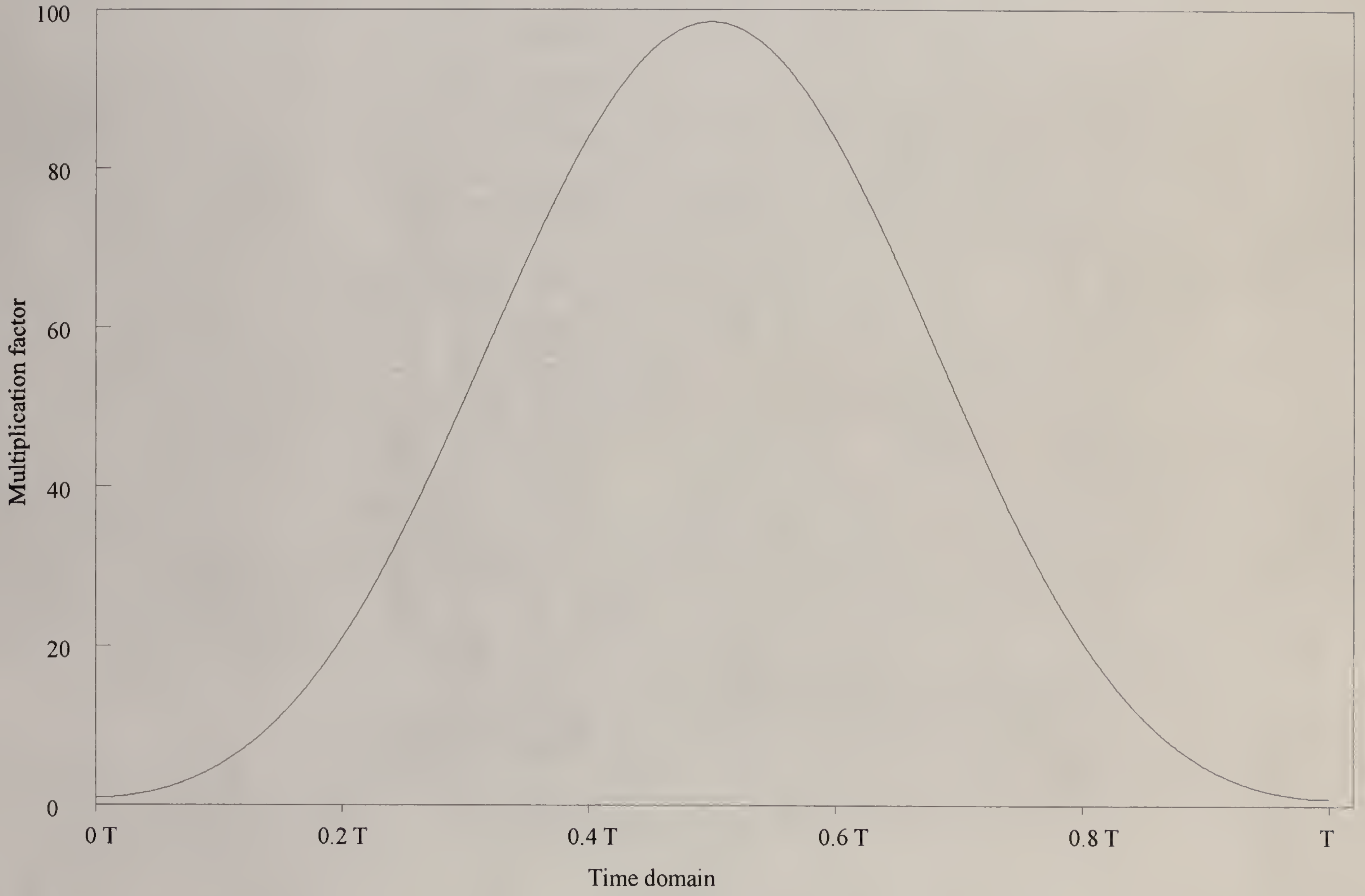

Figure 5.2--continued. (a) 3-T Blackman-Harris apodization

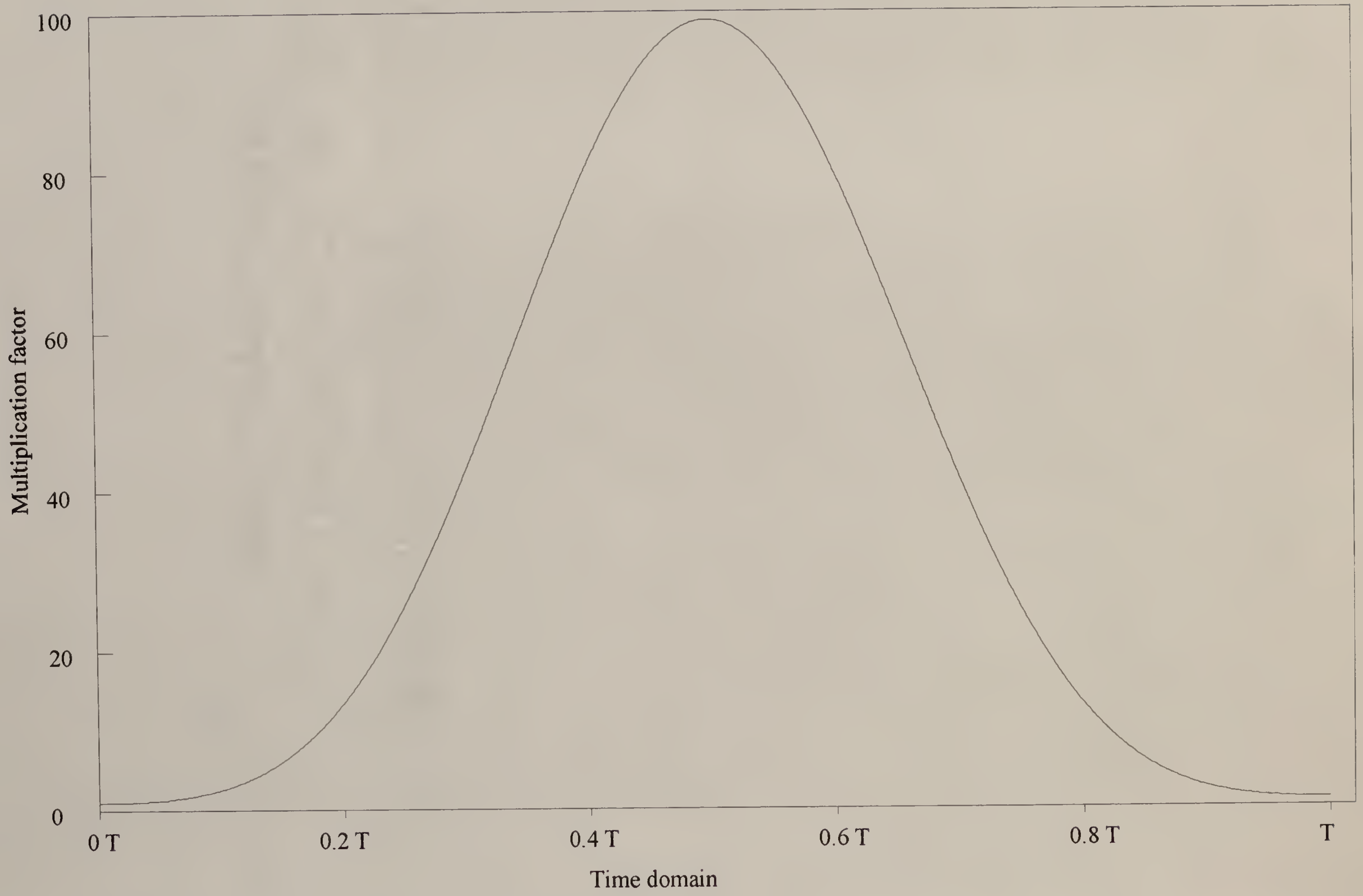

Figure 5.2--continued. (b) Kaiser-Bessel apodization

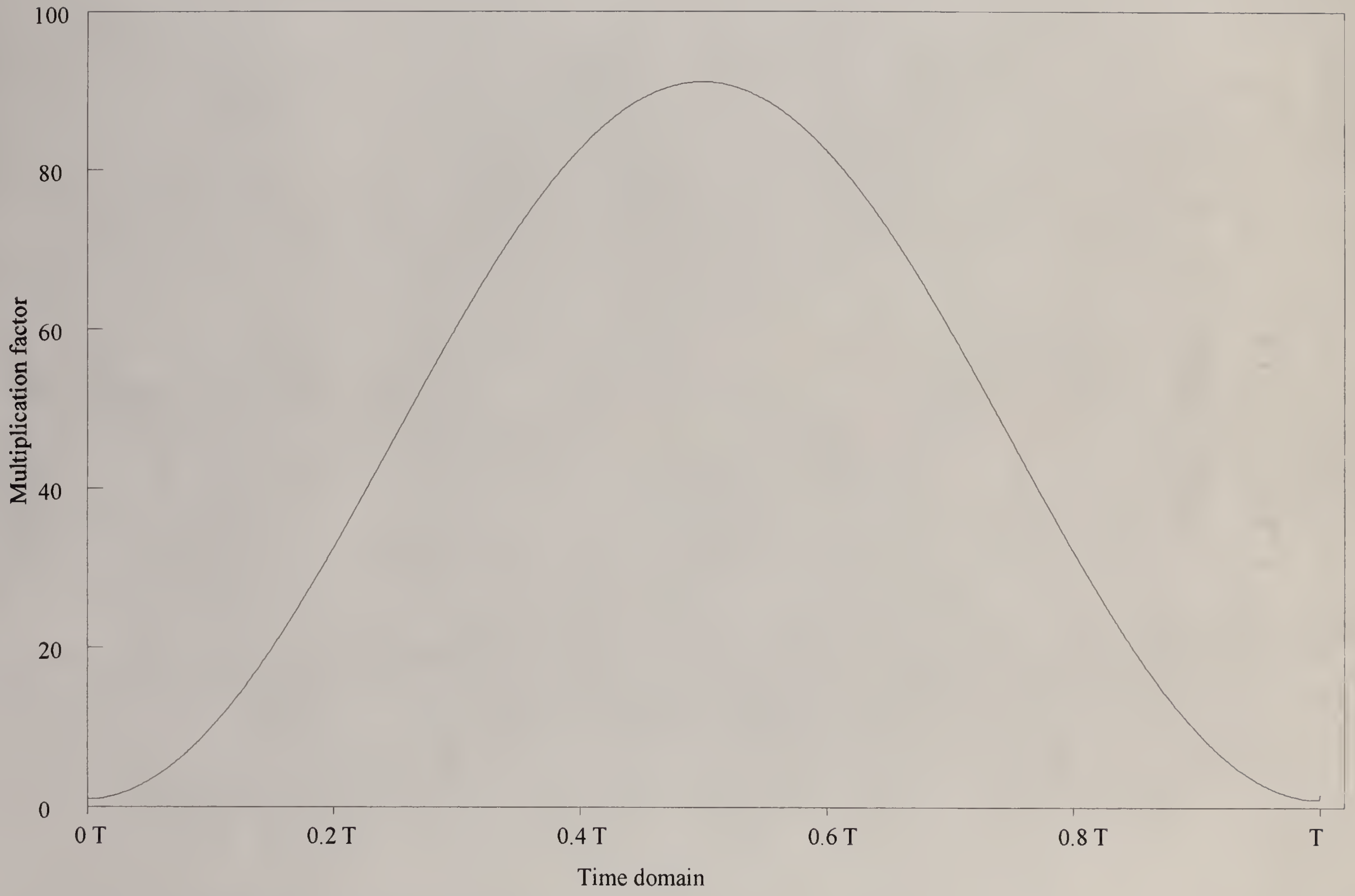

Figure 5.2--continued. (c) Hamming apodization

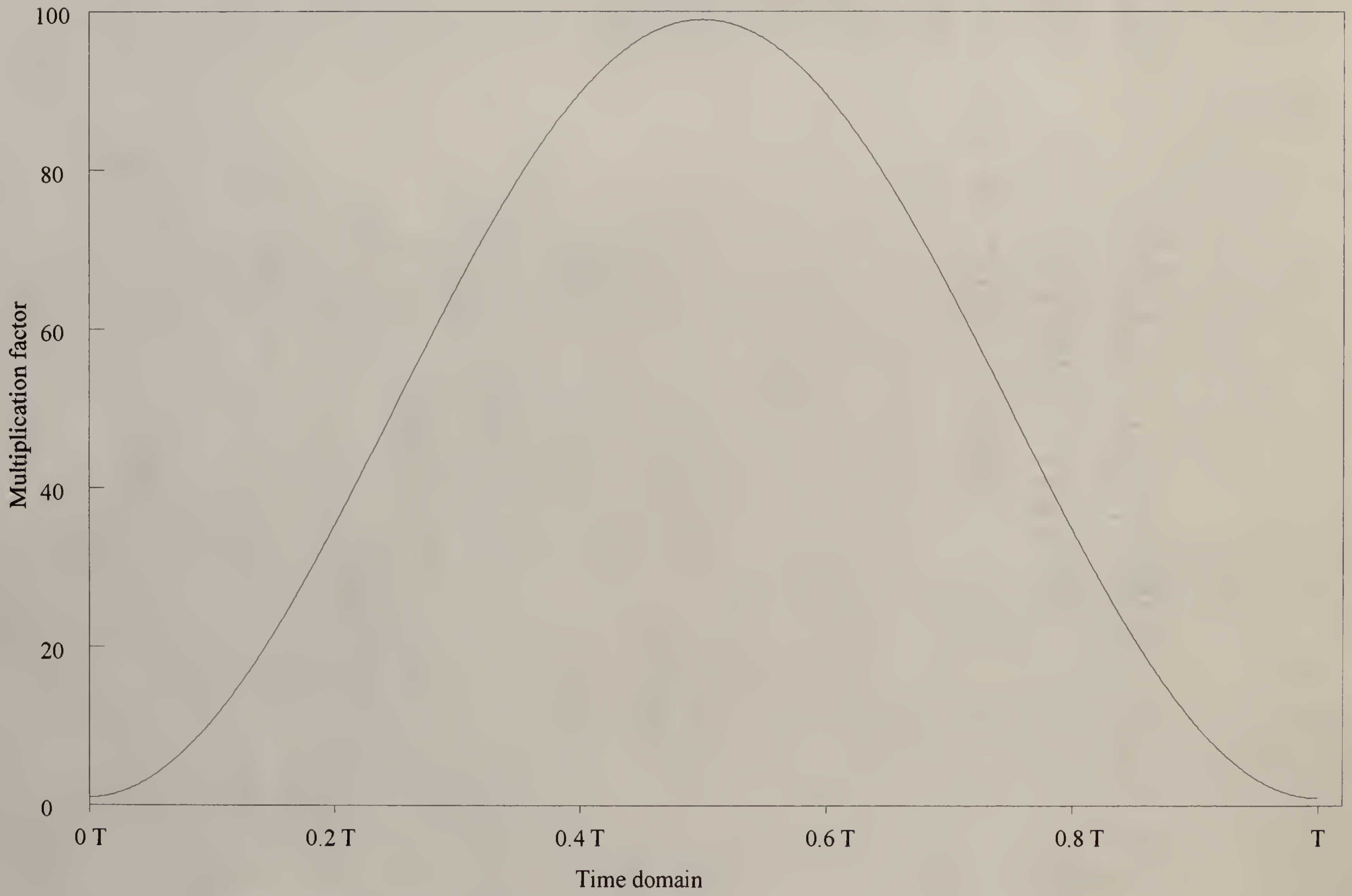

Figure 5.2--continued. (d) Hanning apodization

functions are shown in Table 5.1 along with graphical representations shown in Figure 5.2. Only these four apodization functions were used in this study, for two primary reasons. First, these are the more common apodization functions used for routine analysis. Second, the most successful method [119] for quantitating peak positions examined and obtained appropriate constants (*vide infra*) for only these four apodization functions.

Various degrees of zero filling were investigated to assess their effect on quantitation. Zero filling doubles the number of points to be transformed by adding zeros to the end of the transient signal, effectively interpolating points in the frequency (mass) spectrum after Fourier transformation. This is commonly done to increase the number of points defining peaks, thus decreasing the error in peak abundance determination. Investigations using no zero filling, and one, two, and three stages of zero filling were undertaken. The transient response signal for each zero filling stage was 1, 2, 4, or 8 times the size of the original transient and progressively longer processing times were required for the Fourier transformation [122]. Thus a total of 16 pre-transform manipulations (four apodization functions and four stages of zero filling) were applied to each transient response signal. Given the 24 simulated transient response signals, this resulted in a total of 384 spectra (after Fourier transformation), each with eight peaks, for a total of 3072 peaks which were evaluated in this investigation.

Two different methods of determining ion abundances were investigated: measurements of peak heights and peak areas. Five methods of determining peak heights were evaluated. The first method was simply to use the maximum data point as the measured value. This method is straightforward and simple to apply, but has the disadvantage that the value obtained is never the true maximum of the peak as the true maximum falls between data points defining the peak [119]. The other methods all involve interpolating the peak maximum by fitting the three data points of highest intensity to various functions. The various fitting functions can all be described by the function

$$Y=(aX^2+bX+c)^n \tag{2}$$

where n is dependent upon the type of interpolation desired. For this study parabolic (n=1), Lorentzian (n=-1), magnitude-Lorentzian (n=-0.5), and what will be termed the "Comisarow method" (n>1) were examined. The Comisarow method is based on optimized values of n for the various apodization functions [119]. These optimized values of n are 5.5 for Hanning apodization, 6.6 for Hamming apodization, 9.5 for 3-term Blackman-Harris apodization, and 12.5 for Kaiser-Bessel apodization.

The maximum value of a peak is determined in the usual way. Taking the first derivative of eq. 2 gives

$$Y'=n(aX^2+bX+c)^{n-1}(2aX+b) \quad . \tag{3}$$

The position of the maximum is found by setting Y' equal to zero and solving for X:

$$0=n(aX^2+bX+c)^{n-1}(2aX+b) \tag{4}$$

$$X_{max}=-b/2a \quad . \tag{5}$$

Neither of the first two terms on the right of eq. 4 is zero; n is either 5.5, 6.5, 9.5 or 12.5, and (aX^2+bX+c) is the value of the peak maximum and therefore when raised to a power will also be non-zero. Substituting the expression for X_{max} given by eq. 5 back into eq. 2 leads to

$$Y_{max}=(a(-b/2a)^2+b(-b/2a)+c)^n \tag{6}$$

$$Y_{max}=(-b^2/4a+c)^n \quad . \tag{7}$$

Therefore, solving three equations with the three unknowns (a, b, and c) allows the "true" peak maximum to be obtained. These three equations are

$$Y_1=(aX_1^2+bX_1+c)^n \tag{8}$$

$$Y_2=(aX_2^2+bX_2+c)^n \tag{9}$$

$$Y_3=(aX_3^2+bX_3+c)^n \tag{10}$$

where the three data points used are (X_1, Y_1), (X_2, Y_2), and (X_3, Y_3), which are those three points

closest to the top of the peak. There are many ways of determining the three unknowns; one of the best ways to solve these equations using matrix algebra. Rearranging eqs. 8-10 yields

$$(aX_1^2+bX_1+c)=Y_1^{1/n} \tag{11}$$

$$(aX_2^2+bX_2+c)=Y_2^{1/n} \tag{12}$$

$$(aX_3^2+bX_3+c)=Y_3^{1/n} \tag{13}$$

These three equations can be represented in matrix notation:

$$\begin{bmatrix} X_1^2 & X_1 & 1 \\ X_2^2 & X_2 & 1 \\ X_3^2 & X_3 & 1 \end{bmatrix} \begin{bmatrix} a \\ b \\ c \end{bmatrix} = \begin{bmatrix} Y_1^{1/n} \\ Y_2^{1/n} \\ Y_3^{1/n} \end{bmatrix} \tag{14}$$

$$A \quad V = H \tag{15}$$

Therefore, solving for a, b, and c is a matter of solving AV=H for V, which is accomplished by

$$A^{-1}AV=A^{-1}H \tag{16}$$

$$V=A^{-1}H \tag{17}$$

where A^{-1} is the inverse matrix of A. This procedure is repeated for each apodization function by changing the exponent, n, and thus the values in the H matrix.

Peak area as a measure of absolute signal intensity was also studied. It is known that in the mass domain the full width at half maximum (FWHM) for peaks in FTICR-MS increases with increasing mass [124]. This is true if one uses the mass domain, but if instead the frequency domain is used where the peak widths are constant, areas are a viable method for determining the peak intensities. Therefore, the frequency domain was used for all area determinations. Four methods for determining peak areas were examined: a trapezoidal, an "extended" trapezoidal, peak maximum multiplied by the FWHM, and the "integrated Comisarow" method.

One of the first considerations made when using areas for peak intensity measurements is to define where a peak begins and ends. For the two trapezoidal methods, the initial and final points of a peak were determined by systematically inspecting all points starting with the maximum and proceeding in both directions, finding the first data point of higher intensity than the preceding one (presumably corresponding to the end of the peak, where either ringing due to the Gibb's phenomenon, noise, or another peak caused an increase in intensity). The third method (FWHM x peak maximum) does not require such a determination, and the integrated Comisarow method will be discussed below.

The trapezoidal area is obtained by

$$\sum_{i=initial}^{i=final-1} \frac{1}{2}(X_{i+1}-X_i)*(Y_{i+1}+Y_i) \tag{18}$$

where X is the frequency of the data points, Y is the intensity of the data points, and initial and final are determined as described above.

Since the true maximum of the peak is not the data point of highest intensity, some of the total peak area is not being considered using the usual trapezoidal method. Therefore, an "extended" trapezoidal method was developed to include the true peak maxima approximated by including an additional triangular area whose vertices were the Comisarow interpolated maximum and the two adjacent data points.

Use of the FWHM x peak maximum has been suggested as an appropriate quantitation means in a paper by Marshall and co-workers [125]. This method is referred to here as the "triangle method", since in effect the area of a triangle of height equal to the peak maximum and base equal to 2*FWHM is determined. In the "triangle method" peak heights were obtained by the interpolated "Comisarow method" and the FWHM was determined by using a linear interpolation of two data points which spanned the true half maximum for each side of the peak. The FWHM was found by interpolating this to the value at the half maximum and determining the difference between the two sides of the peak.

The final method to estimate peak area was obtained by integrating the appropriate Comisarow fitting function. This approach is justified since the various functions described by Comisarow are able to fit the entire peak, even when using only the three most intense data points in order to determine the constants a, b, and c, as can be seen in Figure 5.3. The first

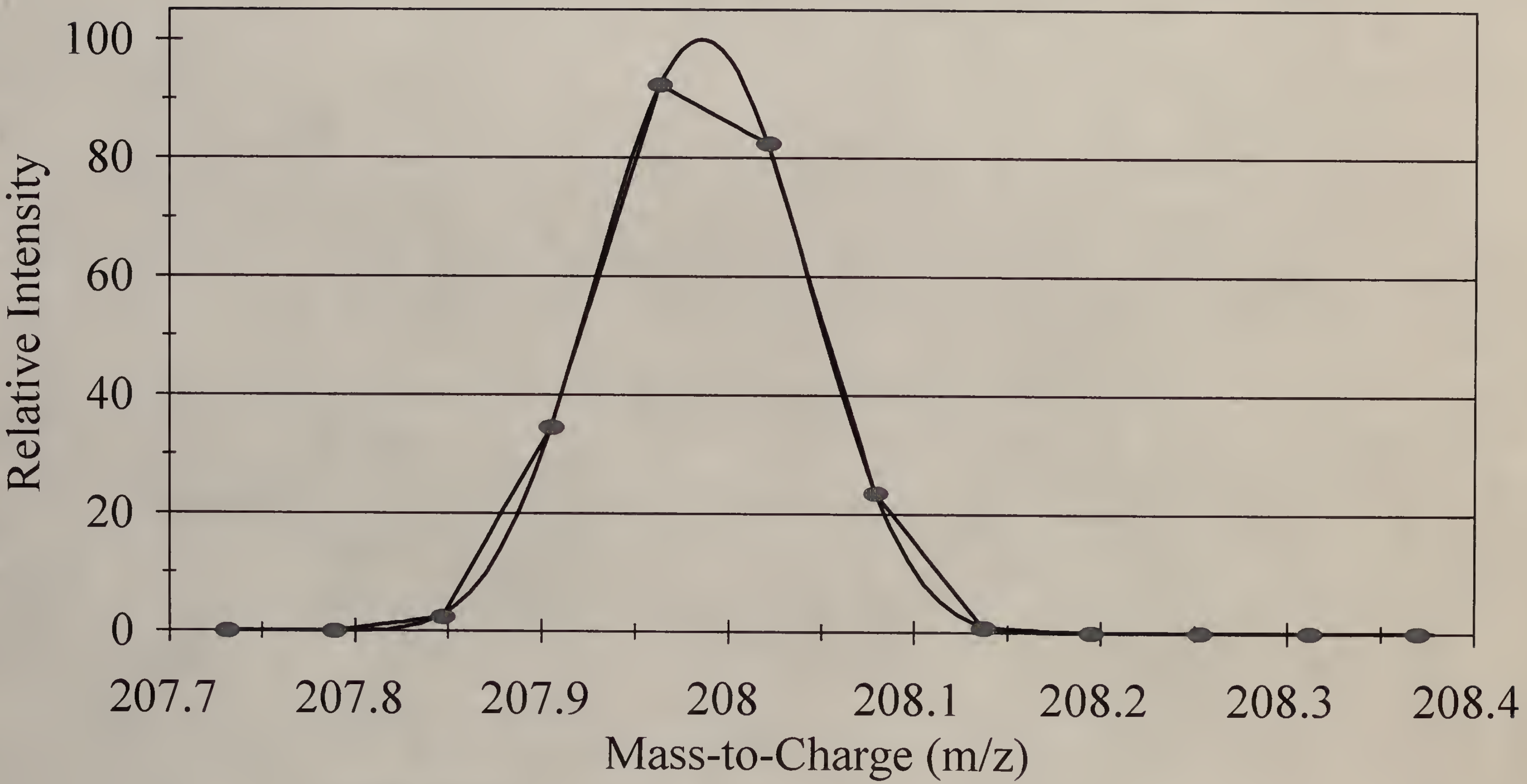

Figure 5.3: Peak fitting using the “Comisarow method” for $^{208}Pb^{+1}$ using a simulated 32k data size, no noise, 3-term Blackman-Harris apodization function, and no orders of zero filling.

step in this procedure is the determination of integration limits. The initial point for the integration was found by beginning at a frequency lower than that of the center of the peak by one FWHM, and then proceeding back toward the center of the peak until (aX^2+bX+c) was positive. The final point was likewise determined. This gives

$$\int_{initial}^{final} (aX^2+bX+c)^n \tag{19}$$

To solve this integral, n for the Hamming apodization was adjusted slightly to 6.5 instead of 6.6. This was done so that integration equations of the same functional form could be used for all four apodization methods. The integral for equation 19 ($z=n-\frac{1}{2}$) is evaluated from

$$\int \mathbb{R}^z\sqrt{\mathbb{R}}dx=\frac{(2z+2)!}{[(z+1)!]^2(4k)^{z+1}}\left[\frac{k(2ax+b)\sqrt{\mathbb{R}}}{a}\sum_{r=0}^{z}\frac{r!(r+1)!(4k\mathbb{R})^r}{(2r+2)!}+\int\frac{dx}{\sqrt{\mathbb{R}}}\right] \tag{20}$$

and

$$\int\frac{dx}{\sqrt{\mathbb{R}}}=\begin{cases}\dfrac{1}{\sqrt{a}}\sinh^{-1}\dfrac{2ax+b}{\sqrt{q}} & (a>0)\\[2ex] -\dfrac{1}{\sqrt{-a}}\sin^{-1}\dfrac{2ax+b}{\sqrt{-q}} & (a<0)\end{cases} \tag{21}$$

where $\mathbb{R}=(aX^2+bX+c)$, $q = 4ac-b^2$, and $k=4c/q$ [120]. This method of peak area determination will be referred to as the integrated Comisarow method.

For all analyses the average absolute percent error (AAPE) was used to describe the accuracy of the method. The formula for this is

$$AAPE = \frac{1}{N}\sum_{i=1}^{N}\frac{|Y_i - Y_t|}{Y_t} * 100\% \tag{22}$$

where N is the number of measurements, and Y_t is the true value.

All transient generation, apodization, zero filling, FFT, peak height and peak area measurements were performed using a 80486DX2-80MHz computer and the laboratory-written, Windows© based analysis package, WinICR [126, 127]. All calculations involving the simulation of transient responses were done using double-precision floating point variables.

Results and Discussion

Quantitation Based on Peak Height

A summary of the detailed study of the average absolute percent errors for the wide range of simulated data, zero-filling, apodization, and peak height determination revealed several general patterns, as illustrated in Figure 5.4. The x-axis is labeled by 0, 1, 2, and 3, which represent the number of zero fills applied to the data before Fourier transformation. Results are shown for the three different simulated noise levels (“Single Scan” for the high

Figure 5.4: Bar graph showing the Average Absolute Percent Error (AAPE-eq. 23) obtained when using peak heights as a method for quantitation of ion abundances for various fitting functions, noise levels, and orders of zero filling. Along the x-axis are the 3 types of simulated spectra with the degree of zero filling for each type bracketed. Along the y-axis are the fitting techniques used. The arrows on some bars indicate that they are off-scale and have the value above the arrow.

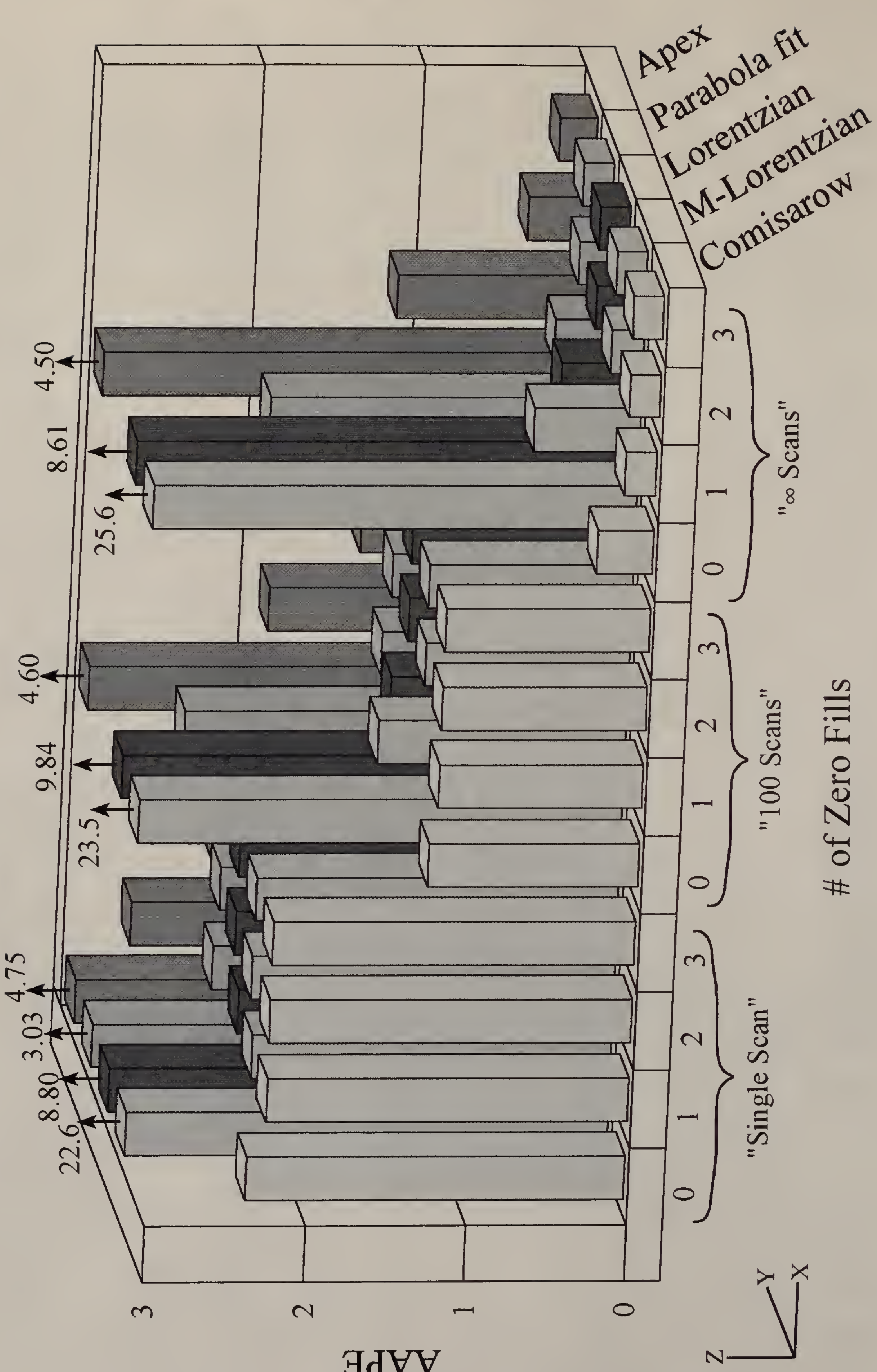
AAPE
0
1
2
3
Apex
Parabola fit
Lorentzian
M-Lorentzian
Comisarow
22.6
8.80
3.03
4.75
23.5
9.84
4.60
25.6
8.61
4.50
0
1
2
3
"Single Scan"
"100 Scans"
"∞ Scans"
# of Zero Fills
X
Y
Z

noise set, “100 Scans” for the moderate noise set, and “∞ Scans” for the no noise set) described above. The y-axis is labeled “Apex”, “Parabola fit”, “Lorentzian”, “M-Lorentzian”, and “Comisarow” for the highest point, parabolic fit, Lorentzian fit, magnitude-Lorentzian fit, and the Comisarow method peak height determination, respectively. The z-axis corresponds to the average absolute percent error (AAPE) for the particular peak height determination described by the X- and Y- axis labels. A Hanning apodization function was used for all of the data shown in this particular figure. Results for other apodization functions are discussed below.

As expected, there is a marked decrease in the average absolute percent error as the noise level is decreased. The lowest AAPE is about 2.2 for the single scan set, 1.5 for the 100 scan set and 0.2 for the ∞ set. As the number of scans increase, the noise decreases, resulting in less random noise interfering with accuracy of peak height measurements. Precise peak quantitation here becomes a trade-off between additional time required to make additional measurements versus the accuracy level desired. The signal-to-noise increases as the square root of the number of scans [121], so decreasing the noise level by another factor of ten from the moderate noise levels would be comparable to an experiment with 10,000 rather than 100 scans.

When the effects of zero filling are examined, other trends become evident. As the degree of zero filling increases, so does the accuracy of the measurements. This is true for all levels of noise and all interpolation methods. This behavior is only indirectly related to the degree of zero-filling, and is directly linked to the increased numbers of points spanning the peaks with increased zero filling. Examination of Figure 5.4 revels a sharp reduction in absolute percent error for all noise levels and all peak height determination functions when moving from no orders of zero filling to one order of zero filling. Only slight improvements in absolute percent error are seen with additional zero filling. These results point to one zero filling as the optimum amount. While 3 zero fills gives slightly better accuracy, the required time for Fourier transformation of the data increases 8-fold. As stated earlier, increased zero-filling leads to more points spanning each peak. For these spectra there were approximately 6, 11, 22, and 45 points spanning the peak for zero, one, two, and three zero fills, respectively. Therefore, an adequate number of points per peak for the peak height determination methods used is in the range of 10 to 20.

Finally, examination of Figure 5.4 suggests the best method for determining peak heights for selected acquisition and processing conditions. It is apparent that with no zero-filling the method based on Comisarow's fitting equations is by far the best for determining peak heights. As the number of points spanning a peak increases, other methods become comparable to the one based on Comisarow's equation. However, with only one zero fill (11 points defining a peak) the "Comisarow method" performs as well as any method at any zero fill level. A minimal improvement can be seen at the higher degrees of zero-filling when using the Comisarow method, on the order of 0.5% improvement for two orders of zero filling over one order and 0.01% improvement of three orders of zero filling over two orders. Thus, in this study the Comisarow method either was statistically the same as, or was superior to, every other method of peak height determination. This result is not unexpected, since these fitting functions were shown [119] to be the best for determining the center position of the peak in the frequency (mass) scale, and thus should be best for determining the peak intensity at the true peak frequencies. The Lorentzian and Magnitude Lorentzian do not perform as well as the other methods since these peak fitting methods are for unapodized spectra. They have been included for completeness and in order to test their usefulness with apodized spectra.

While data represented in Figure 5.4 were obtained using the Hanning apodization function, other apodization functions used in this study produced similar results. The Hamming, 3-term Blackman-Harris, and Kaiser-Bessel apodization functions all led to results which, when put in a format similar to Figure 5.4, showed the same trends and roughly the same AAPE's. However, the other apodization functions do not provide AAPE's quite as low as does the Hanning function. The 3-term Blackman-Harris yield AAPE's about 4% larger than those obtained using the Hanning function. Likewise, the Kaiser-Bessel results are about 6% larger than those from the Hanning function. This is to be expected since the dynamic ranges of measured peaks are approximately 1:2, 1:2, and 1:37. As stated earlier, the Hanning apodization is recommend for a dynamic range of 1:10, the 3-term Blackman-Harris apodization for 1:100, and the Kaiser-Bessel apodization for 1:1000. Since the peaks were closest to 1:10, Hanning apodization provided the best results. Likewise, the 3-term Blackman-Harris apodization was next closest to the dynamic ranges of the peaks and it was the next best apodization function. Lastly, the Kaiser-Bessel apodization is farther away from the suggested dynamic range than the Hanning apodization and the 3-term Blackman-Harris apodization and the results were poorer. Finally, the Hamming function results in AAPE's 40% larger than those shown in Figure 5.4. The differences between the 3-term Blackman-Harris, the Kaiser-Bessel, and the Hanning functions are not very significant, but the Hamming function, with such large AAPE's, is clearly not the best choice. This dramatic worsening in accuracy is attributed to the larger side lobes on peaks when the Hamming apodization function is applied, which interfere with peak height determination of neighboring peaks, especially the Pb^{+2} peaks at 103, 103.5, and 104 m/z.

Since the most accurate results were obtained when using the Hanning apodization, one order of zero filling, and the Comisarow method for peak height determination, these parameters were used to investigate the effects of data size and exponential signal damping. Results of these investigations are summarized in Figure 5.5. For undamped transients, a monotonic decrease in the AAPE is seen with increasing data set size. This is to be expected since as the number of data points (the x-axis) is increased, the signal-to-noise increases and therefore the 3 points used in the interpolation have a smaller fraction of noise interfering with accurate determinations. The curve labeled “Damped” is somewhat less straightforward due to the fact that not only is the data set size changing, but also the T/τ. It has been previously shown that the interpolation accuracy decreases with increasing T/τ [117 - 119]. This explains the general upward trend seen for the first part of the curve; however, it is believed that the increased signal-to-noise and therefore the increased accuracy of the interpolation points overrides the increased error from greater T/τ ratios for the larger data sets. Since T/τ is 4 for the 128k data set size, these results would argue against further acquisition since the signal would fall by the end of the transient response signal to only 2% of that at the beginning.

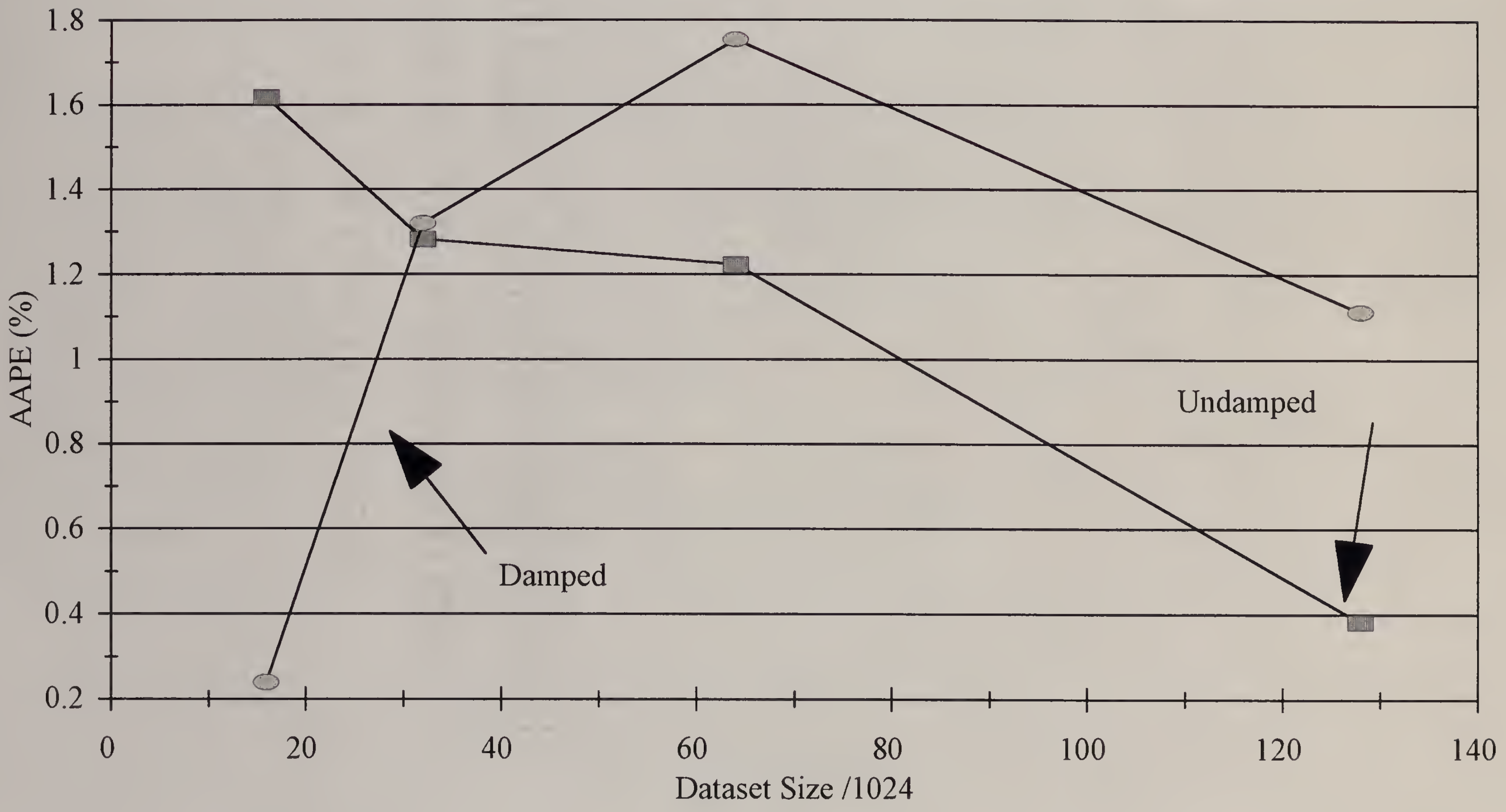

Figure 5.5: Effect of data set size on AAPE using Hanning apodization, moderate noise level, one order of zero filling and the "Comisarow method" of peak height determination for damped and undamped transient response signals.

Quantitation Based on Peak Area

Given that several quantitation approaches based on peak area use the peak height as one factor in the area determination, one would expect similar quantitation results for the two methods. In fact, this is seen when comparing Figure 5.6 to Figure 5.4. As in Figure 5.4, the x-axis of Figure 5.6 is labeled by 0, 1, 2, and 3 corresponding to the order of zero filling, for transients with high, moderate, and zero noise applied. The y-axis is labeled with the method for determining peak area: “Trapezoidal”, “Trapezoidal +”, “Max*FWHM”, and “Integrated Comisarow” for the trapezoidal method, the trapezoidal plus the additional area for the interpolated maximum, the ‘triangle’ method obtained by multiplying the maximum by the FWHM, and the value obtained from integrating the optimal Comisarow fitting function corresponding to the chosen apodization function, respectively.

As with peak height, a decrease in the noise level resulted in improved accuracy. The AAPE’s decreased from ~2.6 for the high noise data to ~1.6 for the moderate noise data to ~0.4 for transients generated with no noise. However, these AAPE’s are all slightly *higher* than those obtained using peak height for quantitation. Also, the data in Figure 5.6 again indicate that one degree of zero filling gives the best compromise between quantitation and increased transformation times.

Perhaps the most significant results shown in Figure 5.6 are the comparisons between methods used for determining peak area. Focusing first on the two trapezoidal methods, it is clear that the two methods give almost identical results, particularly for the data with

Figure 5.6: Bar graph showing the Average Absolute Percent Error (AAPE-eq. 23) obtained when using peak areas as a method for quantitation of ion abundances for various fitting functions, noise levels, and orders of zero filling. Along the x-axis are the 3 types of simulated spectra with the degree of zero filling for each type bracketed. Along the y-axis are the fitting techniques used. The arrows on some bars indicate that they are off-scale and have the value above the arrow.

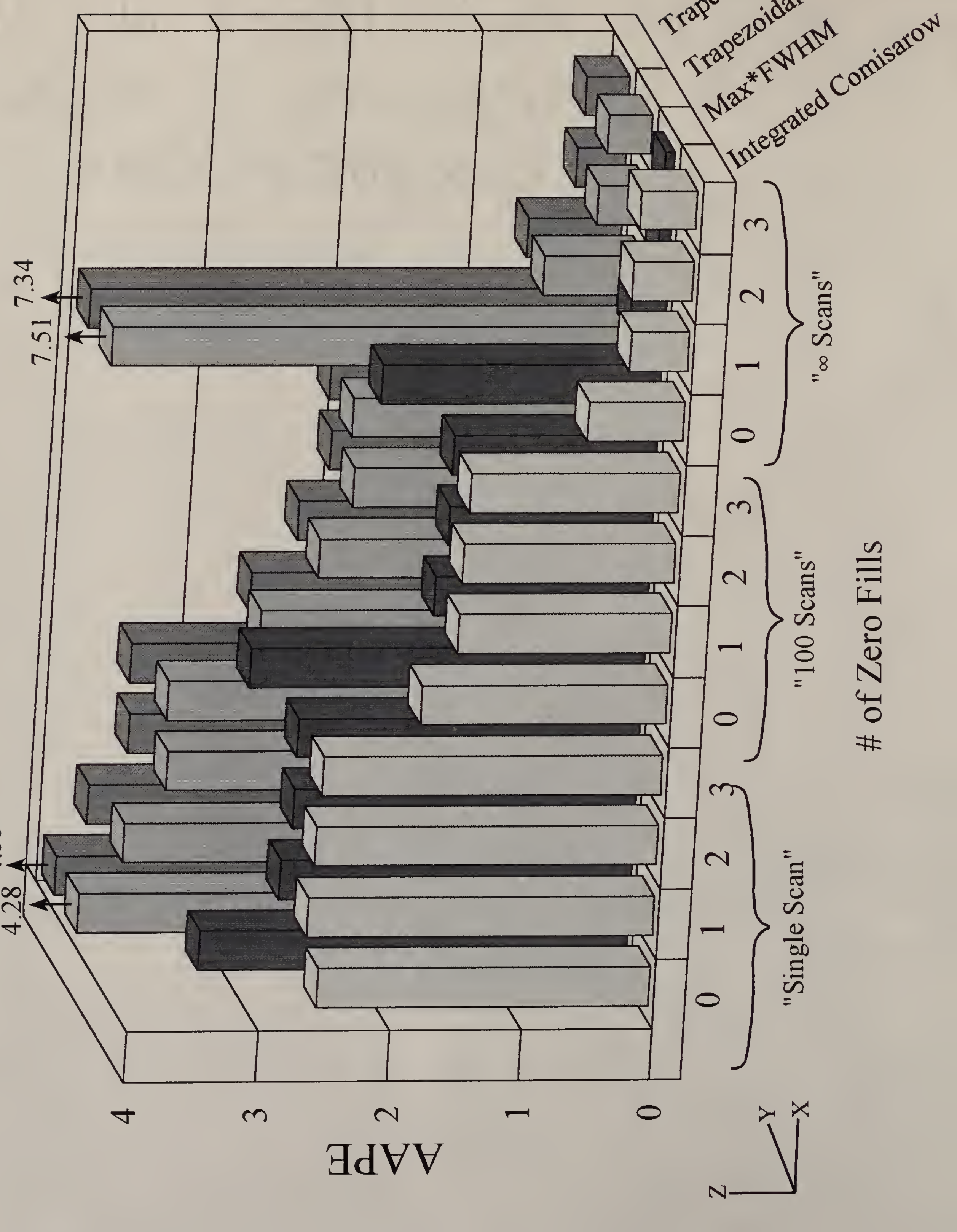
AAPE
0
1
2
3
4
Z
Y
X
"Single Scan"
"100 Scans"
"∞ Scans"
0
1
2
3
# of Zero Fills
Trapezoidal
Trapezoidal + Max*FWHM
Integrated Comisarow
4.28
4.33
7.51
7.34

moderate and no noise. Only for the high noise case was the "Trapezoidal +" method noticeably better. The lower AAPE in this case can be related to the use of the "Comisarow method" for peak height determination in the "Trapezoidal +" method. It can be seen in Figure 5.4 that interpolation with the appropriate Comisarow fitting function provides good results, even in the highest noise case. Thus the additional area added in the "Trapezoidal +" method, presumably determined with good accuracy, helps offset errors from the higher noise data of the rest of the peak.

The "triangle" method and the integrated Comisarow methods yield similar results for high and moderate noise cases (except with no zero filling, where the integrated Comisarow method is considerably better for all noise levels). For the case of no noise, the triangle method is noticeably better in the cases with multiple degrees of zero filling. The most reasonable explanation for this behavior is simply that with no noise, the peak maximum (using the Comisarow method) and the FWHM are determined with high accuracy which translates into high accuracy, for the triangle method. The results would, of course, be much poorer if the observed peak maximum were used in place of the interpolated maximum obtained from the appropriate Comisarow function.

As noted above, the moderate noise case analyzed is most similar to that seen in typical FTICR-MS spectra. This leads us to suggest that either the integrated Comisarow method or the triangle method would be best for calculating peak areas based on the results shown in Figure 5.6.

All results shown in Figure 5.6 were obtained using a Hanning apodization function. As was the case with peak heights, the Hanning apodization function gave the lowest AAPE's for peak area determination as well, with AAPE's from 3-term Blackman-Harris apodization higher by 1.5%, from Kaiser-Bessel apodization higher by 2%, and from Hamming apodization higher by 60%. From these results, it is apparent that the Hamming apodization function is undesirable for these methods of quantitation, and that one of the other three apodization functions (Hanning, 3-term Blackman-Harris, or Kaiser-Bessel) should be used as suggested by Comisarow depending on the dynamic range required [109].

Figure 5.7 shows the AAPE's for damped and undamped transients of increasing numbers of data points, for the moderate noise case, one order of zero filling, and Hanning apodization. It is quite similar to Figure 5.5, except that the data from peak area rather than peak height quantitation are plotted. Quantitation using two methods for determining peak areas, the "triangle" and the integrated Comisarow function methods was considered. Similar trends are seen with peak area as were seen in peak height. There is a general decrease (with an anomalous initial point) for the undamped signal due to signal-to-noise improvement, and an initial increase and then decrease in the AAPE's from damped transient. The competing factors of increased errors due to increasing the T/τ ratio and the decrease in error due to improved signal-to-noise from having a larger data set size are once again evident.

Peak Ratio Measurements

In many analyses, analytical and otherwise, peak ratio measurements are utilized. The results obtained when measuring peak ratios are completely analogous to those shown. One important concern is the accuracy of peak ratios for peaks in a narrow m/z range compared to those in a wide m/z range. To address this concern, peak ratios were determined from

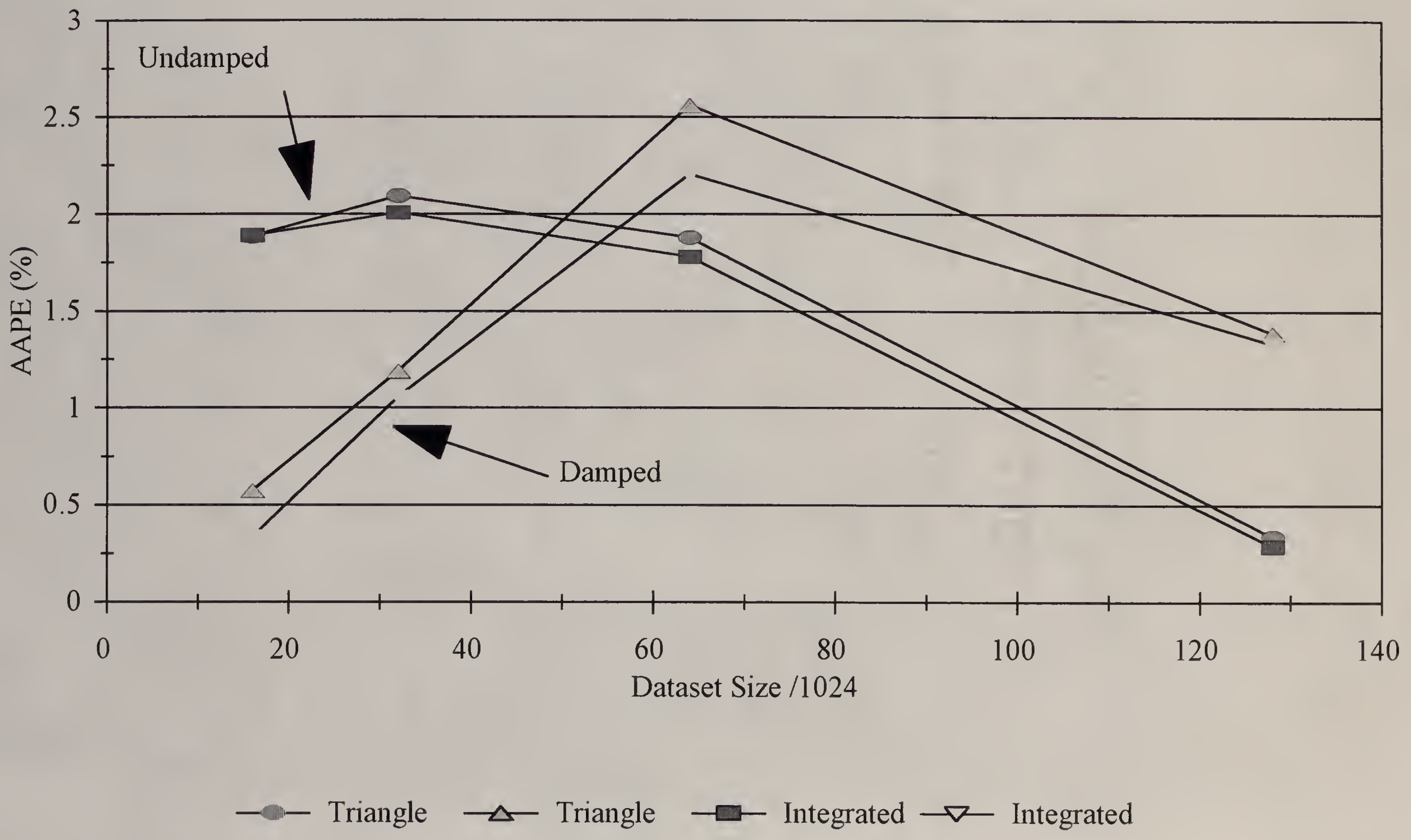

Figure 5.7: Effect of data set size on AAPE using Hanning apodization, moderate noise level, one order of zero filling and the "Comisarow method" and "triangle method" of peak area determination for damped and undamped transient response signals.

analysis of the simulated data for the isotopes of Pb^{+1} and the isotopes of Pb^{2} (thus considering data in a narrow m/z range), and for the isotopes of Pb^{+1} ratioed to those of Pb^{+2} (wide m/z range). Ratios of peaks in the narrow m/z ranges were about 5% more accurate than ratios of peaks in the wide mass ranges. This is understandable since the best results from such measurements are when the two species are similar. Also the overlap of the side lobes is different for the two sets of peaks, which could contribute to the poorer performance for the wide m/z range.

Unknown Quantitation

To evaluate the usefulness of this technique xenon gas was used as an unknown. The nine isotopes of xenon are: ^{124}Xe (0.10 %), ^{126}Xe (0.09 %), ^{128}Xe (1.91 %), ^{129}Xe (26.4 %), ^{130}Xe (4.1 %), ^{131}Xe (21.2 %), ^{132}Xe (26.9 %), ^{134}Xe (10.4 %), and ^{136}Xe (8.9 %). Only seven of the nine isotopes were investigated in this study since ^{124}Xe and ^{126}Xe were not detectable from the noise in the spectra used for quantitation. Thirty spectra were analyzed, with each spectrum being obtained by summing 100 transient response signals prior to Fourier transformation. The thirty spectra were background corrected, apodized using the Hanning apodization (appropriate given the dynamic range of the peaks involved), modified by various degrees of zero filling (0-3), and transformed. The thirty spectra were divided into three groups of ten, which were analyzed and then peak heights and areas averaged. This yielded three sets of peak heights and areas for error analysis. The first set was used as a reference sample in order to obtain RSFs for use in the second and third sets. Using the RSFs, as

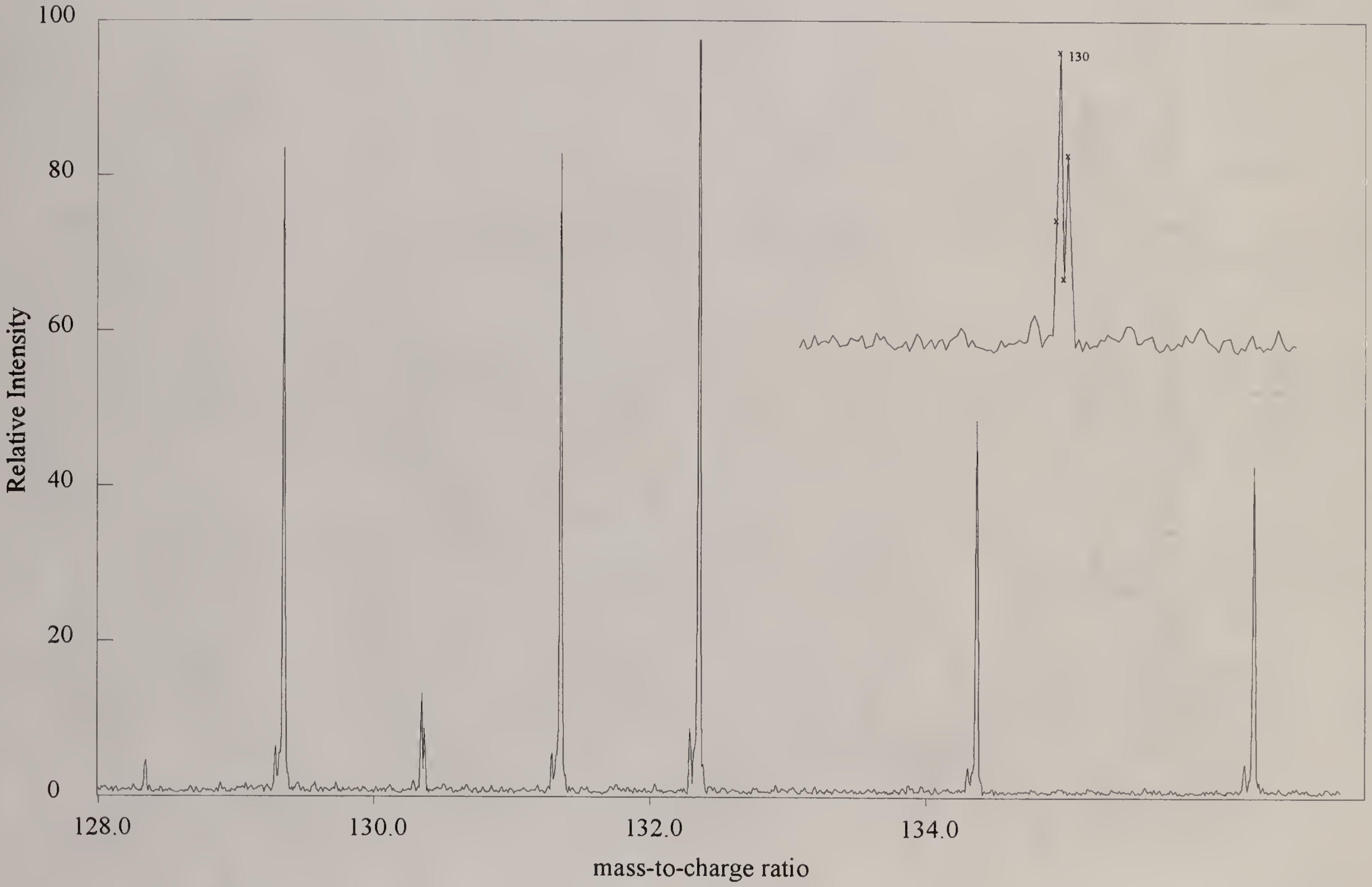

Figure 5.8: Mass spectrum of xenon used for the unknown quantification. The inset shows an expanded view of ^{130}Xe which clearly shows the splitting of the peak due magnet inhomegenity. The individual data points for ^{130}Xe are marked in order to illustrate the problems the difficulty with accurate interpolation caused by the splitting.

described in Chapter 2, peak heights and areas were obtained by the methods discussed earlier in this chapter. Percent errors were obtained for each peak as compared to the natural abundance. The absolute values of these errors were then averaged. This provides information most comparable with that discussed earlier in this chapter for the simulated data sets.

A spectrum typical of the quality of the thirty used for this study is shown in Figure 5.8. This spectrum is similar in signal-to-noise ratio and dynamic range of peaks to that shown in Figure 5.1b, which resulted from transformation of simulated data. This indicates that these xenon spectra provide good "real" data for testing peak quantitation. The inset in Figure 5.8 shows severe splitting of the $^{130}Xe^{+}$ peak. One can see the individual data points and notice that the data point directly after the peak maximum is much lower than it would be if the peak were not split. This splitting is attributed to poor homogeneity of the prototype 2T magnet used to obtain the data. This splitting can be seen in the other peaks as well, but the splitting is not as dramatic as with ^{130}Xe, and is along the baseline. Due to the splitting of ^{130}Xe, it was not used in the study. Thus only six isotopes of xenon were used in this study.

The data in Figure 5.9 is very similar to that seen in Figure 5.4. Figure 5.9 is a bar graph of the AAPEs of the five peak height determination methods for the various stages of zero filling for each trail. At no orders of zero filling both the parabolic and Comisarow interpolation methods provide much lower AAPE than either the Lorentzian or magnitude-Lorentzian. The parabolic and Comisarow interpolation methods show a 56.7 % and a 44% improvement over using the apex method. As seen earlier, with increasing orders of zero filling the error decreases. However, after one order of zero filling the improvements are

Figure 5.9: Bar graph showing the Average Absolute Percent Error (AAPE-eq. 23) obtained when using peak heights as a method for quantitation of ion abundances for various fitting functions and orders of zero filling. Along the x-axis are the 2 trials of xenon spectra with the degree of zero filling for each trial bracketed. Along the y-axis are the fitting techniques used. The arrows on some bars indicate that they are off-scale and have the value above the arrow.

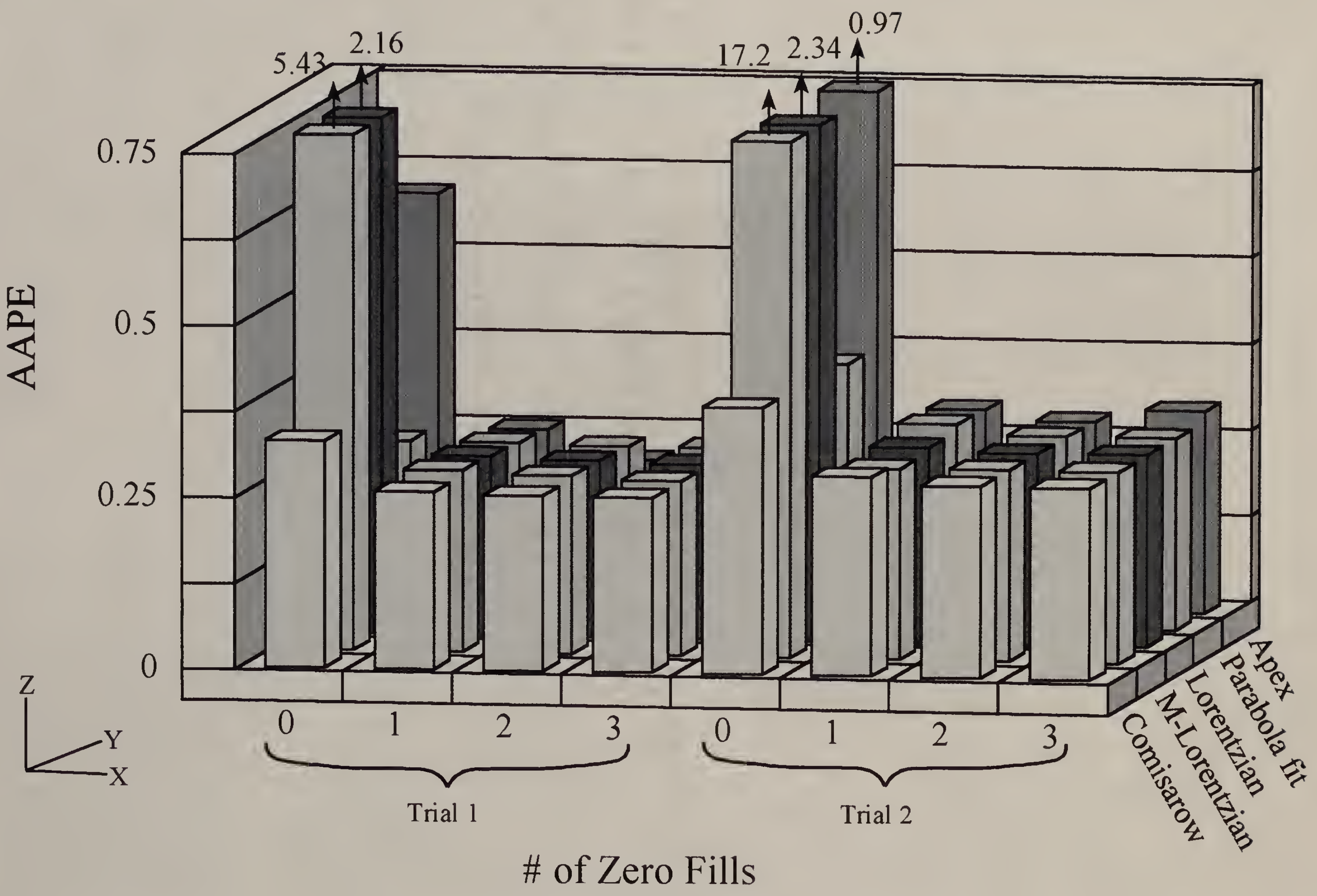
AAPE
0.75
0.5
0.25
0
5.43
2.16
17.2
2.34
0.97
0
1
2
3
0
1
2
3
Trial 1
Trial 2
# of Zero Fills
Apex
Parabola fit
Lorentzian
M-Lorentzian
Comisarow
Z
Y
X

meager. The parabolic interpolation gave better results in this case than when simulated data were used. This could be due to the peak shapes differences in the “real” spectra (using the prototype magnet with poor homogeneity) and the simulated spectra (using a “perfect” magnet). These results using a “real” sample show that both the parabolic and Comisarow methods should be used with no orders of zero filling for the best results. If one order of zero filling is used, it would not make much difference which, if any, interpolation was used in this case. However, in the simulated example it took two orders of zero filling before there was negligible difference between the apex and various interpolation methods. Therefore, the suggested methodology of one order of zero filling, and the Comisarow interpolated peak height provides the best general purpose way to determine ion intensities.

Figure 5.10 is a bar graph similar to that shown in Figure 5.6. This bar graph shows the two trials and the various stages of zero filling along the x-axis and the AAPE for the different peak area methods along the z-axis. Similar conclusions can be drawn from this figure as could be drawn from Figure 5.6. Regarding trial one, the integrated Comisarow method of determining peak area is the best method. It is better than the Max x FWHM (“triangle”) method by an average of 30.1%. In trial two, the integrated Comisarow method gave better results by an average of 65.1% over the “triangle” method. In the simulated case the two methods performed almost identical (for the moderate noise level case). The data obtained using a “real” sample corroborate the suggestion to use the integrated Comisarow method when a measure of peak area is desired for quantitating ion abundances.

Figure 5.10: Bar graph showing the Average Absolute Percent Error (AAPE-eq. 23) obtained when using peak areas as a method for quantitation of ion abundances for various fitting functions, noise levels, and orders of zero filling. Along the x-axis are the 3 types of simulated spectra with the degree of zero filling for each type bracketed. Along the y-axis are the fitting techniques used. The arrows on some bars indicate that they are off-scale and have the value above the arrow.

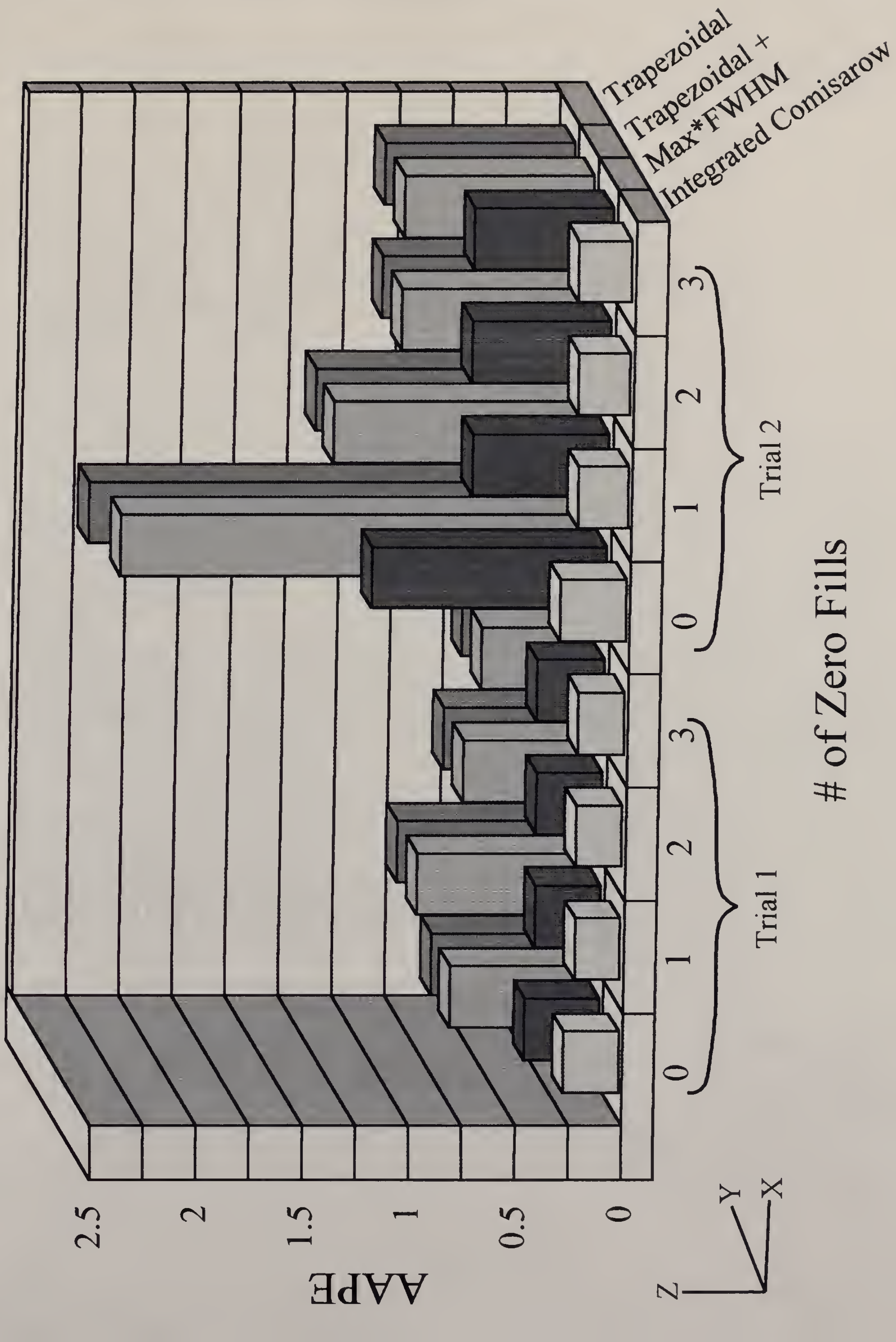
AAPE
2.5
2
1.5
1
0.5
0
# of Zero Fills
0
1
2
3
Trial 1
0
1
2
3
Trial 2
Trapezoidal
Trapezoidal +
Max*FWHM
Integrated Comisarow
Z
Y
X

Conclusions

Application of various apodization functions and degrees of zero filling to simulated ion transients, followed by Fourier transformation, generated a series of mass spectra which were analyzed to determine the most accurate methods of peak quantitation. Based on these results, several suggestions for the best method of peak quantitation in FTICR-MS can be made. Starting with the transient signal collected, either the Hanning, 3-term Blackman-Harris, or Kaiser-Bessel apodization functions should be used depending on the desired dynamic range of the analyte. The time-domain spectrum should be zero filled until there are between 10 and 20 points spanning each peak of interest. After Fourier transformation, a peak height interpolation based on a fitting function appropriate to the apodization function used [109] should be used to maximize accuracy. Experimental data confirm these results, but also show that parabolic interpolation is capable of providing quality results and should not be ignored. If peak area determinations are desired, either the "integrated Comisarow" method or the triangle method should be used. Experimental data corroborate these findings and show that the "integrated Comisarow" method is best for determining peak areas.

CHAPTER 6
CONCLUSIONS

The primary motivation for performing the research described in this thesis was an attempt to find possible solutions to the isobaric interference problem. Two such solutions to this problem were explored and reported. The first was the prospect of using secondary discharge species for quantitating the analyte, and the second was the prospect of using a GD probe/source within the high magnetic field of an FTICR-MS in order to take advantage of high ion transport efficiency and the ultra-high mass resolution seen in FTICR-MS.

Metal argides, metal dimers, and doubly-charged metal ions are useful for quantitation when the analyte is obscured by interference peaks. This technique gives reasonable accuracy (ca. 15% relative error) if the elemental composition is approximately 0.1% or greater of the sample. Below this the measurement errors for the trace species are larger than for the elemental species . It is important to look at all candidate species when using alternative quantitation techniques since one or more may give false results if they are also interfered with. While this technique should be used with caution, it was demonstrated that it gives the analyst a viable alternative in those cases where it is impossible to address interferences in other ways. This technique is only applicable to relatively abundant species (>0.1%). Therefore, if the analyte of interest is not present in high enough concentration, then another technique must be used. One alternate possibility is using the ultra-high resolution of

FTICR-MS along with the high transport efficiency afforded with locating the GD probe/source within 25 cm of the analyzer cell.

Glow discharge sources *do* work when located inside the FTICR magnetic field and the probe/source design presented here has the added benefit of a lower sputtering rate, which enhances LODs. The relative proximity of the source to the FTICR cell results in higher ion transport efficiency when compared to previous external injection methods. The thirty fold improvement in ion transport seen in this work gives limits of detection comparable to external injection (low ppm), but with significantly lower sample consumption, leading to a limit of detection of 25 picograms for ^{60}Ni. Finally, it has been shown that the behavior of a glow discharge with this probe/source design in a magnetic field of approximately 1.5 Tesla is comparable to that when no magnetic field is present. This supports the idea that FTICR-MS will have an important role in the future for highly interfered samples. This will require analytical quantitation using FTICR-MS, but formalized methods of quantitation in FTICR are lacking. This naturally leads to experiments in determining the optimum method of quantitation using FTICR-MS.

Application of various apodization functions and degrees of zero filling to simulated ion transients, followed by Fourier transformation, generated a series of mass spectra which were analyzed to determine the most accurate methods of peak quantitation. Based on these results, several suggestions for the best method of peak quantitation in FTICR-MS can be made. Starting with the transient signal collected, either the Hanning, 3-term Blackman-Harris, or Kaiser-Bessel apodization functions should be used depending on the desired dynamic range of the analyte. The time-domain spectrum should be zero filled until there are between 10 and

20 points spanning each peak of interest. After Fourier transformation, a peak height interpolation based on fitting function appropriate to the apodization function used should be used to maximize accuracy. If peak area determinations are desired, either the "integrated Comisarow" method or the triangle method should be used.

This thesis has demonstrated two methods for solving the isobaric interference problem. If the analyte is relatively abundant (>0.1%) then the first method is applicable. If the analyte is not that abundant or ultra-high resolving power is required, then using GD-FTICR-MS (using the quantitation methods outlined) is better choice for sample analysis.

GLOSSARY

ppm	parts-per-million
AAPE	average absolute percent error.
FTICR	Fourier transform ion cyclotron resonance
GD	glow discharge
MS	mass spectrometry
ICP	inductively coupled plasma
$m/\Delta m_{1/2}$	resolution as measured by the mass divided by the FWHM
FWHM	full width at half maximum
ω_c	cyclotron frequency
ω_T	trapping frequency
ω_m	magnetron frequency
B	magnetic field
q (or z)	charge on an ion
z (or q)	charge on an ion
m	mass of an ion
RSF	relative sensitivity factor
IBR	ion beam ratio
rf	radio frequency

dc	direct current
SWIFT	stored waveform inverse Fourier transform
LOD	Limit of detection
RSD	Relative Standard Deviation

APPENDIX A:
BASIC CODE FOR DETERMINING INTERPOLATED HEIGHTS AND AREAS USED IN CHAPTER 5

```
PROCEDURE  list_lines_fit

 '                        List lines for data after FT but still linear in freq.

 IF llfs$ = "" THEN llfs$ = "N"
 IF llfs2$ = "" THEN llfs2$ = "Y"
 afile$ = ppath$ + "ll.tmp"
 IF llfs$ = "Y"
  OPEN "a", #5, afile$
 ENDIF
 IF llfs$ = "N"
  OPEN "o", #5, afile$
 ENDIF
 'PRINT #5, dfile$
 'PRINT #5, "     m/z          Int.          Trap. area    INT. m/z      PAR INT. Int.    LOR
INT. int   MAGLOR INT int.   BEST INT int    FWHM      Resol       Int x FWHM     INT.
trap. area  Integ
 '=>>"
 'PRINT
#5,"----------------------------------------------------------------------------------------------------
-------------------------------------------------------------------------------------
 '=>>   "

 DIM freq(3,3),freqInv(3,3),heights(3,1),abc(3,1),klg(200)

 IF dst$ = "massf" THEN

  @mass_to_index(mr1)                                         'get left start point
  ilow = i_dex
  @mass_to_index(mr2)                                         'get right start point
  ihigh = i_dex

  IF ilow < 1 THEN ilow = 2
  IF ihigh > ndp THEN ihigh = ndp - 1
```

```
pmax = xr(ilow)
pmin = xr(ilow)
FOR i = ilow TO ihigh
 IF xr(i) > pmax THEN pmax = xr(i)                         'find highest point
 IF xr(i) < pmin THEN pmin = xr(i)                         'find lowest point
NEXT i
prange = pmax - pmin                                        'range

@mass_to_index(mr1)                                        'same as above
ilow = i_dex
@mass_to_index(mr2)
ihigh = i_dex

IF ilow < 1 THEN ilow = 1                                  'precautions
IF ihigh > ndp THEN ihigh = ndp

FOR i = ilow + 1 TO ihigh - 1                 'from begin to end of spectrum
 '************************************************

 peak = 100 * ((xr(i) - pmin) / (prange))     'converts intensity to % relative intensity
 pmim = prange * (mi / 100)                              'above threshold (mi)

 IF xr(i) > xr(i + 1) AND xr(i) > xr(i - 1) AND peak > mi    'Peak top?

  @index_to_mass(i)                            'converts index number to mass
  regmass = massz
  IF massz >= mr1 AND massz <= mr2 THEN      'is within viewing region?

   ipmax = i
   @remap                                ' temp. remaps peaks to lower indeces

   regheight = xr(i)                       'intensity of data point(peak)

   ' We now have a peak within mr1 and mr2
   'now we do the interpolations
   '=====================================================================
   n = 1                                   'parabola
   @peakfitting2                        'subroutine call for interpolating the peak
   maxheight = maxpoint                    'interpolated max for parabola
   freqzPAR = freqzfit
   n = -1                                  'Lorentzian
   @peakfitting2
```

```
maxheightLOR = maxpoint                    'interpolated max for Lorentzian
freqzLOR = freqzfit
n = -0.5                                 'Magnitude-Lorentzian
@peakfitting2
maxheightMAGLOR = maxpoint        'interpolated max for Magnitude-Lorentzian
freqzMAGLOR = freqzfit

'------------assigning the correct exponent for the Comisarow method
IF apodization = 1
  n = 5.5                                'For Hanning
ELSE IF apodization = 2
  n = 6.6                                'For Hamming
ELSE IF apodization = 3
  n = 9.5                                'For Blackman-Harris
ELSE IF apodization = 4
  n = 12.5                                'For Kaiser-Bessel
ELSE IF apodization = 0
  n = 1.5                              'for nothing
ELSE IF apodization = 5                   'for Noest-Kort
  n = 9.5
ENDIF



@peakfitting2
maxheightbest3 = maxpoint       ' interpolated max for Comisarow
freqzCOM = freqzfit

@index_to_mass(freqzCOM)          'interpolated mass for Comisarow
masszCOM = massz

abc(1,1) = abc(1,1)
abc(2,1) = abc(2,1)
abc(3,1) = abc(3,1)
max3 = (-abc(2,1)) / (2 * abc(1,1))

@FWHM                           'subroutine call for determining the FWHM
@integration                    'subroutinge call for the Comisarow integration
@area_trap                      'sub call for trap. area and extended trap. area
integratedarea1 = integratedarea

IF apodization = 4         'used when testing the Comisarow number for
  n = 10.5                 'Kaiser-Bessel.  12.5 is good, 10.5 is better (0-1 %)
```

```
 '        @peakfitting2
  maxheightbest4 = maxpoint
  freqzCOM2 = freqzfit
 '        @integration
  integratedarea2 = integratedarea
ENDIF

@index_to_mass(freqzPAR)
masszPAR = massz
'        area1 = maxheight * (rightpoint-leftpoint)
area1 = maxheight * FWHMindex      'triangle area (Comisarow height x FWHM)
kevinsfwhm = (rightpoint - leftpoint)

'k1=res
'k2=kevinsres
'k3=xr(ipmax)*(ihighp-ilowp)
'k4=maxheight*(ihighp-ilowp)
'k5=maxheight*(rightpoint-leftpoint)
'k6=(ihighp-ilowp)
'k7=(ihigh2-ilow2)
'k8=(rightpoint-leftpoint)



k1$ = STR$(regmass,14,8)                         'mass of peak
k2$ = STR$(regheight,14,8)                       'height of peak
k3$ = STR$(area2,14,8)                     'trapezoidal area of peak
k4$ = STR$(masszPAR,14,8)                    'interpolated mass of peak
k5$ = STR$(maxheight,14,8)                    'parabola interpolated height
k6$ = STR$(maxheightLOR,14,8)                'Lorentzian interpolated height
k7$ = STR$(maxheightMAGLOR,14,8)            'Magnitude-Lorentzian height
k8$ = STR$(maxheightbest3,14,8)       'Comisarow  interpolated height
k9$ = STR$(kevinsfwhm,14,8)                          'FWHM
k10$ = STR$(kevinsres,14,8)                          'Resolution (m/Dm)
k11$ = STR$(area1,14,8)                               'triangle method area
k12$ = STR$(area3,14,8)                      'extended trapezoidal area
k13$ = STR$(integratedarea1,14,8)               'integrated Comisarow area
k14$ = STR$(maxheightbest4,14,8)        'for testing n=10.5 for Kaiser-Bessel
k15$ = STR$(integratedarea2,14,8)        'for testing n=10.5 for Kaiser-Bessel
' k$="\..............\  ######.####  #####.###  ####.####  #####.####  ####.###
####.###  ####.###  ####.###  #.######  ########.##  #####.####   ####.####
####.####"
```

```
        ' k2$="#####.###   #####.###   #####.###   #####.###   #####.###   #####.#####
#####.####   #####.####"
        ' k3$="      "
        '    IF apodization=4
        '   PRINT
#5,dfile$,k1$,k2$,k3$,k4$,k5$,k6$,k7$,k8$,k9$,k10$,k11$,k12$,k13$,k14$,k15$
        ' ELSE
        '  PRINT #5,dfile$,k1$,k2$,k3$,k4$,k5$,k6$,k7$,k8$,k9$,k10$,k11$,k12$,k13$
        'ENDIF
        IF apodization = 4
          PRINT
#5,dfile$;",";k1$;",";k2$;",";k3$;",";k4$;",";k5$;",";k6$;",";k7$;",";k8$;",";k9$;",";k10$;",";
k11$;",";k12$;",";k13$;",";k14$;",";k15$
        ELSE
          PRINT
#5,dfile$;",";k1$;",";k2$;",";k3$;",";k4$;",";k5$;",";k6$;",";k7$;",";k8$;",";k9$;",";k10$;",";
k11$;",";k12$;",";k13$
        ENDIF
        '                                              Erics specific changes
        '      IF apodization=4
        '     PRINT #5,dfile$;",";k1$;",";k2$;",";k8$;",";k10$
        '    ELSE
        '    PRINT #5,dfile$;",";k1$;",";k2$;",";k8$;",";k10$
        '        PRINT
#5,dfile$;",";k1$;",";k2$;",";k3$;",";k4$;",";k5$;",";k6$;",";k7$;",";k8$;",";k9$;",";k10$;",";
k11$;",";k12$;",";k13$
        '  ENDIF
        'PRINT #5,USING k2$,k1,k2,k3,k4,k5,k6,k7,k8
       ENDIF
     ENDIF
   NEXT i
  ENDIF
  CLOSE #5
  IF llfs2$ = "Y"
   @edit_con
  ENDIF
  'xclearscrn = 5
  '  @plotdata(xclearscrn,1)
  ' @expand_mass_x(mr1,mr2)
  afile$ = ""
  CLS
  ERASE freq(), freqInv(), heights(), abc(),klg()
RETURN
```

APPENDIX B:
BASIC CODE FOR INTERPOLATING PEAK HEIGHTS USING MATIX METHODS USED IN CHAPTER 5

```
PROCEDURE peakfitting2

  rimax = rimax

  heights(1,1) = (klg(rimax - 1)) ^ (1 / n)          'matrix of intensities
  heights(2,1) = (klg(rimax)) ^ (1 / n)
  heights(3,1) = (klg(rimax + 1)) ^ (1 / n)


  'Specify freq array x^2, x, and 1
  'Specify freq. for point to left.

  freq(1,1) = (rimax - 1) ^ 2                      'row 1 of known matrix
  freq(1,2) = (rimax - 1)
  freq(1,3) = 1

  'Specify freq. for center point.

  freq(2,1) = rimax ^ 2                            'row 2 of known matrix
  freq(2,2) = rimax
  freq(2,3) = 1

  'Specify freq. for point to right

  freq(3,1) = (rimax + 1) ^ 2                      'row 3 of known matrix
  freq(3,2) = (rimax + 1)
  freq(3,3) = 1

  MAT INV freqInv() = freq()                         ' find invers of known matrix
  MAT MUL abc() = freqInv()*heights()    'multiply the inverted matrix to intensty matrix

  maxx = (-abc(2,1)) / (2 * abc(1,1))
  '*****************************************************************
  IF (abc(1,1) * maxx ^ 2 + abc(2,1) * maxx + abc(3,1)) >= 0
   maxpoint = (abc(1,1) * maxx ^ 2 + abc(2,1) * maxx + abc(3,1)) ^ n   'interpolated max.
  ENDIF
  freqzfit = freq(2,2) - ((freq(2,2) - freq(1,2)) / 2) * (xr(i + 1) ^ n - xr(i - 1) ^ n) / (xr(i - 1) ^
n - 2 * (xr(i) ^ n) + xr(i + 1) ^ n)

  coffset = freqzfit - rimax
  freqzfit = ipmax + coffset

RETURN
```

APPENDIX C:
BASIC CODE FOR DETERMINING TRAPEZOIDAL AREA OF PEAKS AND EXTENDED TRAPEZOIDAL AREA OF PEAKS USED IN CHAPTER 5

```
PROCEDURE area_trap  'Calculate the peak area using the trap. rule
 ilow = ipmax
 ihigh = ipmax

 DO                                                'find starting point
  ilow = ilow - 1
 UNTIL xr(ilow - 1 ) > xr(ilow)
 ilow = ilow

 DO                                                'find ending point
  ihigh = ihigh + 1
 UNTIL xr(ihigh + 1) > xr(ihigh)
 ihigh = ihigh

 area2 = 0
 FOR i = ilow TO ihigh - 1
  @index_to_mass(i)
  x1 = massz
  @index_to_mass(i + 1)
  x2 = massz
  area2 = area2 + 0.5 * (1) * (xr(i) + xr(i + 1))          'trapezoid area
 NEXT i

 my1 = INT(freqzPAR)
 my2 = freqzPAR
 my3 = INT(freqzPAR) + 1

 trap1 = ((my2 - my1) * .5 * (xr(my1) + maxheight))
 trap2 = ((my3 - my2) * .5 * (xr(my3) + maxheight))
 extratrap = ((my3 - my1) * .5 * (xr(my3) + xr(my1)))

 area3 = area2 + trap1 + trap2 - extratrap                   'extended trap area

RETURN
```

APPENDIX D:
BASIC CODE FOR DETERMINING INTEGRATED AREA OF PEAK USING COMISAROW EXPONENTS USED IN CHAPTER 5

```
PROCEDURE integration
 'Calculate the peak area using the Integral of the Comasarow 9.5

 integratedarea = 0
 lowlimit = max3 - FWHMindex - 1                      'find start
 highlimit = max3 + FWHMindex + 1                     'find end

 DO                                                      'test for positive of ax2+bx+c
   lowlimit = lowlimit + 1
   bigx = abc(1,1) * lowlimit ^ 2 + abc(2,1) * lowlimit + abc(3,1)
 UNTIL bigx > 0
 lowlimit = lowlimit

 DO                                                      'test for positive of ax2+bx+c
   highlimit = highlimit - 1
   bigx = abc(1,1) * highlimit ^ 2 + abc(2,1) * highlimit + abc(3,1)
 UNTIL bigx > 0
 highlimit = highlimit
                                          'just follow the integral in CRC or chapter 5
 a = abc(1,1)
 b = abc(2,1)
 c = abc(3,1)
 dhigh = 2 * a * highlimit + b
 dlow = 2 * a * lowlimit + b

 n = INT(n - .5)
 q = 4 * a * c - b ^ 2
 k = 4 * a / q
 bigx = a * highlimit ^ 2 + b * highlimit + c
 smallx = a * lowlimit ^ 2 + b * lowlimit + c

 firstterm = FACT(2 * n + 2) / (FACT(n + 1) ^ 2 * (4 * k) ^ (n + 1))
 secondtermhigh = k * (dhigh) * bigx ^ .5 / a
 secondtermlow = k * (dlow) * smallx ^ .5 / a
 sigmarhigh = 0
 FOR r = 0 TO n
  sigmarhigh = sigmarhigh + FACT(r) * FACT(r + 1) * (4 * k * bigx) ^ r / FACT(2 * r +
2)
 NEXT r

 sigmarlow = 0
 FOR r = 0 TO n
  sigmarlow = sigmarlow + FACT(r) * FACT(r + 1) * (4 * k * smallx) ^ r / FACT(2 * r +
2)
 NEXT r

 IF a => 0
  IF q < 0 THEN q = ABS(q)
  thirdtermhigh = a ^ -.5 * ARSINH((dhigh) / (q) ^ .5)
  thirdtermlow = a ^ -.5 * ARSINH((dlow) / (q) ^ .5)
 ELSE
  IF q > 0 THEN q = -q
  thirdtermhigh = -ASIN((dhigh) / (-q) ^ .5) / (-a) ^ .5
  thirdtermlow = -ASIN((dlow) / (-q) ^ .5) / (-a) ^ .5
 ENDIF

 highvalue = firstterm * (secondtermhigh * sigmarhigh + thirdtermhigh)
 lowvalue = firstterm * (secondtermlow * sigmarlow + thirdtermlow)

 integratedarea = highvalue - lowvalue
RETURN
```

REFERENCES

1. Von Engel, A. *Electric Plasmas: Their Nature and Uses*, Taylor and Francis: New York, **1983**, Chapter 7.

2. Chapman, B. *Glow Discharge Processes*, Wiley-Interscience: New York, **1980**, 181.

3. McDaniel, E. W. *Collision Phenomena in Ionized Gases*, Wiley: New York, **1980**.

4. Hess, K. R.; Harrison, W. W. *Anal. Chem.* **1988**, *60*, 691.

5. Smith, R. L.; Serxner, D; Hess, K. R. *Anal. Chem.* **1989**, *61*, 1103.

6. Smyth, K. C.; Bentz, B. L.; Bruhn, C. G.; Harrison, W. W. *J. Am. Chem. Soc.* **1979**, *101*, 797.

7. Coburn, J. W.; Kay, E. *Appl. Phys. Lett.* **1971**, *18*, 435.

8. Eckstein, E. W.; Coburn, J. W.; Kay, E. *Spectrochim. Acta* **1982**, *37B*, 947.

9. Stedman, D. H.; Stetser, D. W. *Prog. React. Kinet.* **1971**, *6*, 193.

10. Vieth, W.; Huneke, J. C. *Spectrochim. Acta* **1990**, *45B*, 137.

11. King, F. L.; Harrison, W. W. *Glow Discharge Spectroscopies*, Plenum Press: New York, **1993**, Chapter 5.

12. Smithwick, R. W. *J. Am. Soc. Mass. Spectrom.* **1990**, *3*, 79.

13. Roboz, J. *Introduction to Mass Spectrometry: Instrumentation and Techniques*, Interscience: New York, **1968**.

14. Herzog, R. F. *Trace Analysis by Mass Spectrometry*, Academic Press: New York, **1972**, Chapter 3.

15. Lawrence, E. O.; Livingston, M. S. *Phys. Rev.* **1932**, *40*, 19.

16. Sommer, H.; Thomas, H. A.; Hipple, J. A. *Phys. Rev.* **1949**, *76*, 1877.

17. Wobschall, D.; Graham, J. R.; Malone, D. P. *Phys. Rev.* **1963**, *131*. 1565.

18. Wobschall, D. *Rev. Sci. Instrum.* **1965**, *36*, 466.

19. Anders, L. R.; Beauchamp, J. L.; Dunbar, R. C.; Baldeschwieler, J. D. *J. Chem. Phys.* **1966**, *45*, 1062.

20. McIver, R. T., Jr. *Rev. Sci. Instrum.* **1970**, *41*, 555.

21. McIver, R. T., Jr. *Int. J. Mass Spectrom. Ion Phys.* **1971**, *7*, 471.

22. Beauchamp, J. L.; Anders, L. R.; Baldeschwieler, J. D. *J. Am. Chem. Soc.* **1967**, *89*, 4569.

23. Comisarow, M. B.; Marshall, A. G. *Chem. Phys. Lett.* **1974**, *4*, 282.

24. Comisarow, M. B.; Marshall, A. G. *Chem. Phys. Lett.* **1974**, *26*, 489.

25. Comisarow, M. B.; Marshall, A. G. *Can. J. Chem.* **1974,** *52*, 1997.

26. Allemann, M.; Kellerhals Hp.; Wanczek, K. P. *Chem. Phys. Lett.* **1980**, *75*, 328.

27. Buchanan, M. V.; Hettich, H. R. *Anal. Chem.* **1993,** *65*, 245A.

28. Koster, C.; Kahr, M. S.; Castoro, J. A.; Wilkins, C. L. *Mass Spectrom. Rev.* **1992**, *11*, 495.

29. Laude, D. A.; Johlman, C. L.; Brown, R. S.; Weil, D. A; Wilkins, C. L. *Mass Spectrom. Rev.* **1986**, *5*, 107.

30. Dunbar, R. C. In *FT-ICR/MS: Analytical Applications of Fourier Transform Ion Cyclotron Resonance Mass Spectrometry*; Asaamoto, B. Ed., VCH: New York, **1991**.

31. Marshall, A. G.; Grosshans, P. B. *Anal. Chem.* **1991**, *63*, 215A.

32. Grosshans, P. B.; Marshall, A. G. *Int. J. Mass Spectrom. Ion Proc.* **1992**, *115*, 1.

33. Buchanan, M. V.; Comisarow, M. B. In *Fourier Transform Mass Spectrometry: Evolution, Innovation and Applications, ACS Symp. Series 359*; Buchanan, M. V., Ed., American Chemical Society: Washington, DC, **1987**.

34. Marshall, A. G.; Verdun, F. R. in *Fourier Transforms in NMR, Optical, and Mass Spectrometry*, Elsevier: New York, **1990**.

35. Sharp, T. E.; Eyler, J. R.; Li, E. *Int. J. Mass Spctrom. Ion Phys.* **1972**, *9*, 421-439.

36. Hunter, R. L.; Sherman, M. G.; McIver, R. T. *Int. J. Mass Spectrom. Ion Phys.* **1983**, *50*, 259.

37. Kofel, P.; Allemann, M.; Kellerhals, H. P.; Wanczek, K. P. *Int. J. Mass Spectrom. Ion Proc.* **1986**, *74*, 1.

38. Marshall, A. G.; Wang, T. C. L.; Ricca, T. L. *J. Am. Chem. Soc.* **1985**, *107*, 7893.

39. Kemper, R. P.; Bowers, M. T. in *Techniques for the Study of Ion-Molecule Reactions*, Farrar, J. M.; Saunders, W. H., Eds., John Wiley and Sons: New York, **1988**.

40. Comisarow, M. B. *J. Chem. Phys.* **1978**, *69*, 4097.

41. Cooley, J.W.; Tukey, J.W. *Math Comput.* **1965**, *19*, 297.

42. Wang, M.; Marshall, A. G. *Int. J. Mass Spectom. Ion Proc.* **1988**, *76*, 31.

43. Watson, C.H.; Goodner, K.L.; Eyler, J.R. *Proceedings of the 44th ASMS Conference on Mass Spectrometry and Allied Topics*, **1996**, 502.

44. Marshall, A.G.; Verdun, F.R. *Fourier Transforms in NMR, Optical, and Mass Spectrometry: A User's Handbook*, Elsevier, New York, 1990.

45. Ohorodnik, S.K.; DeGendt, S.; Tong, S.L.; Harrison, W.W. *J. Anal. At. Spectrom.* **1993**, *85*, 859.

46. Raith, A.; Vieth, W.; Huneke, J.C.; Hutton, R.C., *J. Anal. At. Spectrom.* **1992**, *7*, 943.

47. Nasser, E. *Fundamental of Gaseous Ionization and Plasma Electronics*; Wiley-Interscience: New York, 1971.

48. Fang, D.; Marcus, R.K. *Glow Discharge Spectroscopies*; Marcus, R.K., Ed.; Plenum: New York, 1993; Chapter 2.

49. Ohorodnik, S.K.; Harrison, W.W. *Anal. Chem.* **1993**, *65*, 2542.

50. King, F.L.; Harrison, W.W. *Int. J. Mass Spectrom. Ion Proc.* **1989**, *89*, 171.

51. Duckworth, D.C.; Marcus, R.K. *Appl. Spectrosc.* **1990**, *44*, 649.

52. Sanderson, N.E.; Hall, E.; Clark, J.; Charalambous, P.; Hall, D. *Mikrochim. Acta* **1987**, *I*, 275.

53. Element, Finnigan MAT, San Jose, CA 95134-1991. VG9000, FI Elemental, Fisons Instruments, Winsford, Chersire CW7 3BX, England.

54. Watson, C.H.; Wronka, J.; Laukien, F.H.; Barshick, C.M.; Eyler, J.R. *Anal. Chem.* **1993**, *65*, 2801.

55. Barshick, C.M.; Eyler, J.R. *Spectrochim. Acta, Part B* **1993**, *48B*, 1445.

56. Marcus, R.K.; Cable, P.R.; Duckworth, D.C.; Buchanan, M.V.; Pochkowski, J.M.; Weller, R.R. *Appl. Spectosc.* **1992**, *46*, 1327.

57. Ahearn, A.J., Ed. *Trace Analysis by Mass Spectrometry*; Academic Press: New York, 1972.

58. Riciputi, L.R.; Christie, W.H.; Cole, D.R.; Rosseel, T.M. *Anal. Chem.* **1993**, *65*, 1186.

59. Verlinden, J.; Gijbels, R. *Spark Source Mass Spectrometry*; Adams, F.; Gijbels, R.; Van Grieken, R., Eds.; Wiley Interscience: New York, 1988; Chapter 2.

60. King, F.L.; McCormack, A.L.; Harrison, W.W. *J. Anal. At. Spectrom.* **1988**, *3*, 883.

61. King, F.L. Ph.D. Dissertation, University of Virginia, Charlottesville, VA, 1988.

62. Smith, R.L.; Serxner, D.; Hess, K.R. *Anal. Chem.* **1989**, *61*, 1103.

63. Chapman, B.N. *Glow Discharge Processes.* Wiley Interscience: New York, 1980; Chapter 2.

64. Hettich, R. L.; Buchanan, M. V. *J. Am. Soc. Mass Spectrom.*, **1991**, *2(1)*, 22-8.

65. Henry, K.D.; Williams, E.R.; Wang, B.H.; McLafferty, F.W.; Shabanowitz, J.; Hunt, D.F. *Proc. Natl. Acad. Sci. U. S. A.*, **1989**, *86(23)*, 9075-8.

66. Tabet, J.C.; Rapin, J.; Poretti, M.; Gaumann, T. *Chimia*, **1986**, *40(5)*, 169-71.

67. Brenna, J.T.; Creasy, W.R.; McBain, W.; Soria, C. *Rev. Sci. Instrum.*, **1988**, *9(6)*, 873-9.

68. Laukien, F.H.; Allemann, M.; Bischofberger, P.; Grossmann, P.; Kellerhals, Hp.; Kofel, P. *ACS Symp. Ser.*, **1987**, *359*, 81-99.

69. Watson, C.H.; Kruppa, G.H.; Wronka, J.; Laukien, F.H. *Rapid Comm. in Mass Spect.* **1991**, *5*, 249.

70. Castro, M. E.; Russell, D. H. *Anal. Chem.* **1985**, *57(12)*, 2290-3.

71. McIver, R.T. Jr. *Int. J. Mass Spectrom. Ion Processes* **1990**, *98(11)*, 35-50.

72. McIver, R.T. Jr. *Anal. Chem.* **1990**, *62(8)*, 878-80.

73. Limbach, P.A.; Marshall, A.G.; Wang, M. *Int. J. Mass Spectrom. Ion Processes* **1993**, *125(2-3)*, 135-43.

74. Kofel, P.; Alleman, M.; Kellerhals Hp.; Wanczek, K.-P. *Int. J. Mass Spectrom.Ion Processes* **1985**, *65*, 97.

75. Barshick, C.M.; Eyler, J. R. *J. Am. Soc. Mass Spectrom*. **1992**, *3*, 122-127.

76. Barshick, C.M.; Eyler, J. R. *J. Am. Soc. Mass Spectrom*. **1993**, *4*, 387-392.

77. Hofstadler, S.A.; Laude, D.A. Jr. *J. Am. Soc. Mass Spectrom.* **1992**, *3(6)*, 615-23.

78. Hofstadler, S.A.; Schmidt, E.; Quan, Z.; Laude, D.A. Jr. *J. Am. Soc. Mass Spectrom.* **1993**, *4(2)*, 68-76.

79. Guan, Z.; Campbell, V.L.; Drader, J.J.; Hendrickson, C.L.; Laude, D.A. Jr. *Rev. Sci. Instrum.* **1995**, *66(9)* 1201.

80. Marcus, R.K.; Cable, P.R.; Duckworth, D.C.; Buchanan, M.V.; Pochkowski, J.M.; Weller, R.R. *Applied Spectrosc.*, **1992**, *46(9)*, 1327-30.

81. Watson, C.H.; Wronka, J.; Laukien, F.H.; Barshick, C.M.; Eyler, J.R. *Spectrochimica Acta*, Vol *48B(11)*, **1993**, 1445-1448.

82. Watson, C.H.; Wronka, J.; Laukien, F.H.; Barshick, C.M.; Eyler, J.R. *Anal. Chem.* **1993**, *65*, 2801.

83. Watson, C.H.; Wronka, J.; Laukien, F.H.; Barshick, C.M.; Eyler, J.R. *Anal. Chem.*, **1996**, *68*, 573-5.

84. Shohet, J.L.; Phillips, W.L.; Lefkow, A.R.T.; Taylor, J.W.; Bonham, C.; Brenna, J.T. *Plasma Chem. And Plasma Process.* **1989**, *9(2)*, 207-215.

85. Bentz, B.L. Ph.D. Dissertation, University of Virginia, 1979.

86. Bentz, B.L.; Harrison, W.W. *Anal. Chem.* **1982**, *54*, 1644-1646.

87. McCaig, L.; Sesi, N.; Sacks, R. *Applied Spectroc.* **1990**, *44(7)*, 1176-1182.

88. Brewer, S.; Holbrook, T.; Shi, Z.; Trivedi, K.; Sacks, R. *Applied Spectroc.* **1991**, *45(8)*, 1327-1332.

89. Aarstol, M.; Comisarow, M.B. *Int. J. Mass Spectrom. Ion Processes* **1987**, *76(3)*, 287-97.

90. Schweikhard, L.; Guan, S.; Marshall, A.G. *Int. J. Mass Spectrom. Ion Processes* **1992**, *120(1-2)*, 71-83.

91. Bentz, B.L.; Harrison, W.W. *Prog. Analyt. Spectrosc.* **1988**, *11*, 53.

92. King, F.L.; Harrison, W.W. *Mass Spectrom. Rev.* **1990**, *9*, 285-317.

93. Hess, K.R.; Harrison, W.W. *Anal. Chem.* **1988**, *60*, 691-696.

94. Smith, R.L.; Serxner, D.; Hess, K.R. *Anal. Chem.* **1989**, *61*, 1103-1108.

95. Massart, D.L.; Vandeginste, B.G.M.; Deming, S.N.; Michotte, Y.; Kaufman, L. in *Chemometrics: A Textbook,* Elsevier: Amsterdam, 1990; p 42-43.

96. Barshick, C.M. Ph.D. Dissertation, University of Virginia, 1990.

97. Comisarow, M.B.; Grassi, V.; Parisod, G. *Chem. Phys. Lett.* **1978**, *57*, 413.

98. Carlin, T.J.; Freiser, B.S. *Anal. Chem.* **1983**, *55(3)*, 571-4.

99. Cassady, C. J.; Carr, S. R. *J. Mass Spectrom.* **1996**, *31*, 247-254.

100. Wu, Q. Y.; Vanorden, S.; Cheng, X. H.; Bakhtiar, R.; Smith, R. D. *Anal. Chem.* **1995**, *67*, 2498-2509.

101. Oconnor, P. B.; Little, D. P.; McLafferty, F. W. *Anal. Chem.* **1996**, *68*, 542-545.

102. Speir, J. P.; Amster, I. J. *J. Amer. Soc. Mass Spectrom.* **1995**, *6*, 1069-1078.

103. Sannes, K. A.; Brauman, J. I. *J. Phys. Chem.* **1996**, *100*,. 7471-7479.

104. Rodgers, M. T.; Campbell, S.; Marzluff, E. M.; Beauchamp, J. L. *Int. J. Mass Spectrom. Ion Proc.* **1995**, *148*, 1-23.

105. White; C. *Anal. Chem.* **1982**, *54*, 1431.

106. White; C. *Anal. Chem.* **1983**, *55*, 339.

107. Stockigt, D.; Schwarz, J.; Schwarz, H. *J. Phys. Chem.* **1996**, *100*, 8786-8790.

108. Aarstol, M.; Comisarow, M.B. *Int. J. Mass Spectrom. Ion Process.* **1987**, *76*, 287-297.

109. Lee, J.P.; Comisarow, M.B. *Appl. Spectrosc.* **1987**, *41(1)*, 93-98.

110. Lee, J.L.; Chow, K.H.; Comisarow, M.B. *Anal. Chem.* **1988**, *60*, 2212-2218.

111. Brenna, J.T.; Creasy, W.R. *Int. J. Mass Spectrom. Ion Proc.* **1989**, *90*, 151-166.

112. Mitchell, D.W.; DeLong, S.E. *Int. J. Mass Spectom. Ion Process.* **1990**, *96*,1-16.

113. Lee, J. L.; Comisarow, M.B. *Appl. Spectros.* **1989**, *43(4)*, 599-604.

114. Chen, L.; Cottrell, C.E.; Marshall, A.G. *Chemometrics and Intelligent Laboratory Systems* **1986**, *1*,51-58.

115. Verdun, F.R.; Giancaspro, C.; Marshall, A.G. *Appl. Spectrosc.* **1988**, *42(5)*, 715-721.

116. Liang, Z.; Marshall, A.G. *Anal. Chem.* **1990**, *62*, 70-75.

117. Serreqi, A.; Comisarow, M.B. *Appl. Spectrosc.* **1987**, *41(2)*, 288-295.

118. Filler, A.S. *J. Opt. Soc. Amer.* **1964**, *54(6)*, 762-767.

119. Keefe, C.D.; Comisarow, M.B. *Appl. Spectrosc.* **1990**, *44(4)*, 600-613.

120. *CRC Handbook of Chemistry and Physics,* ed. Lide, D.R., 71st edition, CRC: Boca Raton, **1990**, A34-A35.

121. Ingle, J.D.; Crouch, S.R. Spectrochemical Analysis, Prentice Hall: New Jersey, 1988.

122. Cooley, J.W.; Tukey, J.W. *Math Comput.* **1965**, *19*, 297.

123. Dunbar, R. C. In *FT-ICR/MS: Analytical Applications of Fourier Transform Ion Cyclotron Resonance Mass Spectrometry*; Asaamoto, B. Ed., VCH: New York, **1991**.

124. Marshall, A.G.; Verdun, F.R. *Fourier Transforms in NMR, Optical, and Mass Spectrometry: A User's Handbook*, Elsevier, New York, 1990.

125. Liang, Z.; Marshall, A.G. *Anal. Chem.* **1990**, *62*, 70-75.

126. Watson, C.H.; Goodner, K.L.; Eyler, J.R. *Proceedings of the 44th ASMS Conference on Mass Spectrometry and Allied Topics*, **1996**, 1191.

127. Watson, C.H.; Goodner, K.L.; WinICR: An FTICR-MS analysis program downloadable program from HTTP://www.chem.ufl.edu/~eylergrp or via email to watson@ftms1.chem.ufl.edu or goodner@ftms1.chem.ufl.edu

BIOGRAPHICAL SKETCH

Kevin L. Goodner was born January 16, 1970, in Cleveland, TN. The son of Mary and Sammy Goodner, he grew up with his brother Keith and attended Blue Springs Elementary, Trewhitt Junior High, and Bradley Central High Schools.

After graduating from high school, Kevin attended Memphis State University, where he majored in chemistry and mathematics. During the summer between his junior and senior years at MSU, he participated in a summer undergraduate research program at the Georgia Institute of Technology under the supervision of Dr. Richard F. Browner, studying basic aerosol processes. Kevin returned to MSU and graduated in May 1992 with a Bachelor of Science in Chemistry (B.S.Ch.) and a Bachelor of Science (B.S.) with honors in mathematics.

August of 1992 brought Kevin to the University of Florida for his graduate studies in chemistry. He joined Dr. John R. Eyler's research group. Kevin met Jamie in the fall of 1992. He asked her to be his wife in January of 1993, and they were married December 31, 1993 in Kevin's hometown. In the summer of 1994 Kevin conducted research at the Oak Ridge National Laboratory in Oak Ridge, TN, under the supervision of Dr. Christopher M. Barshick.

Kevin is currently living in Winter Haven, FL, where Jamie is conducting her Ph.D. research.

I certify that I have read this study and that in my opinion it conforms to acceptable standards of scholarly presentation and is fully adequate, in scope and quality, as a dissertation for the degree of Doctor of Philosophy.

John R Eyler

John R. Eyler, Chairman
Professor of Chemistry

I certify that I have read this study and that in my opinion it conforms to acceptable standards of scholarly presentation and is fully adequate, in scope and quality, as a dissertation for the degree of Doctor of Philosophy.

James D. Winefordner

James D. Winefordner
Graduate Research Professor of Chemistry

I certify that I have read this study and that in my opinion it conforms to acceptable standards of scholarly presentation and is fully adequate, in scope and quality, as a dissertation for the degree of Doctor of Philosophy.

W. W. Harris

Willard W. Harrison
Professor of Chemistry

I certify that I have read this study and that in my opinion it conforms to acceptable standards of scholarly presentation and is fully adequate, in scope and quality, as a dissertation for the degree of Doctor of Philosophy.

D H Powell

David H. Powell
Associate Scientist of Chemistry

I certify that I have read this study and that in my opinion it conforms to acceptable standards of scholarly presentation and is fully adequate, in scope and quality, as a dissertation for the degree of Doctor of Philosophy.

Paul A. Mueller
Professor of Geology

This dissertation was submitted to the Graduate Faculty of the Department of Chemistry in the College of Liberal Arts and Sciences and to the Graduate School and was accepted as partial fulfillment of the requirements for the degree of Doctor of Philosophy.

December 1996

Dean, Graduate School

LD
1780
1996
.G646

UNIVERSITY OF FLORIDA
3 1262 08554 4277